THZ META-FOILS:
A PLATFORM FOR PRACTICAL APPLICATIONS OF METAMATERIALS

WU JIANFENG

B.Sci. Soochow University (2010)

A THESIS SUBMITTED
FOR THE DEGREE OF DOCTOR OF PHILOSOPHY

DEPARTMENT OF PHYSICS

NATIONAL UNIVERSITY OF SINGAPORE

2014

DECLARATION

I hereby declare that this thesis is my original work and it has been written by me in its entirety. I have duly acknowledged all the sources of information which have been used in the thesis.

This thesis has also not been submitted for any degree in any university previously.

Wu Jianfeng

Wu Jianfeng

January 2014

Acknowledgements

I have been fortunate to be surrounded by many loving people and it is my great pleasure to thank them for their love, support, blessings and encouragement.

First of all, I would like to express my heartfelt appreciation and gratitude to my supervisors, Prof. Mark B. H. Breese, Prof. Herbert O. Moser and Dr. Andrew A. Bettiol, for their invaluable guidance and great support throughout my PhD study. Prof. Mark B. H. Breese provides me his unending support on my research and many overseas conference opportunities, and allows me enough freedom to pursue my own ideas. Prof. Herbert O. Moser gives many useful discussions and his profound theoretical knowledge in the field of metamaterials. Dr. Andrew A. Bettiol guides me to the great chiral work.

During my PhD study, I had the opportunities to work with a number of collaborators. I am thankful to Dr. Jian Linke, Dr. Sascha Pierre Heussler and S. M. Kalaiselvi for fabrication; Dr. Agnieszka Banas and Dr. Krzysztof Banas for FTIR characterization; Prof. Minghui Hong and Binghao Ng for TDS characterization; Prof. Hongsheng Chen and Su Xu for help with theoretical calculations.

I am thankful to all my lab members, Haidong, Zhiya, Songjiao, Sara, Malli, Min, Armin, John, Chengyuan, Prashant, Sudheer, Yaoyong, Liufan, Nannan, Zhaohong. Thank you for all your help in both my study and life.

The research scholarship provided by National University of Singapore for my PhD study is gratefully acknowledged.

Last but the most importantly, I would like to give my great thanks to my girlfriend Jialin and my family. Thank you for all your love which gives me the endless power and passion to go ahead.

Table of Contents

List of Figures

List of Publication

1. J. F. Wu, H. O. Moser, S. Xu, L. K. Jian, A. Banas, K. Banas, H. S. Chen, A. A. Bettiol and M. B. H. Breese, "Functional multi-band THz meta-foils", Sci. Rep. **3**, 3531 (2013).

2. J. F. Wu, H. O. Moser, S. Xu, A. Banas, K. Banas, H. S. Chen and M. B. H. Breese, "From polarization-dependent to polarization-independent terahertz meta-foils", Appl. Phys. Lett. **103**, 191114 (2013).

3. J. F. Wu, B. Ng, S. P. Turaga, M. B. H. Breese, S. A. Maier, M. H. Hong, A. A. Bettiol and H. O. Moser, "Free-standing terahertz chiral meta-foils exhibiting strong optical activity and negative refractive index", Appl. Phys. Lett. **103**, 141106 (2013).

4. J. F. Wu, B. Ng, H. D. Liang, M. B. H. Breese, M. H. Hong, S. A. Maier, H. O. Moser and O. Hess, "Chiral meta-foils for terahertz broadband high-contrast flexible circular polarizers", Phys. Rev. Appl. **2**, 014005 (2014). (Selected as Editors' Suggestion)

5. B. Ng, J. F. Wu, S. M. Hanham, A. I. Fernandez-Dominguez, N. Klein, Y. F. Liew, M. B. H. Breese, M. H. Hong and S. A. Maier, "Spoof plasmon surfaces: A novel platform for THz Sensing", Adv. Opt. Mater. **1**, 543-548 (2013). (Selected as Cover Picture)

6. H. D. Liang, V. S. Kumar, J. F. Wu and M. B. H. Breese, "Ion beam irradiation induced fabrication of vertical coupling waveguides", Appl. Phys. Lett. **102**, 131112 (2013).

7. H. D. Liang, V. S. Kumar, J. F. Wu and M. B. H. Breese, "Ion beam irradiation induced fabricated of vertical coupling photonic structures", Proc. of SPIE **8629**, 86290G-1 (2013).

8. M. D. Ynsa, Z. Y. Dang, M. Manso-Silvan, J. Song, S. Azimi, J. F. Wu, H. D. Liang, V. Torres-Costa, M. B. H. Breese and J. P. Garcia-Ruiz, "Reprogramming hMSCs morphology with silicon/porous silicon asymmetric micro-patterns", Biomed. Microdevices **16**, 229-236 (2014).

9. S. P. Turaga, J. F. Wu, A. Banas, K. Banas and A. A. Bettiol, "Conductively coupled resonator scheme for dispersive transparency in metamaterials", Sci. Rep. (2014). (In review)

10. B. Ng, S. M. Hanham, J. F. Wu, A. I. Fernandez-Dominguez, N. Klein, Y. F. Liew, M. B. H. Breese, M. H. Hong, and S. A. Maier, “Broadband terahertz sensing on spoof Plasmon surfaces”, ACS Photon. (2014). (In review)

Chapter 1

Introduction

1.1 Background and Motivation

A better understanding, manipulation and application of electromagnetic waves in a more general respect plays a crucial role in advancing science and technology. Metamaterials are artificial media that can interact with and control electromagnetic waves [1-6]. They possess novel electromagnetic properties, such as simultaneously negative permittivity and negative permeability. These enable many functional applications including negative refraction [7-25], superlensing [26-31], and invisibility cloaking [32-41].

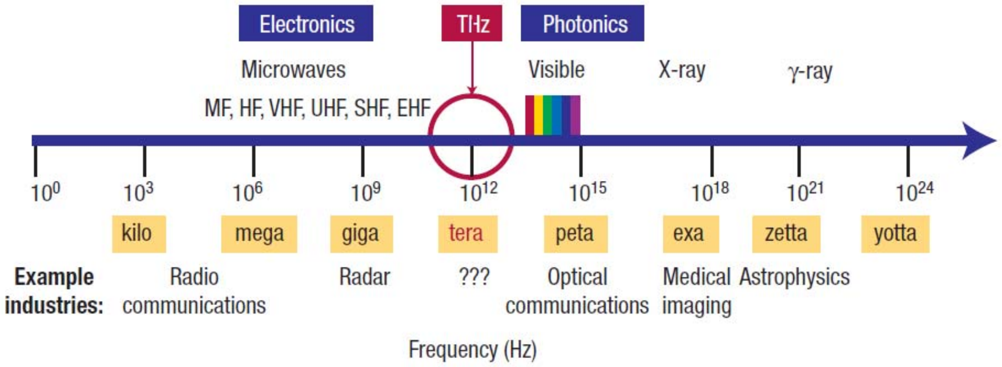

Figure 1.1 *Electromagnetic spectrum. The development of efficient emitters and detectors within each of the spectral regimes has results in the birth of numerous industries. The research for potential applications of THz radiation is steadily intensifying as materials research provides improved sources and detectors [42].*

Terahertz (0.1-10 THz) wave is the electromagnetic wave that occupies the frequency range in between the microwave and infrared regions as shown in Fig. 1.1. Terahertz is a unique frequency range with many important applications such as security detection and gas phase molecule sensing [42-46]. However, it is the least explored frequency regime in the electromagnetic spectrum due to the lack of efficient sources, sensitive detectors and functional devices. Thus, the terahertz band is sometimes referred to the "THz gap". Although THz quantum cascade lasers [47] and THz time domain spectroscopy [48, 49] have been employed to fill the technological gap, the development of THz optics to control and manipulate THz waves is still limited. Metamaterials, unlike natural materials, can be artificially tailored to exhibit strong electric and magnetic responses at THz frequencies. THz metamaterials have now become an attractive and important candidate in THz science and technology [50-52].

Most of the early metamaterials are planar metamaterials [53]. Planar metamaterials cannot be magnetically excited at normal incidence. Recently, three-dimensional (3D) metamaterials have come into focus to realize a negative refractive index and meet practical applications [17-25, 54-61]. Manufacturing real 3D metamaterials is still challenging, especially at THz and optical frequencies. Most 3D metamaterials are fabricated using dielectric materials for various support functions, such as spacers between metal layers, matrices for embedding metallic resonator structures, or as a substrate. These dielectric materials result in losses and shift the original resonances, which impedes the practical application of metamaterials. 3D metamaterials with low losses and many functionalities are in active demand.

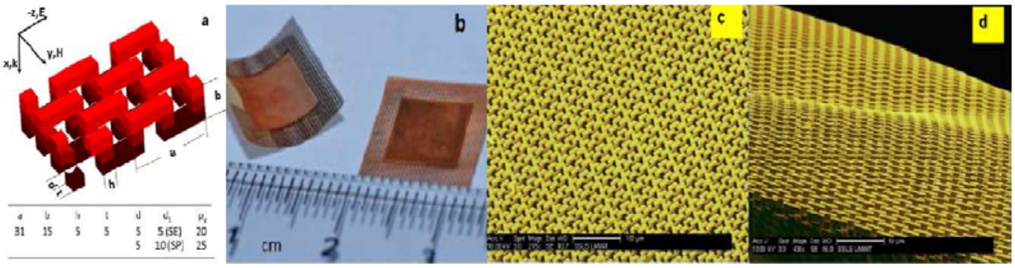

Figure 1.2 *(a) 3D schematic of a 1SE meta-foil showing lithography layers, coordinate frame, definition of geometric parameters, and their measured values (unit μm). (b) Photo of flat and rolled gold meta-foils. (c) Scanning electron microscope (SEM) image of a 2SP gold meta-foil. (d) SEM image of a warped 1SP gold meta-foil [63].*

Moser *et al.* proposed THz meta-foils [52, 62-67]. THz meta-foils, fabricated by conventional photolithography and electroplating, are an all-metal self-supported free-standing metamaterial operating at THz frequencies in Fig. 1.2. It is a unique approach to create an electromagnetic metamaterial that is free of dielectrics. THz meta-foils' properties are solely determined by the geometric structure and the metal properties. The architecture of the meta-foils is based on the well known S-string [68] with the new element of the interconnecting lines that are arranged transversely to the S-strings to hold them together.

1.2 Thesis Outline

THz meta-foils are a 3D all-metal left-handed metamaterial operating at THz frequencies. In this thesis, extending Moser's pioneering work, we design, manufacture and demonstrate four new THz meta-foils with various interesting functions, making them as a platform for practical and novel applications of metamaterials.

Chapter 2 provides a review of metamaterials to describe the fundamental physics and the recent developments in metamaterial research.

Chapter 3 introduces main experimental techniques used in this thesis, such as CST simulation software, UV lithography, gold electroplating, Fourier transform infrared (FTIR) spectroscopy and terahertz time domain spectroscopy (TDS).

Chapter 4 studies functional multi-band THz meta-foils. Multi-band meta-foils, constructed by multi-cell S-string resonators in a single structure, exhibit simultaneously negative permittivity and negative permeability responses at multiple frequencies.

Chapter 5 presents crossed THz meta-foils. Upon showing that conventional parallel-string meta-foils exhibit a strong polarization dependence, we propose crossed meta-foils to be 3D polarization-independent left-handed metamaterials.

Chapter 6 discusses conjugated rosette chiral meta-foils. As the first product of meta-foils combined with chirality, the conjugated rosette chiral meta-foils exhibit strong optical activity, large circular dichroism and negative refractive index with a high figure-of-merit.

Chapter 7 investigates broadband chiral meta-foils. We design, manufacture and demonstrate broadband chiral meta-foils that exhibit a strong circular dichroic effect over a bandwidth of about one octave (1.7-3.3 THz). They provide a new promising route to build up a broadband circular polarizer.

Chapter 8 provides a summary of the work presented in this thesis and gives an outlook on possible future work.

Chapter 2

Review of Metamaterials

2.1 Introduction

Metamaterials are artificially structured media with unit cells much smaller than the wavelength of light [1-6]. These artificial structures interact with electromagnetic (EM) waves and produce fascinating physical properties unavailable in naturally occurring or chemically synthesized materials.

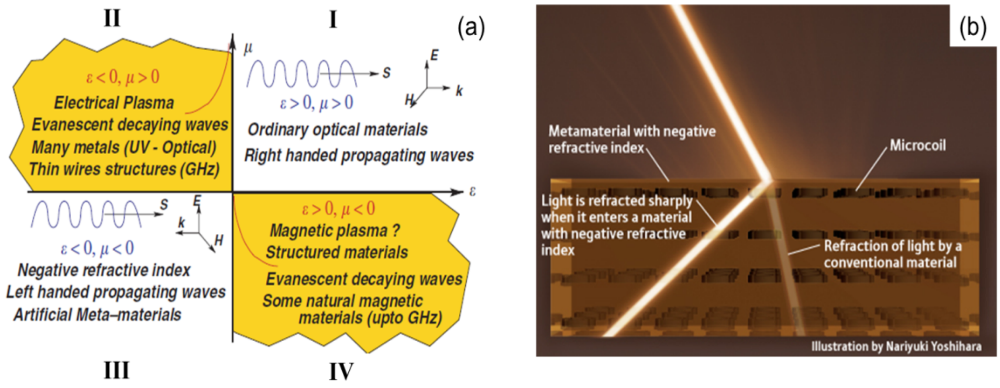

Figure 2.1 *(a) Material parameter space characterized by electric permittivity (ε) and magnetic permeability (μ) [1]. (b) Metamaterials with negative refractive index. Microcoils in a metamaterial interact with the magnetic component of the light wave to refract the beam at a sharper angle [16].*

In electromagnetism, the electric permittivity ε, and magnetic permeability μ are two fundamental parameters characterizing the EM properties of a medium [69]. Physically, permittivity (permeability) describes how an electric (magnetic) field interacts with a medium, which is determined by the ability of a material to polarize in response to the electric (magnetic) field. Consider a monochromatic plane wave propagating in an isotropic, homogenous medium, the refractive index is given by the Maxwell relation,

$$n = \pm\sqrt{\varepsilon\mu} \tag{2-1}$$

Where ε is the relative dielectric permittivity and μ is the relative magnetic permeability of the medium.

There are four possible sign combinations in the pair (ε, μ), which corresponds four different regions in the "material parameter space" in Fig. 2.1(a). The "material parameter space" is used to represent all materials, as far as EM properties are concerned [1]. Region I covers materials with simultaneously positive permittivity and permeability, which include common dielectric materials. Region II contains metals, ferroelectric materials, and doped semiconductors that can exhibit negative permittivity at certain frequencies (below the plasma frequency). Region IV consists of some ferrite materials with negative permeability, whose magnetic responses quickly fade away above microwave frequencies. The most interesting region in the material parameter space is Region III, in which both permittivity and permeability are simultaneously negative. In 1968, such materials had been theoretically predicted by Veselago [7], however, no such materials exist in nature. Due to the unusual properties, materials with simultaneously negative permittivity and permeability are called left-handed materials (LHMs), or negative-index materials (NIMs). Shown in Fig. 2.1(b), if light is incident from positive-index material to a negative-index one, the refracted light lies on the same side as the incident light with respect to the surface normal. Besides negative refraction, the Doppler effect and Cherenkov effect are also reversed in NIMs.

Veselago's theoretical work on NIMs stagnated for a long time, as naturally occurring materials do not provide such properties. Until a significant breakthrough was announced in 1999, Pendry *et al.* [8, 9] first proposed the use of artificial materials to fully expand the available range of material properties as shown in Fig. 2.1(a), and open a completely new research area – metamaterials.

2.2 Electric and Magnetic Responses of Metamaterials

Pendry *et al.* [8] proposed dilute metals with extremely low plasma frequency. A three-dimensional lattice of very thin metallic wires is schematically shown in Fig. 2.2(a). The effective relative permittivity of the system obeys the Drude-Lorentz model as

$$\varepsilon_{r,eff}(\omega) = 1 - \frac{\omega_{p,eff}^2}{\omega(\omega + i\gamma_{eff})} \tag{2-2}$$

where $\omega_{p,eff}$ is the effective plasma frequency $\omega_{p,eff} = \sqrt{\frac{2\pi c^2}{d^2 \ln(d/r)}}$, and γ_{eff} is the damping factor $\gamma_{eff} = \frac{\varepsilon_0 d^2 \omega_p^2}{\pi r^2 \sigma}$. Considering the wire radius $r = 1.0 \times 10^{-6} m$, lattice constant $d = 3.5 \times 10^{-3} m$, the effective plasma frequency $\omega_{p,eff} = 7.52 \times 10^{10} \, rad/s$ is five orders of magnitude smaller than that of noble metals. The effective permittivity of this structure is plotted in Fig. 2.2(b), in which clearly shows negative $\varepsilon_{r,eff}$.

Split ring resonators (SRRs) are one of the typical designs for strong artificial magnetism [9]. Each SRR is composed of two concentric split rings with the openings at the opposite directions as shown in Fig. 2.2(c). Physically, an SRR can be considered as an LC circuit with the metal rings as inductors and the gap as capacitors, in which the resonance frequency is given by $\omega_0 = (LC)^{-1/2}$. Around the resonance frequency ω_0, the external magnetic field in an SRR induces a strong circulating current, resulting in an effective magnetic moment. When the magnetic response is sufficiently strong, the effective relative magnetic permeability $\mu_{r,eff}$ can achieve a negative value. The effective relative magnetic permeability of an SRR array is given by [8]

$$\mu_{r,eff}(\omega) = 1 - \frac{F\omega^2}{\omega^2 - \omega_0^2 + i\Gamma\omega} \tag{2-3}$$

where F is the filling ratio of the SRR $F = \frac{\pi r^2}{d^2}$, ω_0 the resonance frequency $\omega_0 = \sqrt{\frac{3sc^2}{\pi^2 r^3}}$, and Γ is the damp factor $\Gamma = \frac{2}{r\sigma\mu_0}$.

Considering the geometric parameters of the SRR: $d = 4\times 10^{-3}m$, $r = 1\times 10^{-3}m$, and $s = 1\times 10^{-4}m$, the resonance is $f_0 = \omega_0/2\pi = 8.324GHz$. The effective permeability of the SRR around the resonance is calculated and plotted in Fig. 2.2(d), in which clearly shows negative $\mu_{r,eff}$.

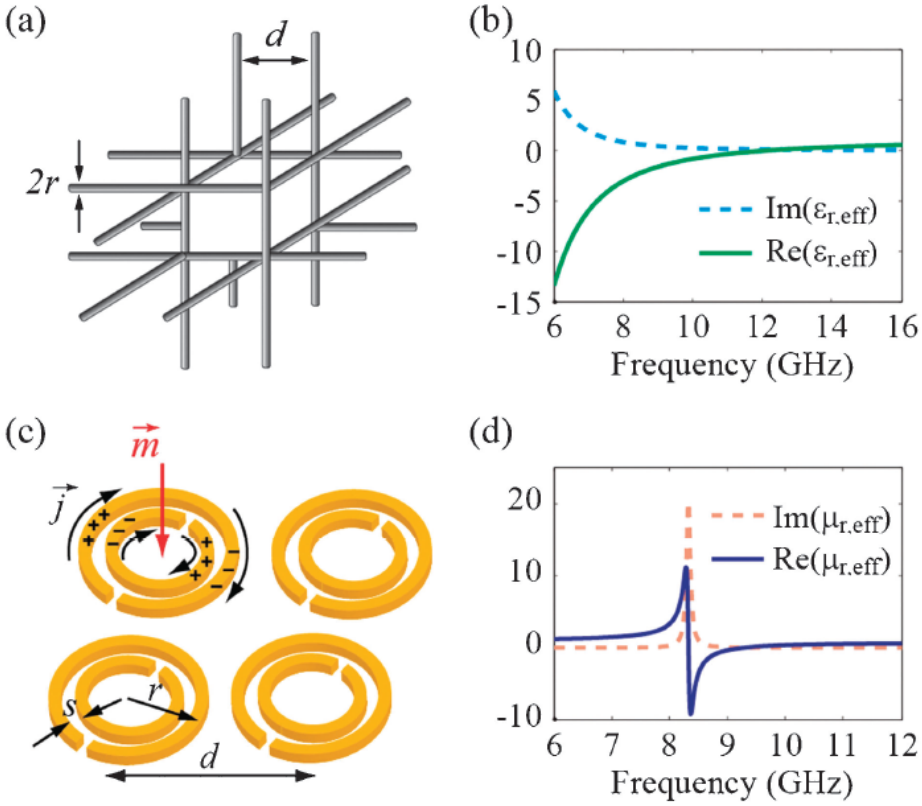

Figure 2.2 *Basic metamaterial structures to implement artificial electric and magnetic responses. (a) Schematic of periodic wires (with radius r) arranged in a simple cubic lattice (with lattice constant d). (b) Effective permittivity of wire media, acting as dilute metals with an extremely low plasma frequency. (c) Schematic of split ring resonators, with outer radius r and separation s between the two rings. A magnetic field penetrating the resonator induces a current* $\vec{j}$*, and thus a magnetic field moment* $\vec{m}$*. (d) Effective permeability of split ring resonators around the resonance frequency.*

Considering a slab of metamaterial, we first characterize it as an effective homogeneous slab to retrieve its effective permittivity and permeability [70]. The first step of the retrieval procedure is to calculate the reflection (S_{11}) and transmission (S_{21}) data by numerical algorithms, such as Finite-Difference Time-Domain (FDTD) and Finite Element Method (FEM). Some commercial softwares, including CST Microwave Studio, COMSOL Multi-physics and ANSOFT HFSS, are widely used in the metamaterials research community. For a plane wave incident normally on a homogeneous slab with thickness d, S_{11} is equal to the reflection coefficient, and S_{21} is related to the transmission coefficient T by $S_{21} = Te^{ik_0 d}$, where k_0 denotes the wave number of the incident wave in free space. The S parameters are related to refractive index n and impedance Z by [71]:

$$S_{11} = \frac{R_{01}\left(1 - e^{i2nk_0 d}\right)}{1 - R_{01}^2 e^{i2nk_0 d}} \tag{2-4}$$

$$S_{21} = \frac{\left(1 - R_{01}^2\right) e^{ink_0 d}}{1 - R_{01}^2 e^{i2nk_0 d}} \tag{2-5}$$

where $R_{01} = \frac{Z-1}{Z+1}$.

The refractive index n and the impedance Z are obtained by inverting Eqs. (2-4) and (2-5), yielding

$$Z = \pm\sqrt{\frac{\left(1 + S_{11}\right)^2 - S_{21}^2}{\left(1 - S_{11}\right)^2 - S_{21}^2}} \tag{2-6}$$

$$e^{ink_0 d} = X \pm i\sqrt{1 - X^2} \tag{2-7}$$

where $X = \frac{1}{2S_{21}\left(1 - S_{11}^2 + S_{21}^2\right)}$.

The value of refractive index n can be determined from Eq. (2-7) as

$$n = \frac{1}{k_0 d}\left\{\left[\left[\ln\left(e^{ink_0 d}\right)\right]'' + 2m\pi\right] - i\left[\ln\left(e^{ink_0 d}\right)\right]'\right\} \tag{2-8}$$

where ' and " denote the real part and imaginary part operator, respectively, and m is an integer. Since the metamaterial slab under consideration is a passive medium, the signs in Eqs. (2-6) and (2-8) are determined by the requirements $\mathrm{Re}(Z) \geq 0$ and $\mathrm{Im}(n) \geq 0$. As shown in Eq. (2-8), the imaginary part of n is uniquely determined, but the real part is complicated by the branches of the logarithm function.

A homogeneous metamaterial slab has been discussed above. However, since a metamaterial itself is not homogeneous, the two apparently straightforward issues mentioned above need to be carefully addressed. Firstly, the location of the two boundaries of the effective slab should be clarified, which we do here by ensuring a constant impedance for various slab thickness. Secondly, the S parameters obtained from simulations or measurements become noisy which can cause the retrieval method to fail, especially at those frequencies where z and n are sensitive to small variations of S_{11} and S_{21}. These two problems were further examined in detail in [70].

2.3 Negative Index Metamaterials

Electromagnetic metamaterials as theoretically introduced by Veselago [7] and experimentally demonstrated by Pendry, Smith, and others [8-11] are artificially structured media that can interact with and control electromagnetic waves. They possess novel electromagnetic properties, such as simultaneously negative permittivity and permeability. These enable many functional applications, such as negative refraction [7-25] and superlensing [26-31].

Metal wires and split rings can produce negative $\varepsilon_{r,eff}$ and $\mu_{r,eff}$, respectively, as illustrated in Fig. 2.2. By overlapping these two sets of meta-structures in the same frequency window, we expect to build metamaterials with a negative effective refractive index (i.e., $n_{eff} < 0$). The idea was first experimentally demonstrated by Smith *et al.* [10, 11] in the microwave region (Figs. 2.3(a) and (b)). Ever since then, metamaterials have drawn considerable attentions and as a result intense efforts have been directed towards designing structures that operate at increasingly higher frequencies (from microwave frequencies to the visible region). However, at optical frequencies, the challenging fabrication process and high losses of metals degrade the magnetic response of split rings, so different structures are required. The most successful optical negative index metamaterials so far are the fishnet structure [17-25], which consists of several layers of metal meshes separated by the dielectric spacer layer (Figs. 2.3(c) and (d)).

Negative index metamaterials bring the world lots of new and exciting applications. Superlens [26-31], as an example of these attractive applications, is discussed here. Pendry proposed that a slab with a refractive index of -1 would act as a perfect lens, not limited by diffraction and therefore able to focus to an arbitrarily small spot [26]. For a conventional lens, the evanescent waves decay exponentially in any medium with a positive refractive index so that they cannot be collected at the image plane, which results in a diffraction-limited image. For a negative index metamaterial lens, both propagating and evanescent waves in phase and amplitude can be completely recovered, resulting in a perfect image (Figs. 2.3(e) and (f)). Zhang *et al.* [29, 31] had experimentally demonstrated the near-field optical superlens (Fig. 2.3(g)). Using silver as a natural optical superlens, they demonstrated sub-diffraction-limited imaging with 60-nanometer half-pitch resolution, or one-sixth of the illumination wavelength.

Objectively speaking, so far all realizations of negative index metamaterials suffer from substantial losses that are too high for most practical applications, therefore, there is still a need to explore new routes to negative refraction.

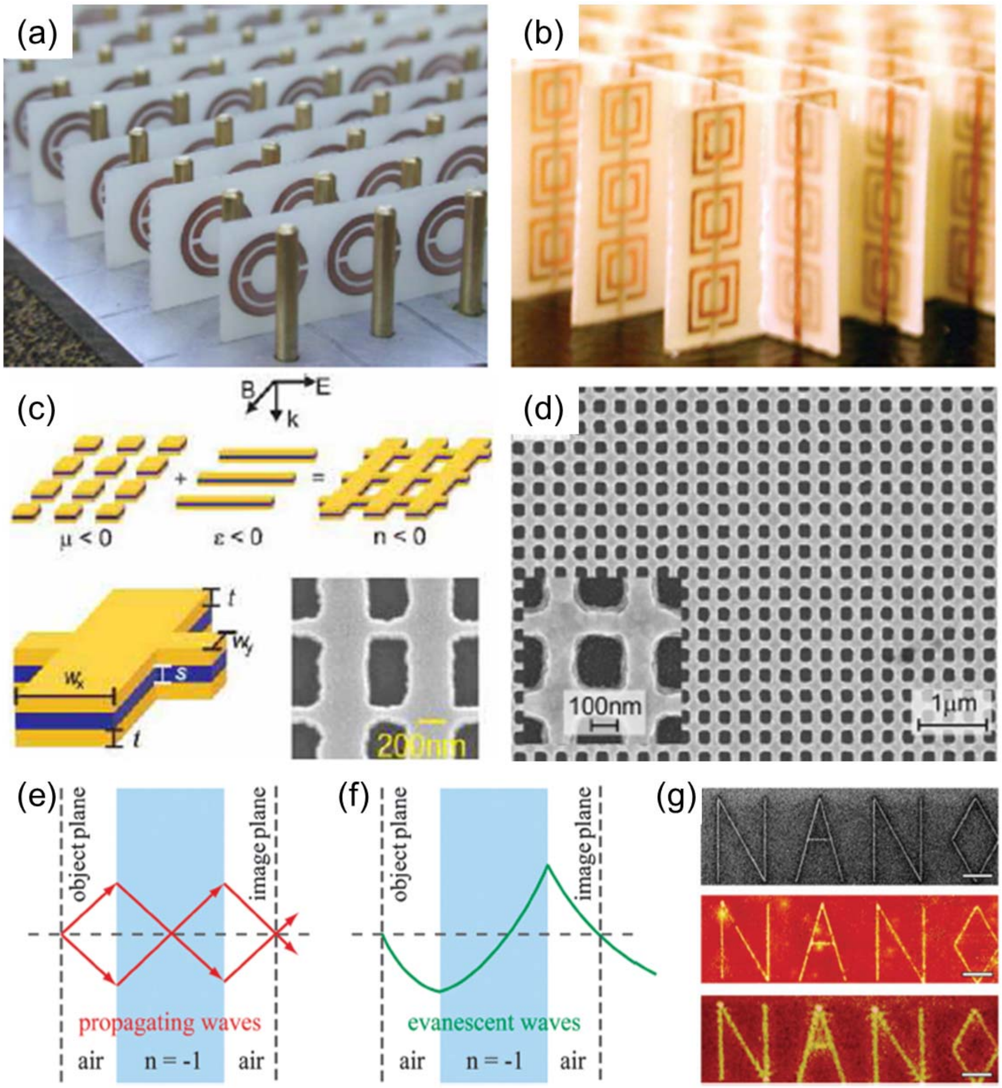

Figure 2.3 *Negative index metamaterials. (a) First metamaterial with simultaneously negative permittivity and permeability [10]. (b) First demonstration of negative refraction in the microwave domain [11]. (c) First demonstration of negative refraction in layered fishnet structures at optical frequencies [18]. (d) SEM image of a fishnet structure with a negative refractive index at 780nm [19]. (e) A flat negative index metamaterial lens brings all the diverging rays from an object into a focused image. (f) The negative index metamaterials slab can also amplify evanescent waves, leading to perfect imaging at the image plane. (g) Experimental demonstration of a near-field optical silver superlens [29, 31].*

2.4 Chiral Metamaterials

Chiral metamaterials are proposed as an alternative route to realize negative refraction by Tretyakov *et al.* [72] and Pendry [73]. Pendry predicted that negative refraction for circularly polarized waves should be possible in optically active media, i.e. structures that rotate the polarization state of light. For circularly polarized waves, the refractive index n depends not only on the electric permittivity ε and magnetic permeability μ, but also on the chirality parameter κ.

$$n = \sqrt{\varepsilon\mu} \pm \kappa \tag{2-9}$$

If the polarization rotary power and thus κ is sufficiently strong, an optically active medium will have a negative refractive index for one circular polarization and a positive index for the other (Fig. 2.4(a)). In this way, neither ε nor μ needs to be negative to obtain negative refraction in chiral metamaterials, as long as κ is large enough.

Chiral metamaterials [74-78] possess a rich variety of electromagnetic properties, such as optical activity, circular dichroism, and negative refraction making them idea candidates for elements in optical setups. Various kinds of chiral metamaterials have been theoretically and experimentally investigated from microwave to terahertz, and optical frequencies (Figs. 2.4(b)-(d)). It is worth highlighting the work of Plum *et al.*, Zhang *et al.* and Gansel *et al.* in the field of chiral metamaterials. Plum *et al.* proposed the bilayered chiral metamaterials in Fig. 2.4(b) [75]. Chirality is achieved by layering arrays of metal rosettes where the rosettes in one layer are rotated by 15 degrees from those in the next layer. Notably, they observed polarization rotation angles as large as about 45 degrees for only two such layers of the metal rosettes, and experimentally demonstrated a chirality-induced negative index of refraction at gigahertz frequencies. Zhang *et al.* introduced another distinct but related structure fabricated by standard microlithography techniques in Fig. 2.4(c) [76]. The chiral unit cell is essentially composed of a set of four split-ring resonators normal to the substrate plane and not parallel to each other, which exhibits negative refractive index at terahertz frequencies. Gansel *et al.* reported the gold helix structures working at near-infrared frequencies, which can be potentially used as a broadband circular polarizer [57] (Fig. 2.4(e)). For propagation of light along the helix axis, the circular polarization with the same handedness as the helices is blocked, whereas the other is transmitted, for a frequency range exceeding one octave.

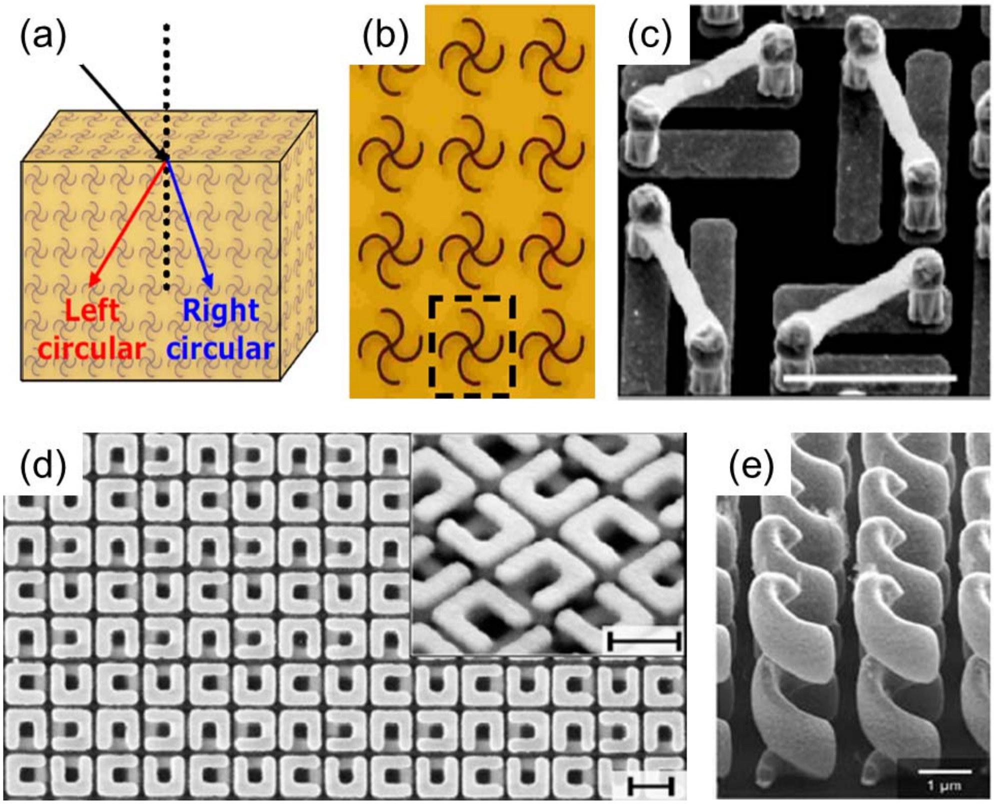

Figure 2.4 *Chiral metamaterials. (a) Metamaterials with sufficiently strong optical activity have a negative refractive index for one circular polarization and a positive index for the other. (b) Experimentally fabricated rosette chiral metamaterials that give negative refractive index at gigahertz frequencies [75]. (c) First experimental demonstration of negative refractive index of chiral metamaterials at terahertz frequencies [76]. (d) Twisted split-ring-resonator photonic metamaterials with huge optical activity [77]. (e) Left-handed helix structures as broadband chiral metamaterials [57].*

2.5 Active and Tunable Metamaterials

Active/tunable metamaterials refer to metamaterials with active/tunable responses to the incident electromagnetic waves [79-89]. In general, the lattice structures of tunable metamaterials are adjustable in real time, making them possible to reconfigure metamaterial devices during operation. Tunability of these metamaterials can be achieved through switching and modulating their electromagnetic properties to be dependent on external optical, electric, magnetic, mechanical or thermal factors, or control signals.

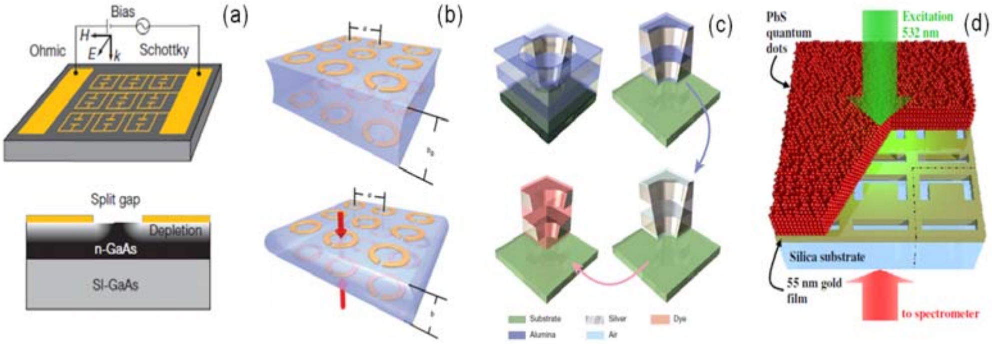

Figure 2.5 *Active and tunable metamaterials. (a) Electrically controlled active THz metamaterials [81]. (b) Magnetoelastic metamaterials [88]. (c) Loss-free and active optical negative-index metamaterials [90]. (d) Photonic metamaterials hybridized with semiconductor quantum dots towards the lasing spaser [92].*

Loss compensation in metamaterials is a crucial step toward their practical applications. In developing active gain-assisted metamaterials, one approach is to combine metamaterials with electrically and optically pumped gain media such as organic dyes [90, 91] and semiconductor quantum dots/wells [92] embedded into the metal structures. Another grand approach is to develop a gain-assisted Plasmon laser, or “lasing spaser” device [93], which is a flat laser with its emission fueled by plasmonic excitations in an array of coherently emitting metamolecules. Furthermore, considerable effort, both experimental and theoretical, has gone into the analysis of active fishnet structures [90, 94, 95]. This field remains an open frontier of metamaterials research.

2.6 Transformation Optics Metamaterials

Transformation optics allows light bending in space in nearly arbitrary manners, similar to general relativity where time and space are curved [96].

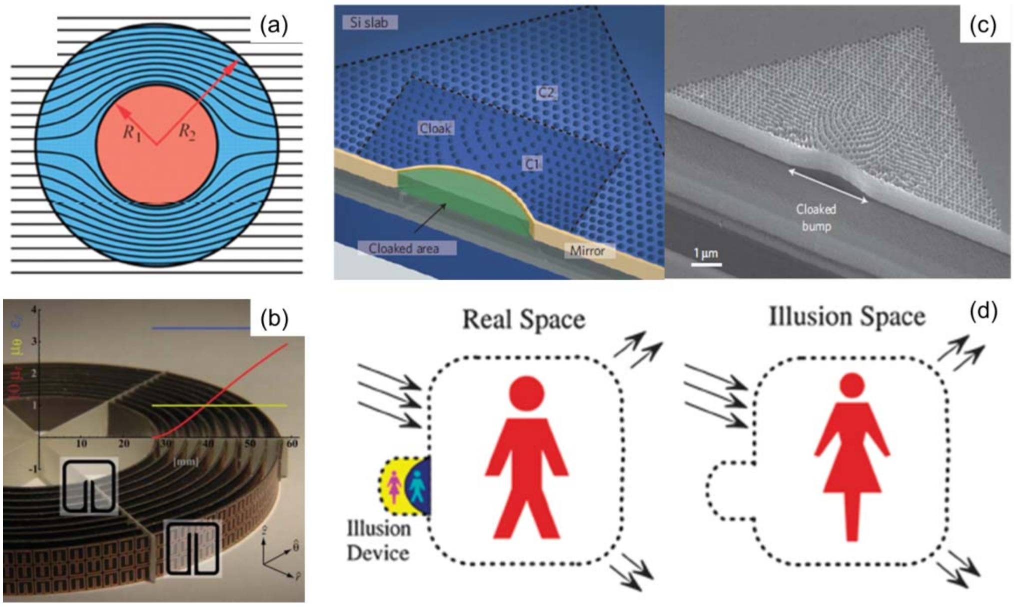

Figure 2.6 *Transformation optics. (a) A cloak in a two-dimensional view [32]. (b) First proof-of-principle cloak built by ten cylindrical layers of SRRs working at microwave frequencies [33]. (c) An optical carpet cloak by drilling holes in a Si slab [40]. (d) The working principle of an illusion device that transforms the stereoscopic image of the object (a man) into that of the illusion (a woman) [97].*

Invisibility cloaking has been the first intriguing concept exploiting transformation optics [32-41]. An analytical coordinate transformation is opening a circular void of radius R_1 in an originally Cartesian frame (Fig. 2.6(a)). The initially straight light ray is deformed to curve around the central hole, and the wavefield is unchanged outside of R_2. Any object in the hole does no interact with the incident radiation, thus, neither object nor cloak can be seen from outside [32]. The first proof-of-principle cloak [33] is built using ten cylindrical layers of split-ring resonators (SRRs) working at microwave frequencies (Fig. 2.6(b)). The experimental results demonstrated that the cloak could significantly decrease scattering from the hidden object and reduce its shadow. Another class of cloaking devices is called carpet cloak, which does not need negative parameters. The object to be hidden lies on a reflecting plane and the cloaking materials covers it like a carpet [37-41]. By restoring the unperturbed reflection from the plane, the object is made to disappear. A 2D carpet cloak within a silicon-on-insulator (SOI) slab waveguide [40] was experimentally studied, which enables broadband and low-loss invisibility at a wavelength range of 1400-1800 nm (Fig. 2.6(c)).

Simulated by the earlier cloaking developments, researchers have extended and generalized clocking to illusion optics [97, 98]. In illusion optics, sources external to the body emit wavefields that lead to the illusionary effect. For example, as shown in Fig. 2.6(d), an object can be hidden without wrapping a clock around it, or it can even be replaced with another, thus opening up new ways of deception [97].

2.7 Conclusions and Outlook

Over the past decade, electromagnetic metamaterials have come a long way from microwave to visible frequencies, thanks to the new electromagnetic theory and modeling software, state-of-the-art fabrication tools as well as greatly improved characterization and analysis techniques. Metamaterials enable us to design our own “atom” and thus create materials with unusual properties and new functionalities, such as negative refraction, superlensing, and invisibility cloaking. Besides these topics discussed above, metamaterials still have lots of interesting applications, such as perfect absorbers [99-101], sensor [102], and electromagnetically induced transparency (EIT) for slow light [103-106] and so on.

Electromagnetic metamaterials are still rather young, and many challenges are still ahead. Making metamaterials large-scale bulk three-dimensional materials at optical frequencies and exploring the suitable designs and materials to effectively reduce the loss in metamaterials are on the way. Recently, nonlinear metamaterials and quantum metamaterials have started to draw researchers’ attentions [4]. However, without further developments in fabrication techniques, no progress in metamaterial research will be possible. New techniques should aim to achieve perfection of nanostructures at close to the molecular level and at low cost, which will be able to build metamaterials to almost any blueprint.

Chapter 3

Experimental Techniques

In this Chapter, the main experimental techniques used in this thesis, such as CST simulation software, UV lithography, gold electroplating, Fourier transform infrared (FTIR) spectroscopy and terahertz time domain spectroscopy (TDS), are discussed in detail.

3.1 CST Microwave Studio

CST Microwave Studio (CST MWS) is a powerful and easy-to-use electromagnetic field simulation software, which is used to carry out the simulation studies of meta-foils. The user can easily create the structure by a powerful graphical solid modeling front end and define the materials properties. After the model has been constructed, a fully automatic meshing procedure is applied. After defining the boundary conditions, the solvers numerically calculate Maxwell’s equations at a given range of frequencies. The user can retrieve results such as scattering parameters (S-parameters), electric and magnetic field distributions and so on.

The Transient solver and Frequency Domain solver are two general purpose tools in CST MWS used in metamaterial simulations. The Transient solver, as a real time domain simulation, is particularly interesting to study the field propagating through a component or along the traces of a printed circuit boards (PCB). Time domain reflectometry (TDR) comes naturally by using this type of solver, but also signal integrity (SI) applications benefit from the capability to use arbitrarily shaped time signals. Besides the specific capabilities in time domain, the Transient solver also delivers broadband frequency domain results such as S-parameters. These simulations can be performed with an arbitrary fine frequency resolution without extra computational cost, thus avoid missing single resonances inside the spectrum. Field results for many frequencies can be derived from one single simulation run. The Frequency Domain solver is particularly useful when operated with a comparatively low frequency, i.e. the structure size is much smaller than the wavelength. The bandpass filter resonance can be optimized and/or tuned in a complete model by applying the solver. It can quickly deliver electromagnetic near and far fields distributions as well as S-parameters.

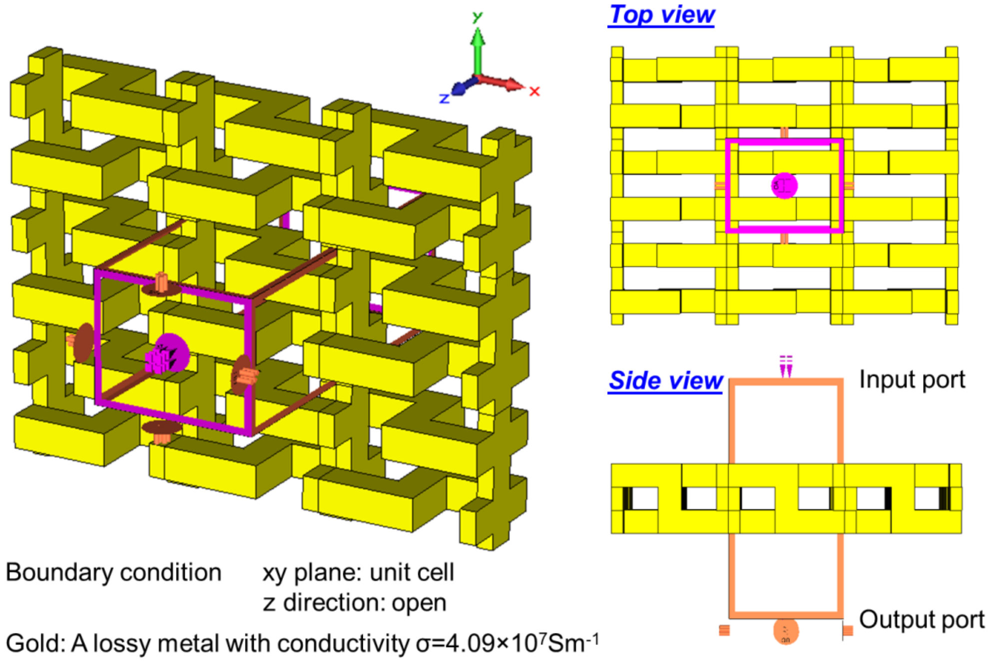

Figure 3.1 *CST model of meta-foils. In simulation, the unit cell boundary condition is applied, and the gold is modeled as a lossy metal with conductivity* $\sigma = 4.09 \times 10^{7}\ Sm^{-1}$.

For meta-foils' simulations, both solvers have been tested and verified to work. The Frequency Domain solver is mainly used in meta-foils' studies. It is usually preferred because it calculates all S-parameters for both polarizations in a single simulation run. In addition, another advantage of the Frequency Domain solver is that it can easily model circular polarization. This is especially efficient for applications that require left-handed and right-handed circular polarized incident light instead of parallel and perpendicular linear polarized light, such as the narrowband and broadband chiral meta-foils described in Chapter 6 and Chapter 7, respectively.

A general procedure of simulation by the Frequency Domain Solver is described below, and a meta-foils' model is illustrated in Fig. 3.1.

(1). Set units and frequency range to be calculated.

(2). Model and define the structure.

(3). Set the boundary conditions.

(4). Define input and output ports.

(5). Generate mesh.

(6). Start the frequency domain solver.

(7). Analyze the results (S-parameters, field patterns, etc.).

3.2 UV Lithography and Gold Electroplating

UV lithography is the most commonly used photolithography technique in operation today, especially for microstructures fabrication. In this thesis, THz meta-foils are experimentally and numerically investigated. The size of THz meta-foil structures is in micron dimension. Thus, UV lithography is selected as the lithography method for meta-foils' fabrication.

As shown in Fig. 3.2(a), a SUSS MA8 Mask Aligner is used. AZ 9260 resist, a positive photoresist, is selected and exposed by 405 nm UV light to pattern the structures. Figures 3.2(b) and (c) show a schematic illustration of the main steps of UV lithography. A general procedure of UV lithography is described as follows.

(1). Optical mask made by laser writer.

(2). Substrate pre-treatment.

- Sample cleaned by Isopropyl Alcohol (IPA), Acetone and De-ionized (DI) water, or cleaned by O_2 plasmas.
- Cr/Au (100nm/50nm) layers sputtered as an adhesion and plating base.

(3). Spin coating

- AZ 9260 resist spun at 6000 rpm (60 s) for 5 µm thickness, at 750 rpm (60 s) for 17 µm thickness.

(4). Softbake Hotplate

- 95 °C (3 mins) to evaporate the excess coating solvent and to compact and harden the photoresist.

(5). UV exposure

- 360 mJ/cm^2 for 5 µm AZ 9260 resist, 900 mJ/cm^2 for 17 µm AZ 9260 resist. Exposed AZ photoresist will be removed finally.

(6). AZ development

- AZ® 400K Developer (1:4): 2 mins for 5 µm resist, 4 mins for 17 µm resist.

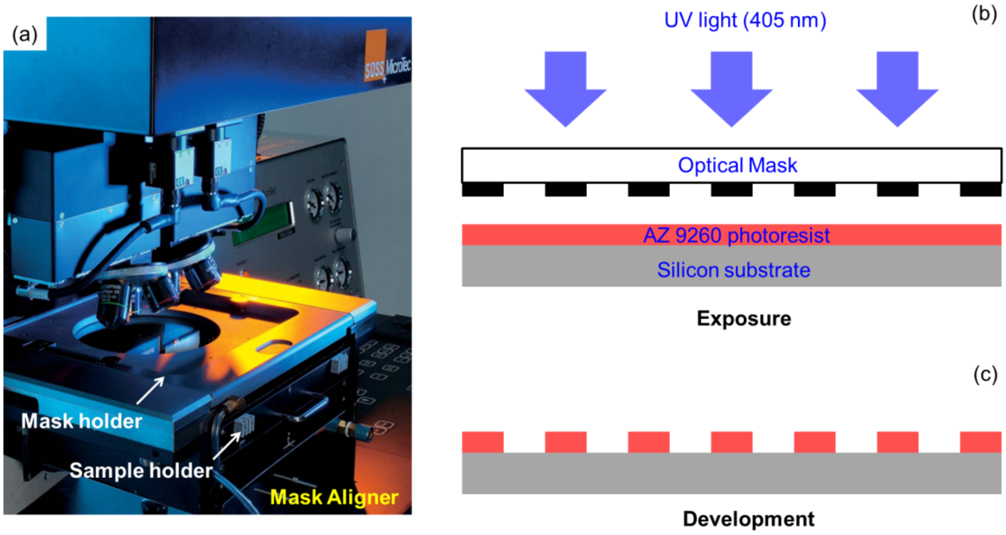

Figure 3.2 *(a) Schematic of SUSS MA8 Mask Aligner. (b) Exposure step: AZ 9260 photoresist coated on silicon substrate is exposed by UV light (405 nm) through the optical mask. (c) Development step: Exposed AZ 9260 resist is removed by AZ developer.*

Gold electroplating is a method of depositing gold onto a conductive surface. This process is also called electrodeposition, which provides an effective way of making metalized structures. The advantage of this technique is in its ability to deposit gold in selective locations with a large range of thicknesses from several nanometers to hundreds of micrometers. In comparison, the gold sputtering technique only deposits gold on the whole surface of the sample with thickness, from several nanometers to hundreds of nanometers. Figure 3.3 shows the gold electroplating setup and a schematic illustration of the main steps. The gold electroplating bath is Neutronex 309 (Enthone Inc.) solution, and the sample is put in the cathode. The process is carried out in a beaker setup at 50 °C solution temperature, pH of 9.5, and under moderate agitation. The current density is set as 0.2 A/dm^2 to achieve good quality structures. Direct current (DC) and pulse current (PC: 20 ms ON, 80 ms OFF) electroplating are two common methods of plating. Comparatively, DC electroplating saves time, and PC electroplating gives much smoother surface. In this thesis, based on an overall consideration, DC electroplating is used in fabricating broadband chiral meta-foils in Chapter 7, and PC electroplating is used in fabricating multi-band, crossed and narrowband chiral meta-foils in Chapters 4-6.

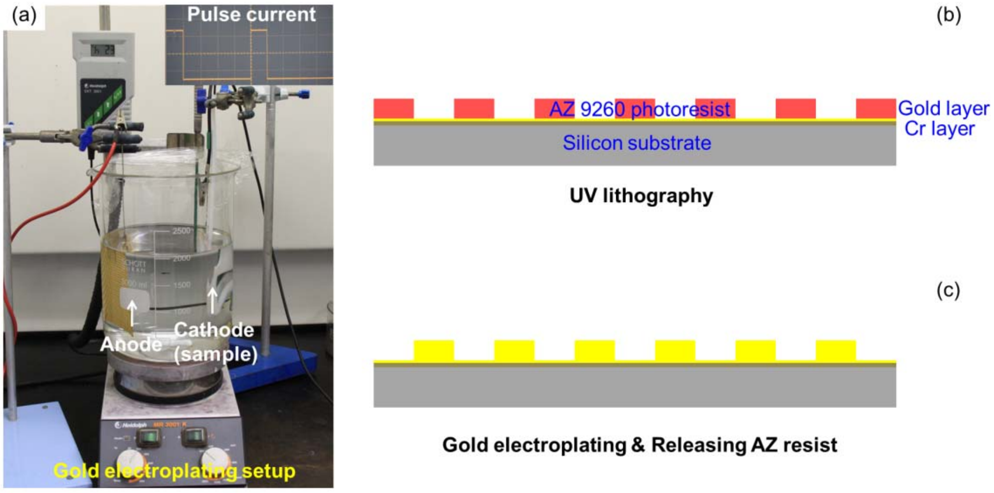

Figure 3.3 *(a) Schematic of gold electroplating setup. (b)-(c) Schematic illustration of gold electroplating. The sample prepared by UV lithography is plated with direct current or pulse current 0.2 A/dm^2 in a beaker setup at 50 °C solution temperature, PH of 9.5.*

3.3 Fourier Transform Infrared Spectroscopy

Fourier transform infrared (FTIR) spectrometry is a powerful technique developed to overcome the limitations encountered with dispersive instruments. To obtain the quick scanning process, a very simple optical device called an interferometer is employed. The interferometer produces a unique type of signal that has all of the infrared frequencies encoded into it. Most interferometers incorporate a beamsplitter which takes the incoming infrared beam and divides it into two optical beams. These two beams are reflected by the fixed and movable mirror, respectively, meet back at the beamsplitter and interfere with each other. The resulting signal is called an interferogram. As the interferogram is measured, all frequencies are being sampled simultaneously. Thus, the use of interferometer results in extremely fast measurements. Finally, the well-known mathematical technique called the Fourier transformation is used to obtain the frequency spectrum (a plot of the intensity at each individual frequency). In FTIR spectroscopy, IR radiation is passed through a sample. Some of the infrared radiation is absorbed by the sample and some of it is transmitted. The resulting spectrum represents the molecular absorption and transmission, creating a molecular fingerprint of the sample. In conclusion, FTIR spectroscopy can identify unknown materials, determine the quality or consistency of a sample and the amount of components in a mixture. Both the basic theory of FTIR and how it works have been briefly discussed above.

In this research work, a Bruker IFS 66v/S, a high performance research grade FTIR spectrometer, is used. As shown in Fig. 3.4, synchrotron radiation light or globar source is selected as the IR source. Synchrotron radiation is from the Infrared Spectro/Microscopy (ISMI) beamline at Singapore Synchrotron Light Source (SSLS) [107]. Different sized circular apertures are used to determine the size of IR beam spot. A THz polarizer is used to control the polarization of light. A beam condenser is added to further focus the IR beam on samples, which can reduce the beam spot size by a factor of 4. A PE/DLa TGS D201 detector is used to collect the spectra. FTIR spectroscopy is used to measure the transmission of meta-foils and investigate their properties in the terahertz range from 2 to 8 THz. The sample chamber pressure is maintained at 2mbar of dry nitrogen gas to avoid signal interferences from water vapor and other gases.

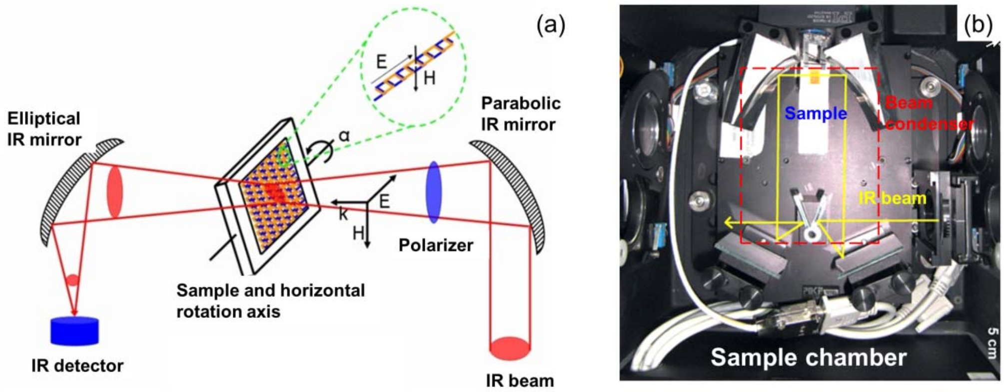

Figure 3.4 *Schematic of FTIR system.*

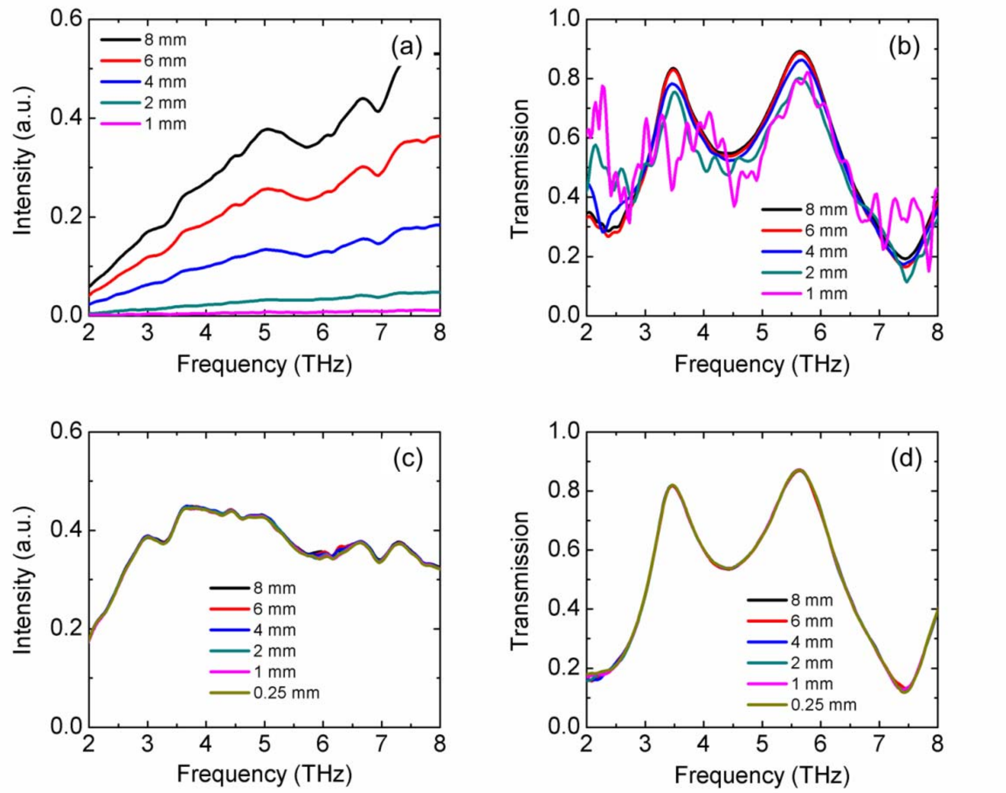

Figure 3.5 *Background spectra of synchrotron radiation and globar source under different sized circular apertures and corresponding transmission spectra of meta-foils by globar source ((a)-(b)) and synchrotron radiation ((c)-(d)), respectively.*

In this section, further comparisons are made between synchrotron radiation and a globar IR source. The advantages of synchrotron radiation over a globar source are experimentally demonstrated on the meta-foils' characterization in the far-infrared (FIR) region. Figure 3.5 shows the background spectra of synchrotron radiation and globar source under different sized circular apertures and the corresponding transmission spectra of meta-foils. Figures 3.5(a) and (b) show the spectra measured using a globar source. The background signal decreases as the aperture size decreases, meanwhile, the amplitude of the peaks in the transmission spectra of the meta-foils becomes lower. When the aperture size is decreased to 1 mm, the flux of incident light reduces to the detection limit of detector and therefore the noisy data appears. In brief, the aperture as large as possible should be selected to obtain accurate results when a globar source is used in the characterization of samples. Figures 3.5(c) and (d) show the measured spectra by synchrotron radiation. All spectra are the same regardless of the aperture size chosen. Two resonance peaks are nicely measured even though the aperture size is decreased to 0.25 mm. In this case, the beam spot size on meta-foils is actually 62.5 μm, and the meta-foils' unit cell size is 30 μm. Based on this excellent spatial resolution, we will be able to study the transverse propagation of the resonant excitation. Furthermore, for the same sized aperture, the signal of synchrotron radiation is much higher than that of globar source, especially for the smaller aperture, which means better signal-to-noise ratio and higher resolution can be obtained by synchrotron radiation. Overall, the aperture chosen has limit impact on final measured results.

To further explain these different results by synchrotron radiation and a globar source, we investigate the nature of synchrotron radiation and blackbody radiation [107-109]. Synchrotron radiation is an electromagnetic radiation emitted by high-energy charged relativistic particles when accelerated by a magnetic field. Blackbody radiation is another electromagnetic radiation given off by a black body at thermal equilibrium, such as a globar source or a Hg arc lamp. The advantage of infrared synchrotron edge radiation as compared to blackbody radiation comes from the phase space distribution of the infrared light emitted from a storage ring rather than from the total power delivered. As the edge radiation is emitted from a small source size into a narrow solid angle, it is much brighter than the isotropic emission of blackbody radiation collected under similar conditions.

In conclusion, synchrotron radiation is experimentally demonstrated here to be a better source for sample characterization in the FIR region, and its high photon flux and brilliance enable high resolution and the characterization of extremely small samples.

3.4 Terahertz Time Domain Spectroscopy

Terahertz time domain spectroscopy (THz-TDS) is another spectroscopic technique in which the properties of a material are probed with short pulses of terahertz radiation [42-45, 48, 49]. THz-TDS can simultaneously provide both the amplitude and phase changes of terahertz light. In this respect, THz-TDS can provide more information than the conventional Fourier-transform spectroscopy discussed in previous section, which is only sensitive to the amplitude.

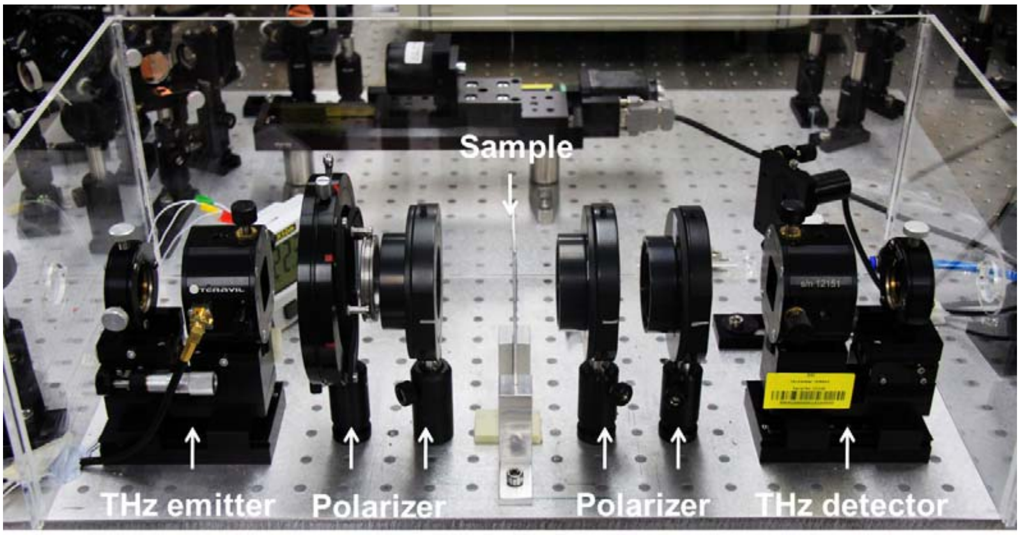

Figure 3.6 *Schematic of terahertz time domain spectroscopy.*

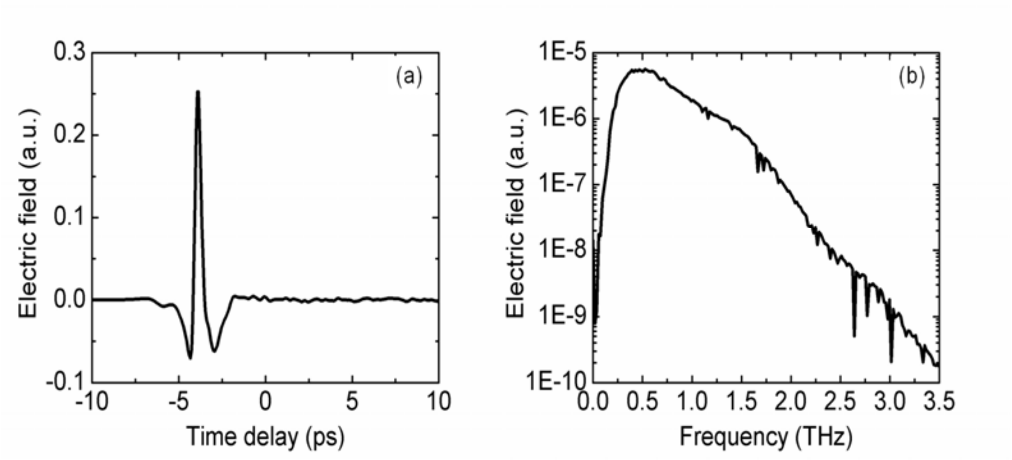

Figure 3.7 *(a) Time domain reference pulse of THz-TDS in a nitrogen purged chamber. (b) Frequency spectrum of the reference pulse.*

As shown in Fig. 3.6, the THz-TDS system consists of a THz emitter and a THz detector, both pumped by a femtosecond laser system. In this THz-TDS system, both emitter and detector are low temperature gallium arsenide (LT-GaAs) based photoconductive switches. THz pulses generated by a Ti:sapphire laser are primarily due to the rapid rise of photo-induced current and the short carrier lifetime of LT-GaAs, which last only a few picoseconds. The electric field of THz pulse interacts in the detector, producing an electrical signal that is proportional to the electric field of THz pulse. By varying the relative time delay between the gated and detected pulses, the time domain spectrum can be obtained. Subsequently, a Fourier transform can be used to extract the frequency spectrum from the time-domain data. Furthermore, four polarizers are employed in Fig. 3.6, two in front of and the other two after the samples, to achieve the co- and cross-polarized transmissions. The transmissions of left-handed and right-handed circularly polarized waves can be further obtained. It is the method used to characterize the chiral meta-foils presented in Chapter 6 and Chapter 7.

Figure 3.7(a) shows the spectrum of terahertz wave generated by THz-TDS. Figure 3.7(b) shows the time domain reference pulse in a nitrogen purged chamber and corresponding frequency spectrum.

Chapter 4

Functional Multi-band THz Meta-foils

4.1 Introduction

Electromagnetic metamaterials were theoretically introduced by Veselago in 1968 [7] and experimentally demonstrated by Pendry, Smith, and others [8-11]. Metamaterials are artificially structured media that can interact with and control electromagnetic waves. They possess novel electromagnetic properties, such as simultaneously negative permittivity and negative permeability. These enable many functional applications including negative refraction [7-25], superlensing [26-31], and invisibility cloaking [32-41].

Most of the early metamaterials featured planar structures consisting of split-ring resonators (SRRs) or a combination of SRRs with wire arrays [12, 53, 103-109]. These planar SRRs can be considered as electrically excited metamaterials at normal incidence since the magnetic field is parallel to the SRR plane and therefore cannot be well coupled into the SRRs. A negative permeability has been first demonstrated in double-SRRs [12] in reflection and in rod-split-ring metamaterials [110] in transmission at THz frequencies, but the coupling efficiency is relatively low.

Three-dimensional (3D) metamaterials [17-25, 54-61] have recently been fabricated for various practical applications even though the processes used to make them have been challenging, especially at THz and optical frequencies. Liu *et al.* [24] presented a general method to manufacture 3D optical metamaterials using a layer-by-layer technique. The SRR layer was fabricated using a standard nanolithography procedure where a photopolymer (PC403) was used as the planarized spacer layer. Similar techniques have been widely applied to fabricate and investigate 3D fishnet metamaterials [25], infrared/optical stereometamaterials [56], chiral metamaterials [77, 78], electromagnetically induced transparency (EIT) metamaterials [105] and so on. Focused ion-beam milling (FIB) and nanotransfer printing techniques [23], capable of cutting nanometer-sized features with a high aspect ratio, were also used to build a 3D fishnet metamaterial on a multi-layer metal dielectric stack. Gansel *et al.* [57] proposed a uniaxial photonic metamaterial composed of 3D gold helices fabricated by direct laser writing and gold electroplating. Burckel *et al.* [58] reported the self-aligned membrane projection lithography (SAMPL) as a path toward fabrication of 3D metamaterials with micrometer-scale characteristic dimensions. Zhang *et al.* [76] built a THz chiral metamaterial by employing standard microlithography techniques. The chiral unit cell is essentially composed of a set of four split-ring resonators normal to the substrate plane and not parallel to each other. Averitt *et al.* [60, 61] fabricated stand-up magnetic metamaterials at terahertz frequencies by UV lithography and multilayer electroplating techniques.

Many metamaterials reported exhibit single-band electric or magnetic responses. As a step towards frequency agile or broadband materials and devices, design and fabrication of multi-resonant metamaterials are potentially useful and thus attractive. Many dual-band planar electric metamaterials were studied in the terahertz regime [117-123]. A dual-band planar metamaterial, constructed by two different sized separated symmetric SRRs, exhibits two distinct electric resonances [117]. Nested SRR structures, designed by the combination of two simple SRRs, were also proposed to be a dual-band electric metamaterial [119]. A multi-layer metamaterial built by stacking planar structures achieve the broadband response, which provides a promising approach to extend SRR based metamaterial operating region from narrowband to broadband with a tunable feature [121]. Besides, a dual fishnet structure, combined by two different sized plate pairs and equivalent sized wires, exhibits a dual-band left-handed metamaterial [122]. Some near-infrared metamaterials with dual-band negative-index characteristics were also reported [124, 125]. Furthermore, some multi-band metamaterial absorbers have been investigated, in which the structural unit cell often consists of multi-sized resonators and a metallic ground plane separated by a dielectric layer [126, 127]. More interestingly, gradient index metamaterials proposed have an effective index of refraction with a constant spatial gradient [128, 129]. The gradient index metamaterial may prove to be an advantageous alternative approach to the development of gradient index lenses and similar optics, especially at higher frequencies. Several efforts have been made [130-132], and the field remains an open frontier of metamaterials research.

Meta-foils proposed by Moser *et al.* [52, 62-67] are another new type of 3D left-handed metamaterial. A self-supported, locally stiff, globally flexible space-grid is formed by the upright S-string architecture with the distinctive feature of metallic transverse interconnects. As spacings of both interconnecting lines and S strings can be varied, we distinguish between pSX meta-foils where p = 1, 2, 3… and X=E or P stand for the number of S periods between subsequent interconnecting lines and for equidistant (E) or pairwise (P) grouded S strings, respectively. Meta-foils are all-metal, self-supported, free-standing electromagnetic metamaterials. Their properties are solely determined by the geometric structure and the metal properties due to no dielectrics such as embedding matrices or supporting substrates. Seemingly similar structures were presented using the term ‘meander’ [133], however, those meander structures are fundamentally different from meta-foils. They lack the spatial phase shift by half S length between adjacent S-strings introduced by Chen *et al.* [68] who did not consider meander structures for their obvious lack of strong resonators. This structural difference was discussed by Moser *et al.* [64] to entail a 3000fold higher resonance peak in the shifted strings. The physical reason is the formation of ‘double-split rings’ between adjacent parts of the shifted S-strings that create strong magnetic moments. Moreover, meander structures still need a dielectric matrix or substrate to hold them. Meta-foils can be considered as being composed of identical inductance-capacitance unit cells that are galvanically coupled to each other in both directions of a plane array. Meta-foils exhibit a magnetic resonance peak in transmission that supports electromagnetic waves propagating through them. Previous meta-foils [63-66] were based on single cells featuring one magnetic resonance peak observed in transmission at frequencies of typically 3-4 THz. Since the magnetic resonance is fixed by the geometrical parameters of the resonator unit cell, meta-foils with multiple cells and resonances become possible, much in analogy to the work done by Chen *et al.* in the GHz range [134].

In this chapter, we extend our research from conventional single-band meta-foils to multi-band meta-foils. We present the first experimental demonstration of double- and triple-band negative refraction index meta-foils in the THz region. Multi-band meta-foils, constructed by multi-cell S-string resonators in a single structure, exhibit simultaneously negative permittivity and negative permeability responses at multiple frequencies. The phenomena are confirmed by CST numerical simulations and Fourier transform infrared spectroscopy measurements. The flexible, freestanding multi-band meta-foils provide a promising candidate for the development of multi-frequency THz materials and devices.

4.2 Simulation, Fabrication and Characterization

In this work, the simulations of meta-foils' properties are performed by using the frequency domain solver of the CST Microwave Studio, which implemented a finite element method to determine reflection and transmission properties. In the simulations, the unit cell boundary condition is applied, and the gold is modeled as a lossy metal [135] with conductivity $\sigma = 4.09 \times 10^7$ Sm^{-1} (see Chapter 3.1).

Figure 4.1 depicts the fabrication process of meta-foils, using three levels of UV lithography with precise alignment and three repeated gold electroplating steps with accurate thickness control. Three optical masks are needed, which carry design patterns and alignment marks. For the initial UV photomask, a soda lime blank (Nanofilm, Wetlake Village, Califormia) with 100 nm thick chromium and 530 nm thick layer of AZ1518 photoresist is patterned by a direct-write laser system (Heidelberg Instruments uPG 101). A 500 µm thick silicon wafer is cleaned and covered with thin layers of Cr/Au (100 nm/50 nm) as an adhesion and plating base, respectively. A 5 µm thick AZ9260 resist is deposited by spin coating and then exposed by UV light in a Mask & Bond Aligner (Karl Suss, MA8/BA6). After resist development, the remaining resist mold is used for gold electroplating to build up a 5 µm thick gold layer. After gold electroplating, another thin layer of Au (50 nm) is sputtered on the sample as a new plating base for the fabrication of second layer structures. The same process sequence is repeated to obtain the second and third layers of the three-dimensional structure to give a total thickness of 15 µm. Precise alignment of photomasks with respect to the already processed structure on the substrate is critical during this process. Next, AZ9260 resist and Au plating base are removed step by step by acetone and gold etchant. Finally, the whole structure is released from substrate by Cr etching (see Chapter 3.2).

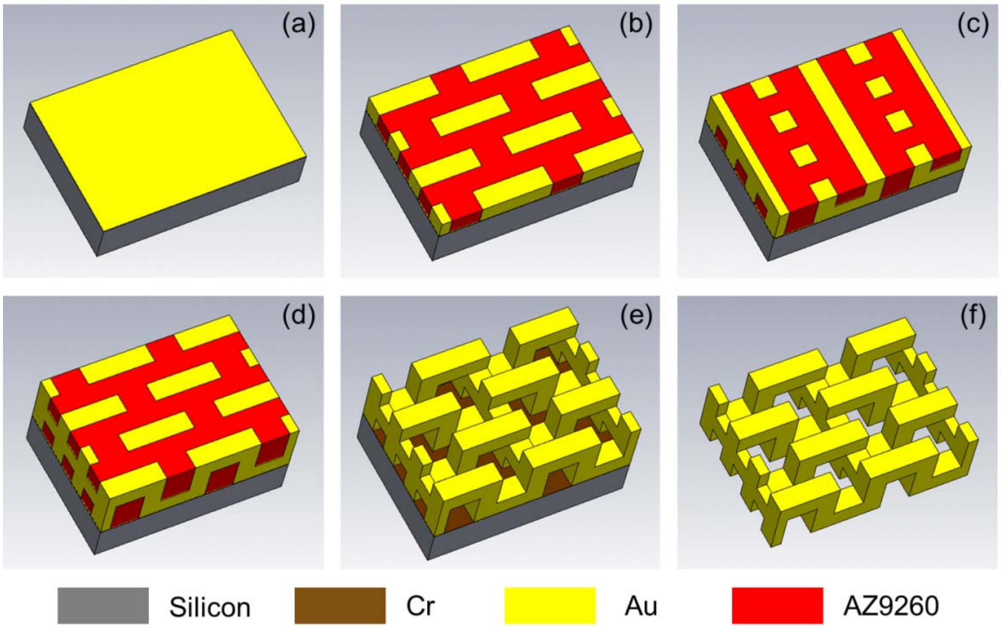

Figure 4.1 *Flowchart of the fabrication of meta-foils. (a) Cr/Au (100 nm/50 nm) layers sputtered on silicon substrate. (b)-(d) Fabrication of three-layer structures by UV lithography and gold electroplating. (e) Removing AZ9260 photoresist and Au plating base step by step by acetone and gold etchant. (f) Releasing the whole structures from substrate by Cr etching.*

A Bruker IFS 66v/S Fourier transform infrared spectrometer (FTIR) is used to characterize the electromagnetic response of the meta-foils in the range of 2 to 8 THz. The radiation source is far infrared synchrotron radiation from the Infrared Spectro/Microscopy (ISMI) beamline at Singapore Synchrotron Light Source (SSLS) [107]. Transmission spectra are acquired by a PE/DLa TGS D201 detector, comparing signals measured with and without sample using a spectral resolution of 0.06 THz (2 cm^{-1}). The sample chamber pressure is maintained at 2 mbar of dry nitrogen gas to avoid signal interferences from water vapor and other gases (see Chapter 3.3).

4.3 Numerical and Experimental Results

As shown in Fig. 4.2, all individual S-strings are connected by transverse rods creating a space-grid to be a meta-foil which is self-supported, locally stiff, and globally flexible. These connections are made between the oscillation nodes of current in the strings to minimize any influence on resonances. Single-cell meta-foils that feature the same unit cell across the whole meta-foil area are shown in Fig. 4.2(a). The unit cell includes two inductance loops that are connected to the same capacitor, which is graphically described by the equivalent circuit. An inductance loop is formed by two bars, one lying in the upstream plane and the other one in the downstream plane, which are connected by the interconnecting line. The capacitor is formed by the two b-legs belonging to adjacent S-strings that are connected to the two bars. This geometry bears some similarity to the fishnet structure [17-23] as the LC-loop stands upright on the substrate plane in case of the fishnet or the y-z-plane in case of the meta-foil, however, there is no correspondence in the fishnet for the direct coupling between the top and bottom plane in the meta-foil nor the capacitors formed by the b-legs. Figure 4.2(b) shows the transmission spectra of single-cell meta-foils. Two dominant peaks appear in the transmission spectrum. The peak at lower frequency is a left-handed magnetic resonance, and the other one at higher frequency is a right-handed electrical resonance, which is confirmed by the parameter retrieval calculations and electric field distribution below. Here, the S-string length is defined by a = 3h + 2w where h is the width of conducting bars and w is the open width of each U portion (there are two ‘U’ motifs in each S). When the S-string length increases, the magnetic peak is red-shifted. The magnetic resonance exhibits a red shift from 4.53 THz to 2.97 THz when the resonator length is increased from 24 μm to 36 μm, which can be explained by the simplified LC oscillator model. Actually meta-foils can be described by a network of coupled LC oscillators. The magnetic resonance frequency is proportional to $1/\sqrt{w}$ because the inductance L scales linearly with the open width w whereas the capacitance formed by the two opposite b-legs of two adjacent S-strings remains unchanged. In comparison, the electrical peak remains the same because a variation of w increases/decreases the respective capacitance and inductance in opposite directions, resulting in no net change. Note that the capacitance acting in case of the electrical resonance is different from the magnetic resonance as it is formed by the two subsequent b-legs in the same S-string. So, if the length of the S-structure is increased, the inductance increases, and the capacitance decreases resulting in little change to the resonance frequency. In summary, the magnetic resonance properties of meta-foils can be tuned by changing the length of the resonator cell.

Starting from these results for single-cell meta-foils, we propose meta-foils featuring two or three single cells with different dimensions in the same structure to realize a bi-cell or tri-cell meta-foils with two or three distinct magnetic resonances. Bi-cell and tri-cell meta-foils in which the open width w alternates between two or three different values are shown in Fig. 4.2.

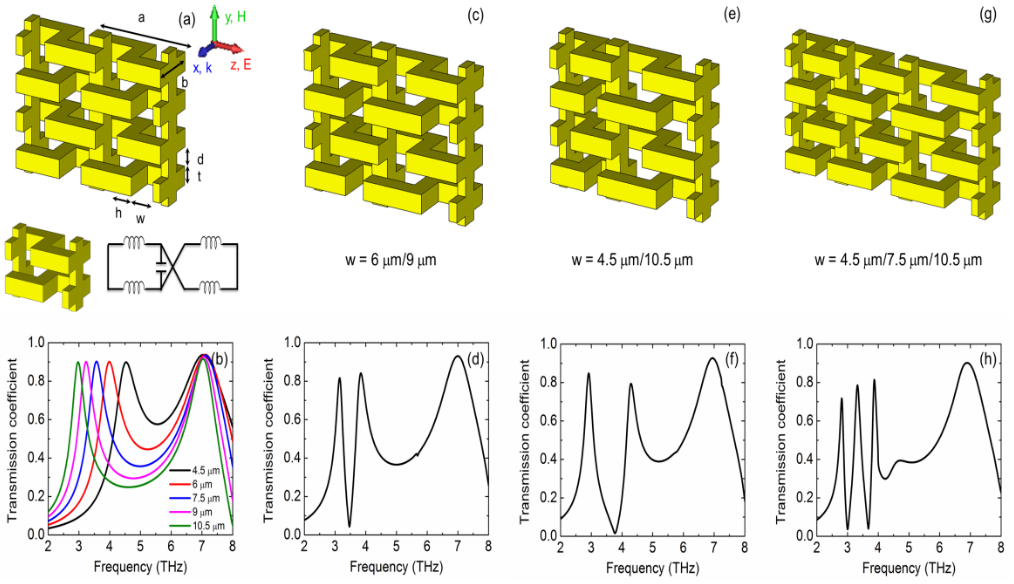

Figure 4.2 *Functional multi-band THz meta-foils designs and simulated results. (a) and (b) 3D schematic and simulated transmission spectra of individual single-cell meta-foils with different S-string length at normal incidence. The resonant unit cell and its equivalent circuit diagram are also depicted. All geometric parameters are given by a = 2w + 3h, b = 15 µm, h = t = d = 5 µm, w is varied from 4.5 to 10.5 µm. The electric field vector E points in z-direction, i.e., along the S-strings, and the magnetic field vector H points in y-direction, i.e., perpendicular to the resonance loops. The magnetic resonance frequency changes from 4.53 over 3.98, 3.57, 3.23 to 2.97 THz as the open width w changes from 4.5 µm to 10.5 µm. (c)-(f) 3D schematics and simulated transmission spectra of bi-cell meta-foils. The open width w is alternated between 6 µm and 9 µm for (c), and 4.5 µm and 10.5 µm for (e). Two magnetic resonance peaks are at 3.15 THz and 3.83 THz for (d), and at 2.92 THz and 4.29 THz for (f). (g) and (h) 3D schematic and simulated transmission spectrum of tri-cell meta-foils (w = 4.5 µm/7.5 µm/10.5µm). Three magnetic resonances are at 2.84 THz, 3.36 THz, and 3.89 THz.*

Two bi-cell meta-foils (w = 6 µm/9 µm and w = 4.5 µm/10.5 µm) are displayed in Figs. 4.2(c) and (e). In the simulated transmission spectra, two different distinct magnetic resonances are excited at 3.15 THz and 3.83 THz for bi-cell meta-foils with w = 6 µm/9 µm, and at 2.92 THz and 4.29 THz where w = 4.5 µm/10.5 µm. These two distinct left-handed magnetic resonances appear due to the superposition of the different resonances formed by each individual cell size of corresponding single-cell meta-foils as well as the mutual coupling between different cells in the bi-cell meta-foils. Their individual peak positions in Figs. 4.2(d) and (f) are close to those of the corresponding single-cell meta-foils in Fig. 4.1(b), except for a slight red shift (stronger for the higher frequency peak). Furthermore, we note that the resonance peaks do not simply superpose, in contrast, a deep dip develops almost down to zero between them. This is due to the opposite phase of two oscillators in between resonance peaks. In the same manner, Figures 4.2(g) and (h) display 3D schematic and corresponding simulated spectra for tri-cell meta-foils (w = 4.5 μm/7.5 μm/10.5 μm). In the tri-cell meta-foils, three magnetic resonances at 2.84 THz, 3.36 THz and 3.89 THz are strongly excited.

As we did previously on 1SE single-cell meta-foils [63, 64], we run a standard parameter retrieval code [70] on these spectral data with the sole purpose to check for a negative refractive index in the magnetic resonance peaks of the bi- and tri-cell meta-foils in comparison with the single-cell meta-foils. The parameter retrieval has been discussed in Chapter 2.2. The retrieval results are shown in Fig. 4.3 where the frequency bands with negative refractive index are highlighted. It is clearly seen that for all double and triple resonances, the refractive index is negative. In particular, the tri-cell meta-foils exhibit three left-handed bands that have not been achieved in a THz single structure before. The retrieval results in Fig. 2 show that, from single- over bi- to tri-cell meta-foils, the number of negative refractive index peaks corresponds to the number of different cells and their respective frequency bands. Negative index peaks are located at the magnetic resonances. Overall, multiple-cell meta-foils are theoretically demonstrated to possess multiple magnetic resonances here. In some frequency ranges, Re(n) reaches the edge of the Brillouin zone which is defined as $\pm\pi/(kb)$. The wavelength inside of the medium becomes smaller than the thickness of the unit cell which renders the notion of refractive index meaningless. A thorough discussion of conditions necessary to extract meaningful effective parameter tensors from anisotropic thin slabs of metamaterials can be found in previous literatures [136-138]. Because of $\lambda/b = 5$ at 4 THz, $b < \lambda/2$ is fulfilled even at the highest frequency considered, where λ is the wavelength in free space which permeates the meta-foil. The limitations discussed by [136-138] should not apply. The retrieval parameters provide a qualitatively explanation of the negative refractive index pass bands at the magnetic resonances.

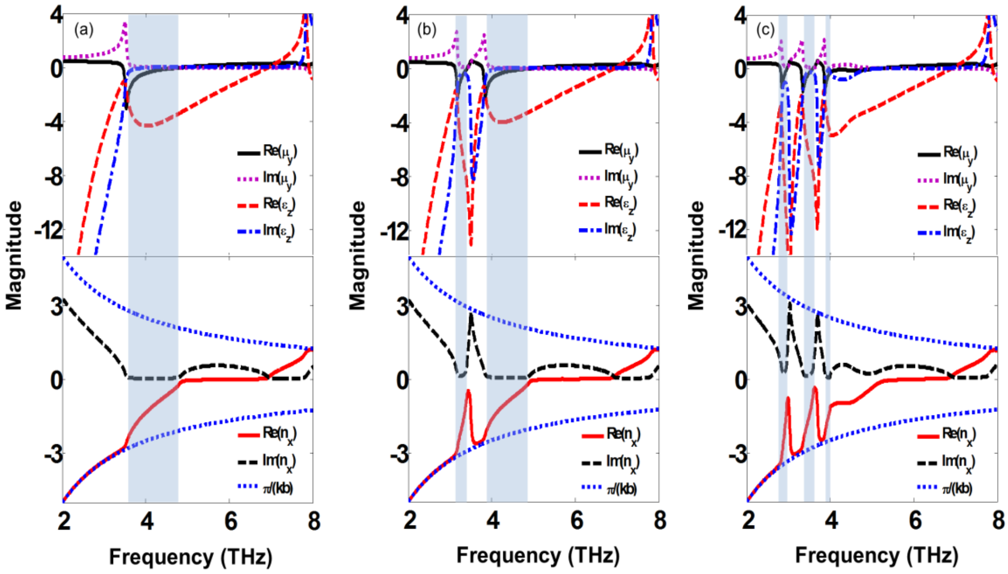

Figure 4.3 *Refractive index of multi-band THz meta-foils from standard parameter retrieval calculations of the relative complex permittivity ε and permeability μ. For the significance of the latter see discussion in main text. Three different types of meta-foils, single-cell meta-foils (w = 7.5 μm) for (a), bi-cell meta-foils (w = 6 μm/9 μm) for (b), and tri-cell meta-foils (w = 4.5 μm/7.5 μm/10.5μm) for (c), were calculated from the simulated transmission at normal incidence. In the shaded frequency ranges, both the permittivity and permeability are negative*

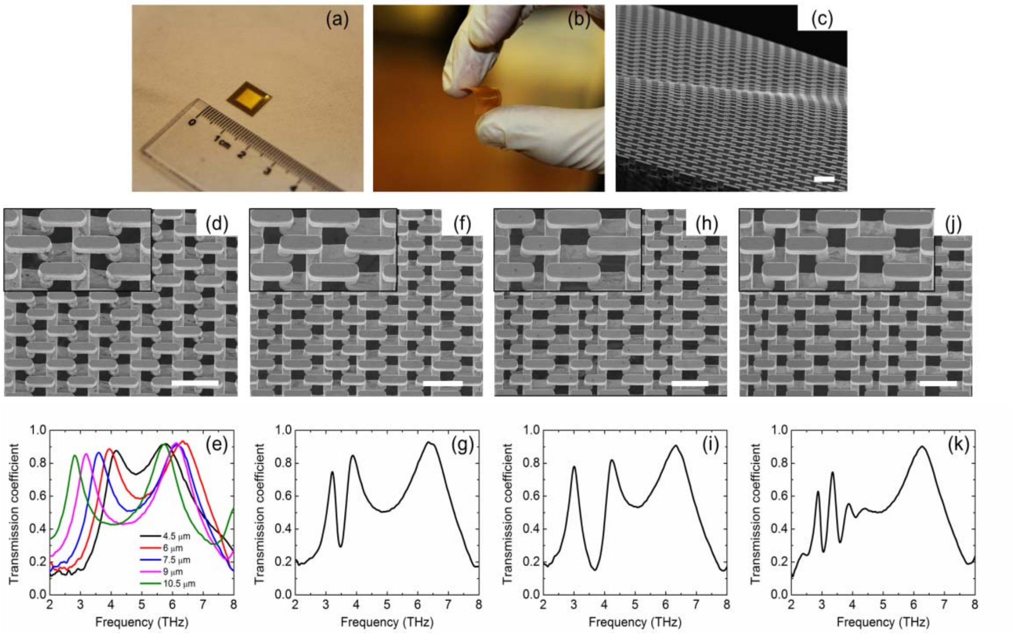

Figure 4.4 *Experimental demonstration of multi-band THz meta-foils. (a) and (b) Photographs of the flat and bent meta-foils. The useful window is 6 mm × 6mm × 0.015 mm (L × W × H). (c) SEM image of flexible meta-foils. (d) and (e) SEM image and measured transmission spectra of single-cell meta-foils. The measured magnetic resonance frequency changes from 4.18, 3.94, 3.60, 3.20 to 2.82 THz as the open width w changes from 4.5 μm to 10.5 μm. (f)-(i) SEM images and measured transmission spectra of bi-cell meta-foils. Two measured magnetic resonance peaks are at 3.11 THz and 3.77 THz for bi-cell meta-foils (w = 6 μm/9 μm), and at 2.90 THz and 4.13 THz for bi-cell meta-foils (w = 4.5 μm/10.5 μm). (j) and (k) SEM image and measured transmission spectra of tri-cell meta-foils (w = 4.5 μm/7.5 μm/10.5μm). Three measured magnetic resonance peaks are at 2.87 THz, 3.35 THz and 3.87 THz. All scale bars in SEM images are 25 μm, and each inset shows a unit cell for each of the structures.*

Figure 4.4 shows images and measured transmission spectra of single-cell, bi-cell and tri-cell meta-foils compared with Fig. 4.1. Figures 4.4(a)-(c) show the flat and deliberately bent meta-foils where the useful window is 6 mm × 6 mm × 0.015 mm (L × W × H). Single-cell meta-foils with different open width w from 4.5 μm to 10.5 μm are fabricated here, and a scanning electron microscopy (SEM) image of single-cell meta-foils (w = 7.5 μm) is selected and shown in Fig. 4.4(d). Figure 4.4(e) shows the measured transmission spectra of these different single-cell meta-foils at normal incidence. The measured magnetic resonance frequency changes from 4.18, 3.94, 3.60, 3.20 to 2.82 THz as the open width w changes from 4.5 μm to 10.5 μm. Compared with the simulated results in Fig. 4.1(b), the magnetic resonances are well reproduced over a substantial range of widths w, whereas the measured electric resonances are all at a lower frequency when compared to the simulated value and have a larger variation. Figures 4.4(f)-(i) depict SEM images of bi-cell meta-foils (w = 6 μm/9 μm and w = 4.5 μm/10.5 μm) along with their corresponding measured transmission spectra. For two different bi-cell meta-foils, two distinct magnetic resonances are obtained, at 3.11 and 3.77 THz where w = 6 μm/9 μm, and at 2.90 and 4.13 THz where w = 4.5 μm/10.5 μm. The positions of magnetic resonance peaks in the measured results are in good agreement with simulated results in Figs. 4.2(d) and (f), demonstrating our ability to accurately fabricate bi-cell meta-foils. Remaining discrepancies between the experimental and simulated results in the positions, heights and widths of the resonance peaks are considered as being mainly due to small imperfections in both the fabrication process and characterization, which were ignored in simulations. Figures 4.4(j) and (k) show an SEM image of tri-cell meta-foil (w = 4.5 μm/7.5 μm/10.5 μm) along with its measured transmission spectrum. Three separate magnetic resonances are excited at 2.87 THz, 3.35 THz and 3.87 THz. The stronger reduction of the measured peak heights compared to the simulated ones as observed in single-cells and bi-cells is because the measured spectral resolution is no longer high enough, especially for the shaper resonance peak. The measured spectral resolution is 0.06 THz whereas the full width at half maximum (FWHM) of the high-frequency peak in the tri-cell is about 0.2 THz. So, only three measured points have to represent the sharp peak, thus touching at the limit set by Shannon’s theorem.

4.4 Equivalent Circuit Analysis

We use equivalent circuit theory to better understand the physical nature of the coupling between resonators and, in detail, dip formation in multi-band meta-foils. Here, we select the bi-cell meta-foils as an example. Figures 4.5(a) and (b) show how the equivalent circuit is related to the actual structure. In the center of Fig. 4.5(a), the vertical bar is part of an interconnecting line and represents resistance R_C . The top and bottom half S extending to the right is a split ring with inductance L_2 and resistance R_2, and likewise to the left with inductance L_1 and resistance R_1. The subsequent overlapping bars give rise to capacitance C. The crossover of conductors in the circuit scheme takes care of the different connection of the split rings to the central bar R_C. According to Kirchhoff’s voltage (mesh) rule, we can write down the sum of the voltages around the loops,

$$\left(i\omega L_1 - \frac{i}{\omega C} + R_1\right) j_1 + R_C\left(j_1 + j_2\right) = A_1 e^{-i\omega t} \tag{4-1}$$

$$\left(i\omega L_2 - \frac{i}{\omega C} + R_2\right) j_2 + R_C\left(j_1 + j_2\right) = A_2 e^{-i\omega t} \tag{4-2}$$

where $L_k, R_k, j_k, A_k, k = 1,2$ are the inductances, resistances, currents, EMF amplitudes of the two resonance circuits, respectively, and R_C, C, ω, t are the coupling resistance, capacitance, angular frequency of the circuits, and time, respectively. For comparison, a single resonator is described by

$$\left(i\omega L_1 - \frac{i}{\omega C} + R_1 + R_C\right) j_1 = A_1 e^{-i\omega t} \tag{4-3}$$

Straightforward algebra yields the solutions

$$j_1 = \frac{A_1\left(R_2+R_C\right)-A_2R_C+iA_1\left(\omega L_2-\frac{1}{\omega C}\right)}{\frac{L_1+L_2}{C}+R_1R_2-\omega^2L_1L_2-\frac{1}{\omega^2C^2}+R_C\left(R_1+R_2\right)+i\left(\omega\left(L_1R_2+L_2R_1+R_C\left(L_1+L_2\right)\right)-\frac{R_1+R_2+2R_C}{\omega C}\right)}e^{-i\omega t}$$

(4-4)

$$j_2 = \frac{A_2\left(R_1+R_C\right)-A_1R_C+iA_2\left(\omega L_1-\frac{1}{\omega C}\right)}{\frac{L_1+L_2}{C}+R_1R_2-\omega^2L_1L_2-\frac{1}{\omega^2C^2}+R_C\left(R_1+R_2\right)+i\left(\omega\left(L_1R_2+L_2R_1+R_C\left(L_1+L_2\right)\right)-\frac{R_1+R_2+2R_C}{\omega C}\right)}e^{-i\omega t}$$

(4-5)

For a quick assessment of the structure of the solutions and according to common practice, we assume all resistance zero to obtain

$$j_{1,R=0} = \frac{iA_1\left(\omega L_2-\frac{1}{\omega C}\right)}{\frac{L_1+L_2}{C}-\omega^2L_1L_2-\frac{1}{\omega^2C^2}}e^{-i\omega t} \tag{4-6}$$

$$j_{2,R=0} = \frac{iA_2\left(\omega L_1-\frac{1}{\omega C}\right)}{\frac{L_1+L_2}{C}-\omega^2L_1L_2-\frac{1}{\omega^2C^2}}e^{-i\omega t} \tag{4-7}$$

We note that denominator is common to both solutions and has two zeros at $\frac{1}{L_1C}$ and $\frac{1}{L_2C}$. The numerators vanish at either $\frac{1}{L_1C}$ and $\frac{1}{L_2C}$, so a zero of the denominator is not automatically a resonance. To analyze the frequency behavior more detail, we write the formulae in terms of the resonance frequencies $\omega_1 = \frac{1}{L_1C}$ and $\omega_2 = \frac{1}{L_2C}$ and obtain normalized currents

$$\frac{j_{1,R=0}}{A_1 C}e^{i(\omega t-\pi/2)}=\frac{\omega\left(\left(\frac{\omega}{\omega_2}\right)^2-1\right)}{\omega^2\left(\frac{1}{\omega_1{}^2}+\frac{1}{\omega_2{}^2}\right)-\left(\frac{\omega^2}{\omega_1\omega_2}\right)^2-1}=f\left(\omega,\omega_1,\omega_2\right) \tag{4-8}$$

$$\frac{j_{2,R=0}}{A_2 C}e^{i(\omega t-\pi/2)}=\frac{\omega\left(\left(\frac{\omega}{\omega_1}\right)^2-1\right)}{\omega^2\left(\frac{1}{\omega_1{}^2}+\frac{1}{\omega_2{}^2}\right)-\left(\frac{\omega^2}{\omega_1\omega_2}\right)^2-1}=g\left(\omega,\omega_1,\omega_2\right) \tag{4-9}$$

Inspecting Eq. (4-8), we see that at the zero of the numerator, ω_2, which is also a zero of the denominator, the value of the function $f\left(\omega,\omega_1,\omega_2\right)=\frac{\omega_2^3}{\omega_1^2}$ is finite while infinite at ω_1, and vice versa for function $g\left(\omega,\omega_1,\omega_2\right)$. Hence, the resonances of the coupled resonators in the zero resistance approximation are located at the same frequencies as the simple resonators.

In Fig. 4.5(c), the above functions are plotted for ω_1 = 4 THz and ω_2 = 3.2 THz in the range of 3 to 4.2 THz, in steps of 0.01 THz. Taking squares of the normalized currents which represent power transmission, we obtain Fig. 4.5(d). Obviously, the individual resonance peaks do not overlap, but create a zero amplitude and power in between them. We further check this by looking at ω_1 = 4.0 THz and ω_2 = 3.9 THz in the range of 3.5 to 4.2 THz. Again, Figures 4.5(e) and (f) show that peaks do not overlap, but develop a deep dip in between. In fact, even in the limit of equal resonance frequencies, it can be shown that there is a zero in between. For the case of non-zero resistances, it is much more complex, so we did not move forward further. Overall, we investigate theoretically the physical nature of the coupling between resonators and dip formation in the bi-cell meta-foils by the zero resistance approximation in the equivalent circuit theory.

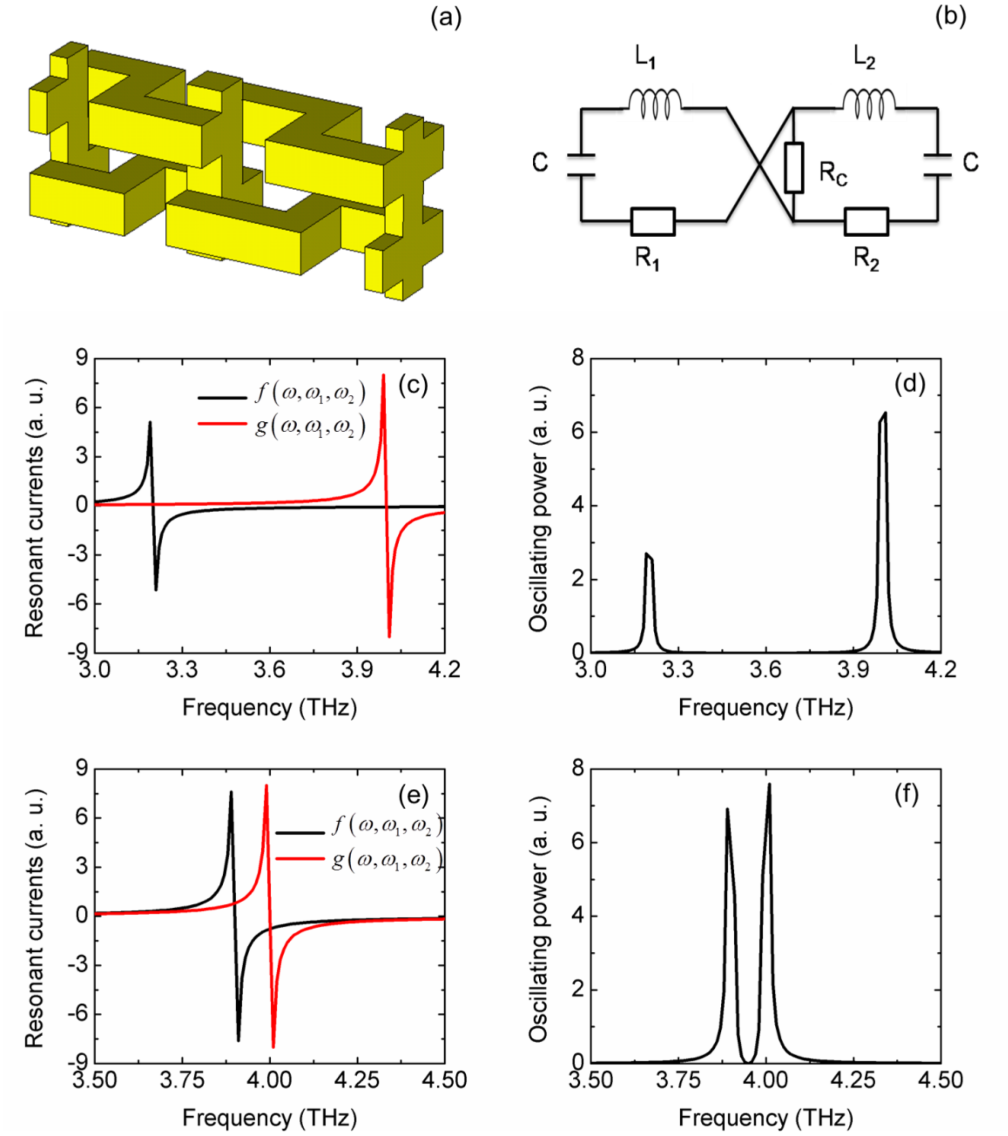

Figure 4.5 *3D schematic of bi-cell meta-foils for (a) and the circuit diagram for (b). (c)-(f) Amplitude of normalized resonant currents* $f(\omega,\omega_1,\omega_2)$ *and* $g(\omega,\omega_1,\omega_2)$*, and the normalized oscillating power versus frequency, respectively. Resonance frequencies* ω_1*,* ω_2 *are 4.0 and 3.2 THz for (c) and (d), and 4.0 and 3.9 THz for (e) and (f), respectively.*

4.5 Discussion

In order to further understand the performance of single-, bi- and tri-cell meta-foils, we investigate the electric field distribution through numerical MWS simulation. Figures 4.6(a) and (b) show the electric field distribution in single-cell meta-foils (w = 7.5 μm) at magnetic and electrical resonances, respectively. It provides a more visual confirmation of the magnetic resonance at 3.57 THz and electrical resonance at 7.12 THz. At 3.57 THz, the adjacent S-strings are greatly excited with opposite field indicating strong charging of the capacitors formed by the b-legs of adjacent S-strings, and, thus, high amplitudes of oscillations in the LC loops creating the magnetic resonance. Note that in this magnetic resonance case the individual S-strings are at approximately the same potential level with adjacent strings at the opposite. In contrast, at 7.12 THz, each U portion in an S-string is electrically excited with some capacitive charging also between b-legs of the same S-string in addition to the potential differences between adjacent strings. Figures 4.6(c) and (d) show the electric field distribution in the bi-cell meta-foils (w = 6 μm/9 μm) at the magnetic resonances. Figure 4.6(e) displays the electric field distribution at the electrical resonance. At 3.15 THz and 3.83 THz, cells with w = 9 μm and w = 6 μm are strongly excited, respectively. At 7.02 THz, electric excitation similar to Fig. 4.6(b) is observed. Thus, in the bi-cell meta-foils the two magnetic resonances are selectively excited in either of the two single-cell sub-meta-foils. Figures 4.6(f)-(i) show the electric field distribution in the tri-cell meta-foils (w = 4.5 μm/7.5 μm/10.5 μm) at resonances. Similar to the bi-cell case, in tri-cell meta-foils three magnetic resonances are selectively excited in either of the three single-cell sub-meta-foils, in monochromatic simulation. If we compare these magnetic modes with those of other metamaterial structures, such as the split-ring resonator [11], Ω-ring resonator [139], subwavelength dielectric resonator [140] and fishnet structures [17-25], etc, we find they share similar magnetic mode in the frequency range of negative permeability. Although the shapes of these structures are quite different, the overall field distributions are all very similar. One can also see that the negative permeability vanishes when this magnetic mode disappears, e.g. 7.12 THz in the single-cell meta-foils, 7.02 THz in the bi-cell meta-foils and 7.05 THz in the tri-cell meta-foils. These results also imply that the proper magnetic modes in subwavelength scale are very important to achieve left-handed behavior.

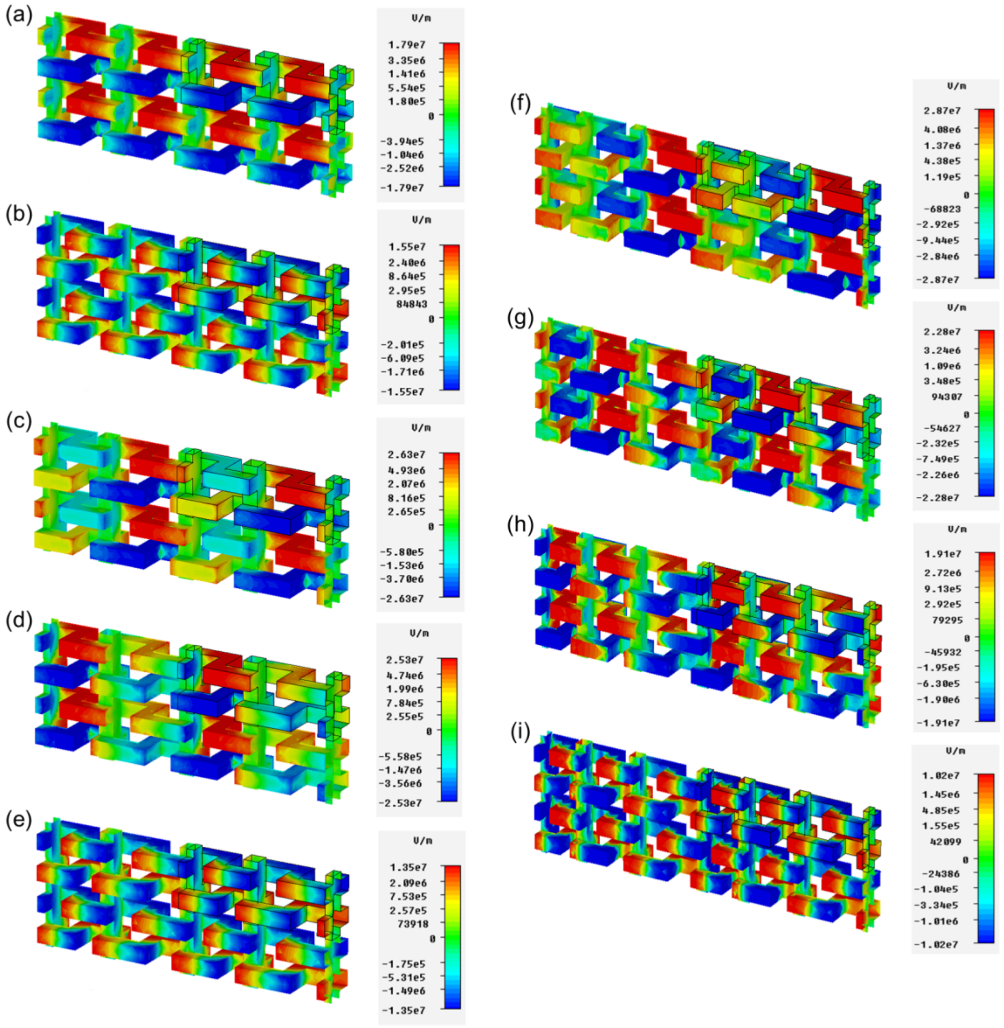

Figure 4.6 *Electric field distributions of multi-band THz meta-foils at different resonances. (a) and (b) MWS simulation results of the electric field distribution on single-cell meta-foils (w = 7.5 μm) at 3.57 THz and 7.12 THz. (c)-(e) MWS simulation results of the electric field distribution on bi-cell meta-foils (w = 6 μm/9 μm) at 3.15 THz, 3.83 THz and 7.02 THz. (f)-(i) MWS simulation results of the electric field distribution on tri-cell meta-foils (w = 4.5 μm/7.5 μm/10.5 μm) at 2.84 THz, 3.36 THz, 3.89 THz and 7.05 THz.*

The proposed multi-band meta-foils are different from previous work on THz dual-band electrical resonances in coupled split ring resonators (SRR) [117-127] in a few crucial aspects. Multiple-cell meta-foils are characterized by galvanic coupling, magnetic excitation and transmission peaks at resonances whereas previous coupled SRR samples exhibit capacitive-inductive coupling, electric excitation and transmission dips at resonances, respectively. The continuous geometry of meta-foils results in stronger galvanic coupling compared to capacitive-inductive coupling in discrete SRR structures. In addition, no matter what multiple cells are designed into an actual meta-foil, the filling of the area is always complete in contrast to the <100% filling by split rings resonators. These fundamental differences make multiple-cell meta-foils a distinct class of metamaterials with unique characteristics.

Such multiple-cell meta-foils open up a wide range of new potential applications. In general, devices may exploit polychromatic properties or the coupling of spectro-geometric features. Among the former, multiple-passband filters, multi-band sensors, polychromators, and polychromatic beams may be envisaged, among the latter phase gratings and diffractive optical elements (DOEs). Applications would include spectral calibration and identification of molecules by multi-band filters, fast parallel sampling spectroscopy by polychromators, and metrology by phase gratings. To identify molecules, for instance, that exhibit absorption peaks in the THz range under discussion, they could be detected by means of a specific multi-band meta-foil that is designed to have transmission peaks at the spectral position of a selected molecule's absorption peaks. So, if broadband THz radiation is shone through a specific meta-foil having transmission resonances at 2.05, 2.9, 4.35 THz, the latter would act as a filter letting pass only the radiation corresponding to these resonances. If this filtered radiation would then pass through a sufficiently dense accumulation of the PETN molecule that features absorption peaks at these frequencies, it would be absorbed and the change in intensity could be measured by a simple broad-band detector. For TNT at 2.2, 3.8, 4.7 THz, it would work similarly. PETN (pentaerythritol tetranitrate) and TNT (2,4,6-trinitrotoluene) are well-known explosives having strong absorption bands at the above frequencies, respectively. So, absence of the selected molecule or presence of other molecules would entail a higher detector response whereas the presence of the selected molecule would diminish detector response. The obvious potential application is in the detection of explosives in security. A broader discussion was given in [141]. Furthermore, interestingly, multi-band meta-foils can also be mass manufactured cost-effectively to serve as optical elements by plastic moulding [64].

4.6 Conclusion

In conclusion, novel single-cell, bi-cell and tri-cell meta-foils have been manufactured and investigated. Results obtained from numerical simulation and spectroscopic characterization show that bi/tri-cell meta-foils feature two/three slightly red-shifted resonance peaks of the corresponding single-cell meta-foils which, however, are separated by a deep dip. The spectral location of each peak can be controlled by the geometric parameters, thus, the peaks are structurally tunable. In this way, multiple-cell meta-foils can be adapted to specified spectral signatures of target molecules. The concept might be extended to multi-cell meta-foils having four or more different cells with potential applications to novel multi-frequency devices, and, when grouping resonators of the same frequency, to fast polychromators or demultiplexers. In addition, multi-band meta-foils can be tailor-made to virtually any shape, they can be bent, and wrapped around objects to shield them from electromagnetic radiation, thus becoming true metamaterials on curved surfaces. Although implemented here at THz frequencies, multiple-cell meta-foils can also be extended to higher infrared and optical frequencies.

Chapter 5

From Polarization-dependent to Polarization-independent THz Meta-foils

5.1 Introduction

Most split-ring resonators (SRRs) or a combination of SRRs with wire arrays are polarization-dependent metamaterials. Benefitting from the polarization-dependent properties, active or switchable applications of metamaterials are achieved [53, 79]. Actually, conventional parallel-string meta-foils [63-66], for example, multi-band THz meta-foils as discussed in Chapter 4, are polarization-dependent. This dependence requires that for maximal magnetic resonances at normal incidence, the electric field should point along the S-strings and the magnetic field should be perpendicular to the resonance loops.

Polarization-independent metamaterials have been also investigated. An electric metamaterial, consisting of two concentric ring resonators with interdigitated fingers placed between the rings, was experimentally demonstrated that its bandstop resonance remained unaffected by changes in both the incident angle and the polarization [142]. In another electric metamaterial, the switch between polarization-dependent state and polarization-independent state used micromachined actuators to reconfigure the lattice structure from 2-fold to 4-fold rotational symmetry [143]. Besides, some polarization-independent metamaterial absorbers have been designed, in which the structural unit cell consists of symmetric metallic resonators and a metallic ground plane separated by a dielectric layer [101, 126, 127]. It is worth highlighting that the broadband polarization-independent resonant light absorption has been realized by ultrathin plasmonic super absorbers [101]. Furthermore, most famous fishnet structures achieve the negative refractive index and, at the same time, are polarization-independent metamaterials [17-25]. Overall, the polarization-independent properties are achieved by designing structures with intrinsic symmetry. Polarization-independent metamaterials are indeed a very useful branch of metamaterials to meet practical applications. However, most of them are still planar structures, and the metal-dielectric-metal multilayer structures are not really three-dimensional (3D) structures.

In this Chapter, we further discuss the polarization dependence of conventional parallel-string THz meta-foils. To become completely independent of polarization, we propose crossed meta-foils and demonstrate numerically and experimentally their polarization-independent properties. Crossed meta-foils consist of individual S-strings connected to each other along orthogonal directions, with a square at the crossing points. In this way, polarization-independent, all-metal, self-supported, free-standing, 3D left-handed metamaterials are achieved that provide a versatile platform for developing practical applications of metamaterials.

5.2 Results and discussion

Crossed meta-foils are manufactured using three-level lithography with precise alignment and three repeated gold electroplating steps with accurate thickness control. Simulations of crossed meta-foils are performed by the frequency domain solver of the CST Microwave Studio. Sample characterization is carried out by a Bruker IFS 66v/S Fourier-transform infrared spectrometer. Details of simulation, fabrication and characterization have been discussed in Chapter 3 and Chapter 4.

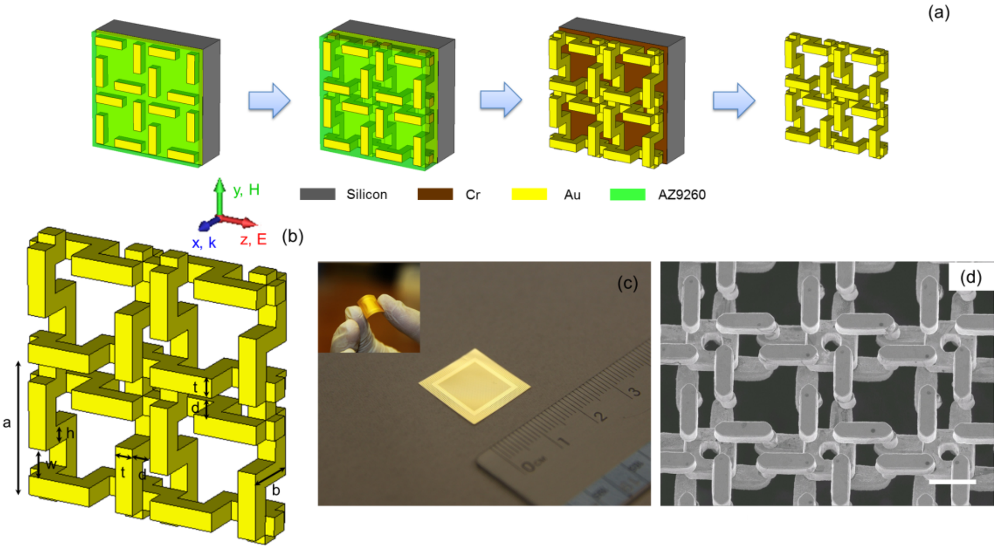

Figure 5.1 *(a) Flowchart of the fabrication process of crossed meta-foils. (b) 3D schematic of a crossed meta-foil. The geometry parameters are given by a = 30 μm, b = 15 μm, h = 5 μm, t = 5 μm, d = 5 μm, and w = 7.5 μm. The crossed meta-foil is axisymmetric in 90° steps with respect to an axis through the center of the coupling ring perpendicular to the y-z plane. (c) Photographs of flat and bent crossed meta-foils. (d) SEM image of a crossed meta-foil (scale bar 15 μm).*

Figure 5.1(a) depicts the flowchart of the fabrication process of crossed meta-foils. Figure 5.1(b) shows a 3D schematic of a crossed mete-foil and its geometry parameters. The crossed meta-foil is axisymmetric in 90° steps with respect to an axis through the center of the coupling ring perpendicular to the y-z plane. Figure 5.1(c) shows flat as well as deliberately bent crossed meta-foils where the useful window is 12 mm × 12 mm × 0.015 mm (L × W × H). It indicates that the crossed meta-foils can be tailor-made to virtually any shape, being practical and flexible metamaterials. A scanning electron microscopy (SEM) image of a crossed meta-foil is shown in Fig. 5.1(d), which reveals the good quality of fabrication.

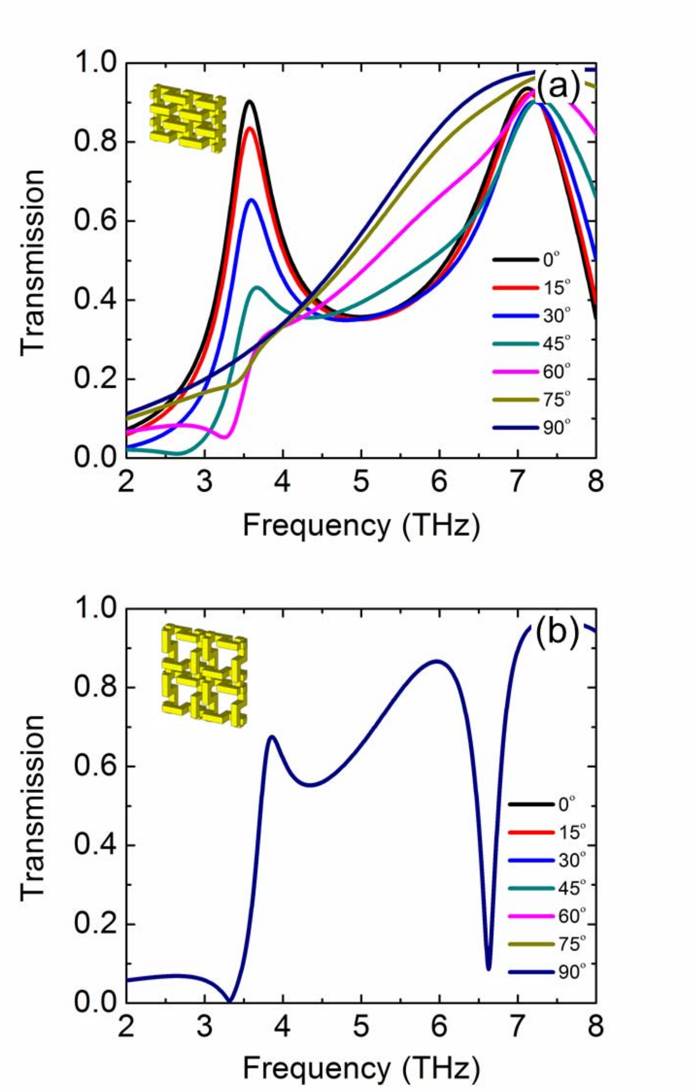

Figure 5.2 *Simulated transmission spectra of (a) a 1SE parallel-string meta-foil (w = 7.5 µm) and (b) a crossed meta-foil at different polarization states under normal incidence.*

Figure 5.2 shows the simulated transmission spectra of a 1SE parallel-string meta-foil (w = 7.5 µm) and a crossed meta-foil at different polarization states under normal incidence. Following previous nomenclature [66], 1SE indicates that the S-strings are equidistant and interconnecting lines are provided after each period. For a 1SE meta-foil, two dominant peaks appear in the transmission spectrum when the electric field points along S-strings in Fig. 5.2(a). The peak at 3.57 THz is a left-handed magnetic resonance, and the other peak at 7.12 THz is a right-handed electric resonance. Upon rotating the electric field to the direction perpendicular to the S-strings, the left-handed magnetic peak attenuates. When the electric field is exactly perpendicular to the S-strings, the magnetic resonance is lost. It indicates that the parallel-string meta-foils are strongly polarization-dependent left-handed metamaterials, which restricts their practical applications. For a crossed meta-foil, the transmission spectrum remains the same at different polarization states in Fig. 5.2(b). The peak at 3.86 THz is a left-handed magnetic resonance, which is confirmed by the following electric field distribution and parameter retrieval calculations. The magnetic resonance properties of crossed meta-foils can be tuned by changing the length of the resonator cell, for example, the open width w. Here, the crossed meta-foil is designed to be an all-metal polarization-independent left-handed metamaterial. In contrast to the parallel-string meta-foils, the structure of crossed meta-foils can be thought as unit cells fanning out from a "square coupling ring" in four directions. At their ends, there are again square coupling rings. In these rings, there is a circulating oscillating current. So, they are magnetic dipoles with the moment perpendicular to the plane. Therefore, the shape of the spectrum is also expected to change.

Figure 5.3 shows the measured transmission spectra of 1SE parallel string meta-foils (w = 7.5 μm) and crossed meta-foils at different polarization states under normal incidence. In the 1SE case, the well-known two resonance peaks [63-66] are found at 3.4 THz and 6.0 THz when the electric field is along the S-strings. When the polarization direction is rotated by 90°, the magnetic peak at 3.4 THz decays completely whereas the electric peak at 6.0 THz shows a broad frequency-independent transmission feature. In contrast, the magnetic resonance peak of the crossed meta-foil that occurs at 3.75 THz remains exactly the same under different polarization states, in excellent agreement with the simulated results shown in Fig. 5.2. The blue-shift of magnetic resonance from 3.4 to 3.75 THz is due to the reduction of the capacitance between S-strings bordering the large 20 μm gap. The broad electrical resonance feature between 4.5 and 8 THz remains polarization-independent as well. It will be commented on in more detail below. Small residual discrepancies between experimental and simulated results regarding positions, heights and widths of resonance peaks are thought to be mainly due to small imperfections in both fabrication and characterization that were ignored in simulations.

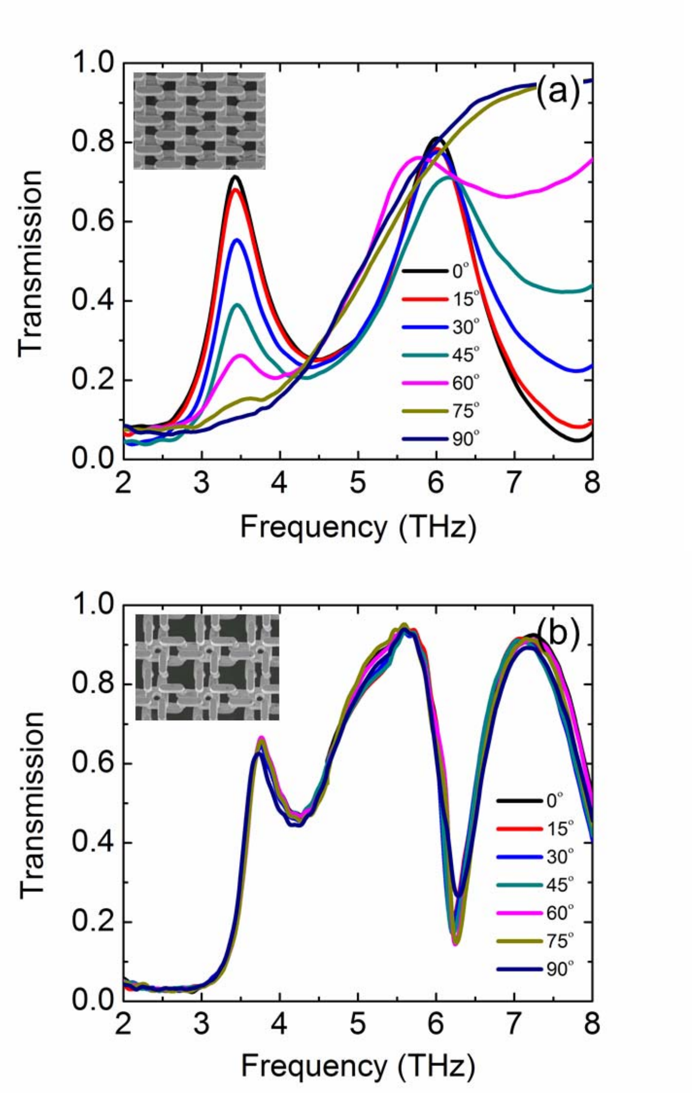

__Figure 5.3__ Measured transmission spectra of (a) a 1SE parallel-string meta-foil (w = 7.5 μm) and (b) a crossed meta-foil at different polarization states under normal incidence.

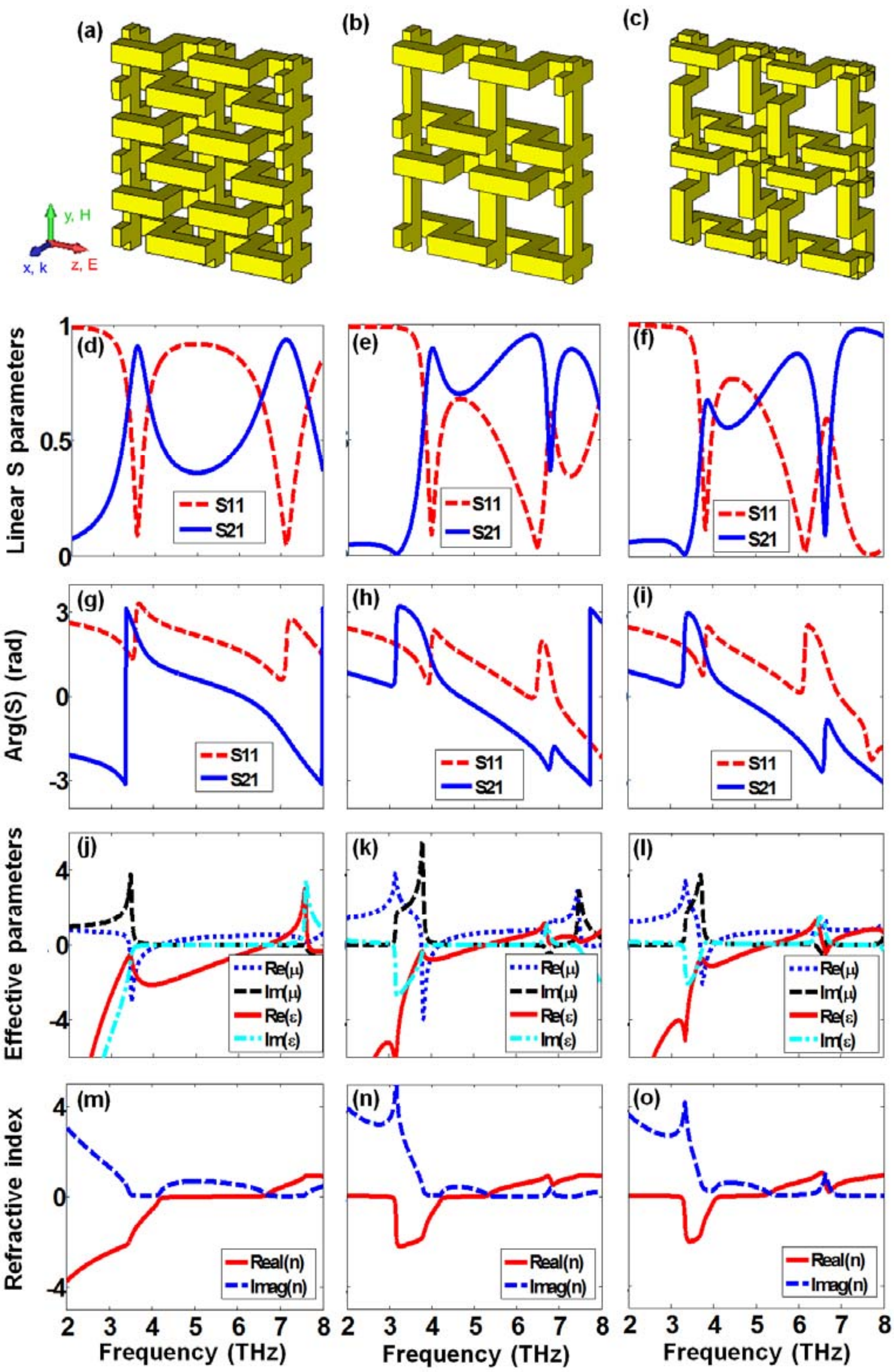

Figure 5.4 *Transition from 1SE over 1SP to crossed meta-foil. A given column shows the geometry of the investigated structures in the first row and then the frequency dependence of both the magnitude and phase of the linear S parameters describing transmission (S21) and reflection (S11), the retrieved constitutive parameters, and refractive index.*

Figure 5.4 presents central results of parameter retrieval calculations carried out using the method described by *Chen et al.* [70], which is the same method used in Chapter 4. These calculations were performed not only for the crossed meta-foil, but also for the cases of the 1SE and 1SP meta-foil because it allows us to track the transition from a 1SE to a crossed meta-foil and, thus, gain insight into the reason for the apparent difference between the 1SE and the crossed meta-foil. In case of the crossed meta-foil, the negative refractive index within the magnetic resonance between 3.7 THz and 4.0 THz moves back to zero for decreasing frequencies whereas it remains negative in 1SE meta-foils [63]. The first column of Fig. 5.4 shows the geometry of the 1SE meta-foil, its spectrum (both magnitude and phase), and retrieval results regarding the refractive index and the constitutive parameters relative complex permittivity ε and permeability μ. In the second column, we have transformed the 1SE into a 1SP meta-foil in which the distance between pairs of S-strings is increased from 5 μm to 20 μm. In accordance with Fig. 7 of [66], the frequencies of the magnetic and electric peaks shift up and down, respectively. Moreover, as the gap between pairs of S-strings has become much larger, both electric and magnetic excitations have become weaker entailing the change of the real part of refractive index from a negative value to zero. Finally, in the third column, we replace interconnecting lines by pairs of S-strings to obtain the crossed meta-foil. This last modification can also be described as superposing a second identically modified 1SP meta-foil onto the first one after rotating it by 90°. So, changes of refractive index and constitutive parameters from 1SE (1st column) to the crossed meta-foil (3rd column) are mainly determined by the gap between adjacent pairs of S-strings in both y and z direction. This transition leads to a reduction of the total magnetic moments as well as a dilution of the average plasma density with the ensuing vanishing of the real part of the refractive index. Negative permittivity and negative permeability values are simultaneously obtained between 3.7 THz and 4.0 THz resulting in the refractive index being negative in that bandpass. It can also be seen that the deep dip at 6.25 THz is a stop-band due to $\mathrm{Re}(\varepsilon) \leq 0$ and $\mathrm{Re}(\mu) > 0$ superposed on a broad and growing electrical transmission feature expected for high frequency short wavelengths above the plasma frequency. In conclusion, crossed meta-foils are confirmed to be left-handed metamaterials in the range from 3.7 THz and 4.0 THz.

In order to further understand the performance of crossed meta-foils, we investigate the electric field distribution through numerical simulation. As we can see in Fig. 5.5, at 3.86 THz, the adjacent S-strings are greatly excited with opposite field indicating strong charging of the capacitors formed by the b-legs of adjacent S-strings, and, thus, high amplitudes of oscillations in the LC loops creating the magnetic resonance. Note that in this magnetic resonance case the individual S-strings are at approximately the same potential level with adjacent strings oppositely charged, which coincides with the results of conventional parallel-string meta-foils discussed in Chapter 4.

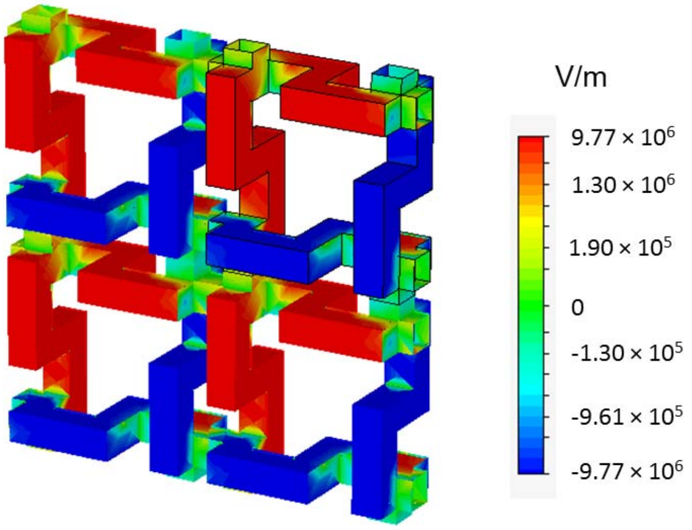

***Figure 5.5** Electric field distribution of a crossed meta-foil at the magnetic resonance.*

Furthermore, we also investigated the dependency of the magnetic resonance of crossed meta-foils on the angle of incidence in Fig. 5.6. The incidence angle is defined as the angle between the normal to the meta-foil y-z plane and the wave vector k. Figure 5.6 shows the magnetic resonance of crossed meta-foils change little when the incident angle varies from 0° to 50°, which indicates the feasibility of practical applications at curved surfaces. Crossed meta-foils can be tailor-made to virtually any shape, bent and wrapped around objects to hide and shield them from electromagnetic radiation, thus becoming true metamaterials on curved surfaces.

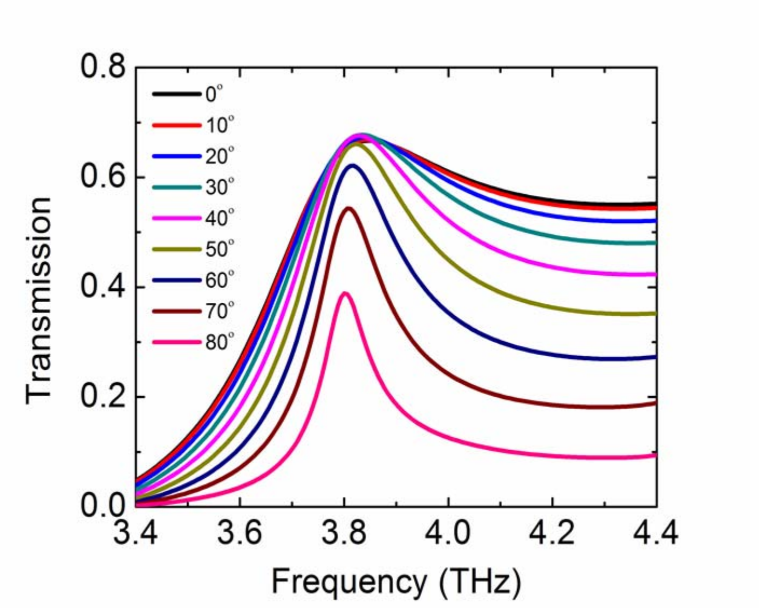

Figure 5.6 *Dependency of magnetic resonance of a crossed meta-foil on incidence angle.*

5.3 Conclusion

In conclusion, upon investigating the polarization-dependent properties of conventional parallel-string meta-foils, crossed meta-foils have been proposed, fabricated and demonstrated experimentally and numerically to be a polarization-independent left-handed metamaterial.

Chapter 6

Conjugated Rosette THz Chiral Meta-foils

6.1 Introduction

> "*I call any geometrical figure, or group of points, chiral, and say it has chirality, if its image in a plane mirror, ideally realized, cannot be brought to coincide with itself.*" Lord Kelvin (1904) [144].

In chemistry, biology and pharmaceuticals, chiral molecules are an important context. Many biologically active molecules, such as the naturally existing amino acids, enzymes and sugars, are chiral. The chirality of these natural chiral materials is relatively low. Researchers started to build the artificial chiral 'molecules' [145], such as helical coils. The studies of chiral media in the microwave region have found applications in many areas such as antennas, polarizers and waveguides [146].

From the electromagnetic point of view, the electromagnetic wave propagation in chiral materials satisfies the following constitutive equation [71]:

$$\begin{pmatrix} D \\ B \end{pmatrix} = \begin{pmatrix} \varepsilon_0\varepsilon_r & -i\kappa/c \\ i\kappa/c & \mu_0\mu_r \end{pmatrix} \begin{pmatrix} E \\ H \end{pmatrix} \tag{6-1}$$

where κ is the dimensionless chirality parameter which measures the effect of cross-coupling between electric and magnetic fields.

Due to the existence of κ, the degeneracy of the two circularly polarized waves is broken; i.e., the refractive index is increased for one circular polarization and reduced for the other. The refractive indices of right-handed circularly polarized (RCP, +) and left-handed circular polarized (LCP, -) waves are given by:

$$n_{\pm} = \sqrt{\varepsilon_r \mu_r} \pm \kappa = n \pm \kappa \tag{6-2}$$

If the chirality κ is strong enough, negative refraction may occur for one circularly polarized wave even when both ε_r and μ_r are positive, while for the other circular polarization the refractive index remains positive.

A chiral medium has two important properties called optical activity and circular dichroism. Optical activity is the ability to rotate the plane of polarization of electromagnetic waves. It is characterized by the polarization azimuth rotation angle of elliptically polarized light:

$$\theta = \frac{1}{2}\left[\arg\left(T_{++}\right) - \arg\left(T_{--}\right)\right] \tag{6-3}$$

where T_{++} and T_{--} are the transmission coefficients for RCP and LCP waves, respectively. Circular dichroism is the ability to different transmissions of RCP and LCP waves. It is characterized by the ellipticity angle of the transmitted waves:

$$\eta = \arctan\left[\frac{\left(\left|T_{++}\right| - \left|T_{--}\right|\right)}{\left(\left|T_{++}\right| + \left|T_{--}\right|\right)}\right] \tag{6-4}$$

Tretyakov and Pendry connected chirality and metamaterials together. Tretyakov *et al.* [72] discussed the possibility of realizing negative refraction by chiral nihility. Pendry [73] discussed in general the possibility to achieve negative refraction in chiral metamaterials, and proposed a practical chiral model with twisted Swiss rolls working in the microwave region. Ever since then, chiral metamaterials (CMMs) [147, 148] become a new research field as an alternative route to achieve negative refraction.

Parameter retrieval of chiral media is an important technique to characterize the EM properties and identify the negative refractive behavior of metamaterials [147, 149]. Consider a circularly plane wave normally incident onto a CMM slab with thickness d, refractive index $n_{\pm}$, and impedance Z for the RCP/LCP waves as shown in Fig. 6.1. The amplitude of incident RCP/LCP electric field is assumed to be unity. The amplitudes of the transmitted and reflected waves are $T_{\pm}$ and $R_{\mp}$; those of the forward and backward propagating waves inside the slab are $T_{\pm}^{'}$ and $R_{\mp}^{'}$, respectively.

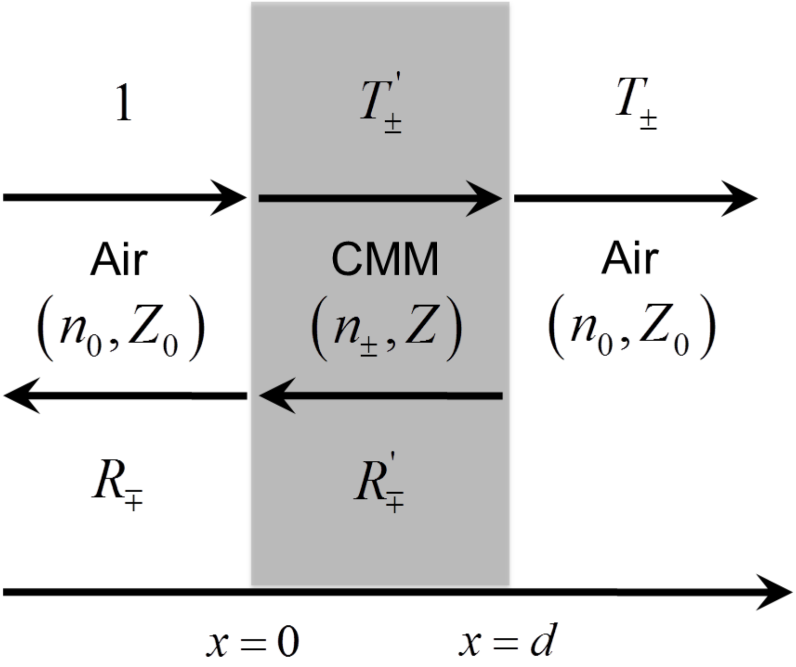

Figure 6.1 *Schematics of the transmission and reflection coefficients of a circularly polarized plane wave normally incident on a CMM slab.*

Applying the condition of continuity of tangential electric and magnetic fields at the first interface ($x=0$),

$$1+R_{\pm}=T_{\pm}^{'}+R_{\pm}^{'} \tag{6-5}$$

$$1-R_{\pm}=\frac{T_{\pm}^{'}-R_{\pm}^{'}}{Z} \tag{6-6}$$

Similarly at the second interface ($x=d$),

$$T_{\pm}^{'}e^{ik_{\pm}d}+R_{\pm}^{'}e^{-ik_{\mp}d}=T_{\pm} \tag{6-7}$$

$$\frac{T_{\pm}^{'}e^{ik_{\pm}d}-R_{\pm}^{'}e^{-ik_{\mp}d}}{Z}=T_{\pm} \tag{6-8}$$

where $k_{\pm}=k_0\left(n\pm\kappa\right)$.

Using the above equations, we can get the transmission and reflection coefficients:

$$T_{\pm}=\frac{4Ze^{ink_0d}e^{\pm\kappa k_0d}}{\left(1+Z\right)^2-\left(1-Z\right)^2e^{2ink_0d}} \tag{6-9}$$

$$R=R_{\pm}=\frac{\left(1-Z^2\right)\left(e^{2ink_0d}-1\right)}{\left(1+Z\right)^2-\left(1-Z\right)^2e^{2ink_0d}} \tag{6-10}$$

And then the impedance and refractive index can be calculated:

$$Z=\pm\sqrt{\frac{\left(1+R\right)^2-T_+T_-}{\left(1-R\right)^2-T_+T_-}} \tag{6-11}$$

$$n_{\pm}=\frac{i}{k_0d}\left\{\log\left[\frac{1}{T_{\pm}}\left(1-\frac{Z-1}{Z+1}R\right)\right]\pm 2m\pi\right\} \tag{6-12}$$

The sign of the square root in Eq. (6-11) and the multi-branches in Eq. (6-12) need to be chosen carefully according to the energy conservation principle, i.e. $\text{Re}\left(z\right)\geq 0,\ \text{Im}\left(n\right)\geq 0$. Once Z and $n_{\pm}$ are calculated, the other parameters can be identified subsequently, $\kappa=\left(n_+-n_-\right)/2$, $n=\left(n_++n_-\right)/2$, $\mu=nZ$, $\varepsilon=n/Z$.

Actually, we have another route to get the retrieval results. Refining $T=\sqrt{T_+T_-}$ and $R=R_{\pm}$, T and R can be written as:

$$T = \frac{4Ze^{ink_0 d}}{(1+Z)^2 - (1-Z)^2 e^{2ink_0 d}} \tag{6-13}$$

$$R = R_{\pm} = \frac{(1-Z^2)(e^{2ink_0 d} - 1)}{(1+Z)^2 - (1-Z)^2 e^{2ink_0 d}} \tag{6-14}$$

These equations are exactly the same as those for the ordinary nonchiral metamaterials (Eqs. (2-4) and (2-5) in Chapter 2.2). Therefore, we can get n, Z, ε, μ by the traditional retrieval procedure for the nonchiral metamaterials.

Rearranging Eq. (6-13), we can obtain

$$\kappa = \frac{-i}{2k_0 d} \ln\left(\frac{T_+}{T_-}\right) = -\frac{-i}{2k_0 d} \ln\left(\frac{|T_+| e^{i\phi_+}}{|T_-| e^{i\phi_-}}\right) \tag{6-15}$$

where $\phi_{\pm}$ are the phase of $T_{\pm}$.

From Eq. (6-15), we have

$$\operatorname{Re}(\kappa) = \frac{\phi_+ - \phi_- + 2m\pi}{2k_0 d} \tag{6-16}$$

$$\operatorname{Im}(\kappa) = \frac{\ln|T_-| - \ln|T_+|}{2k_0 d} \tag{6-17}$$

where the integer m is determined by the condition of $-\pi < \phi_+ - \phi_- + 2m\pi < \pi$. And then the refractive index can be directly got by Eq. (6-2). Besides, we note that the real and imaginary parts of κ relate to the azimuth rotation angle θ and the circular dichroism η, respectively.

CMMs possess a rich variety of electromagnetic properties, such as optical activity, circular dichroism and negative refraction, making them as ideal candidates for functional elements in optical setups. In order to realize these EM properties, many chiral structures, such as twisted rosettes [74, 75, 150], U-shaped split-ring resonators [78, 151, 152], twisted crossed-wires [77, 153, 154], conjugated gammadions [155-157] and complementary designs [158, 159], have been reported. Most of these CMMs were fabricated in the GHz or near infrared frequency regimes using dielectric materials for various support functions, such as spacers between metal layers, matrices for embedding metallic resonator structures, or as substrates. Some CMM designs were also investigated at terahertz frequencies [76, 152, 156, 160-162].

THz meta-foils [63-66] have been introduced as an all-metal, self-supported, locally stiff, globally flexible mesh, the properties of which only depend on the geometric structure and the metal. Multi-band meta-foils in Chapter 4 have been demonstrated to exhibit simultaneously negative permittivity and negative permeability responses at multiple frequencies. Crossed meta-foils in Chapter 5 have been investigated as the polarization-independent left-handed metamaterials.

In this Chapter, we first merge chirality and meta-foils together to propose an all-metal, self-supported, free-standing chiral metamaterial, called a chiral meta-foil (CMF). We investigate both experimentally and numerically the conjugated rosette CMF properties, such as strong optical activity, circular dichroism, and negative refractive index with a high figure-of-merit (FOM). Flexible CMF opens up the possibility of extending metamaterials to real three-dimensional form or bulk metamaterials, allowing more potential designs and applications than metamaterials on rigid substrates.

6.2 Simulation, Fabrication and Characterization

Simulations of CMF are performed by the frequency domain solver of the CST Microwave Studio. In the simulation, the unit cell boundary condition is applied and the circularly polarized eigenwaves are directly used. Three-level photolithography with precise alignment and three repeated gold electroplating steps with accurate thickness control were employed to fabricate the CMF.

The fabricated CMF was characterized by terahertz-time-domain spectroscopy (THz-TDS) in a nitrogen purged chamber with a relative humidity less than 5%. Time-domain spectra of the co- and cross-polarization states of the CMF were measured in transmission mode by employing polyethylene polarizers (TYDEX) before and after the CMF. Transmission coefficients of the circularly polarized waves were then obtained from the linear polarization measurements using the following equation:

$$\begin{pmatrix} T_{++} & T_{+-} \\ T_{-+} & T_{--} \end{pmatrix} = \frac{1}{2}\begin{pmatrix} \left(T_{xx}+T_{yy}\right)+i\left(T_{xy}-T_{yx}\right) & \left(T_{xx}-T_{yy}\right)-i\left(T_{xy}+T_{yx}\right) \\ \left(T_{xx}-T_{yy}\right)+i\left(T_{xy}+T_{yx}\right) & \left(T_{xx}+T_{yy}\right)-i\left(T_{xy}-T_{yx}\right) \end{pmatrix} \tag{6-18}$$

where the first and second subscripts refer to the incident and transmitted waves, + and – refer to the RCP and LCP waves, and x and y refer to the two linearly polarized waves with the electric field polarized along two orthogonal directions [71] (see Chapter 3.4).

6.3 Results and discussion

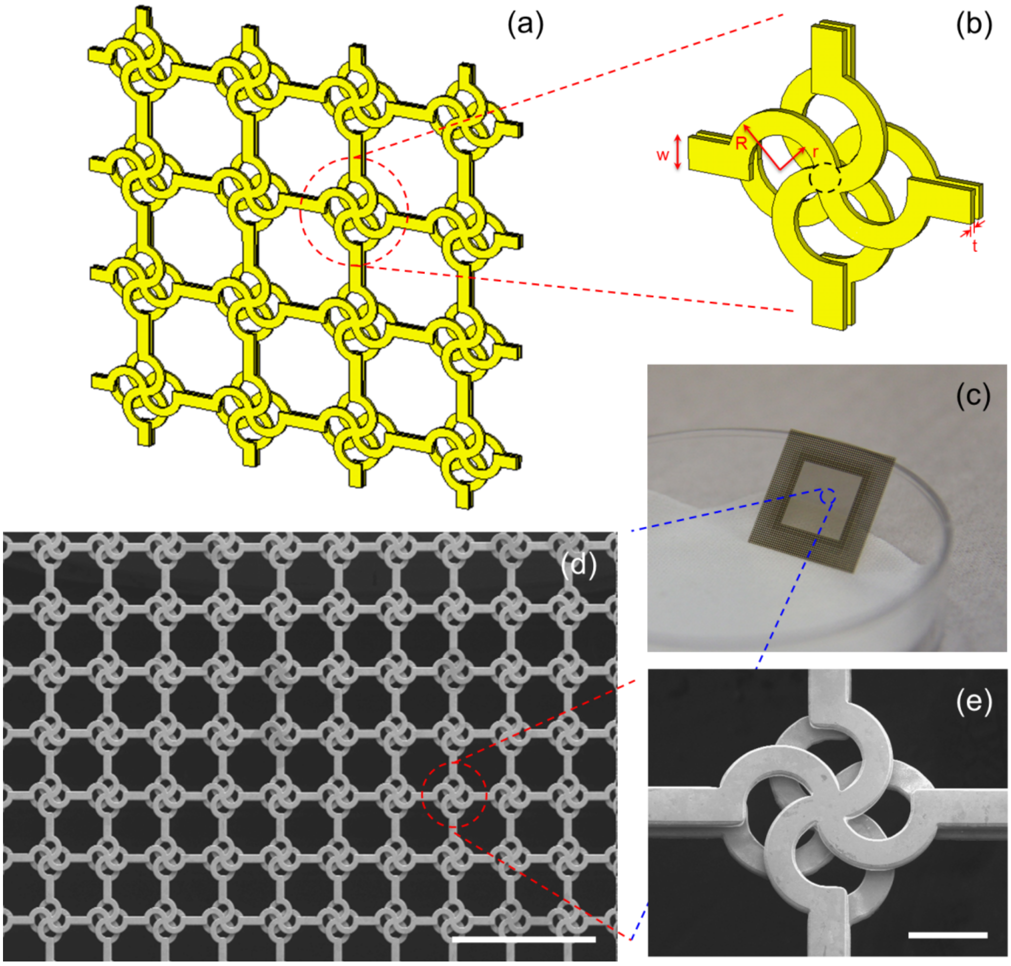

Figure 6.2 *(a) and (b) 3D schematics of the conjugated rosette CMF, and the geometry parameters are given by R = 40 μm, r = 24 μm, w = 22 μm, t = 5 μm and the unit cell size u = 200 μm. The black dotted lines mark the position of pillar. (c) Photograph of the CMF. (d) - (e) SEM images of the fabricated CMF. The scale bar is 500 μm in (d) and 50 μm in (e).*

A CMF is constructed by a square array of conjugated rosettes interconnected with metallic wires and pillars between rosettes as shown in Fig. 6.2. Metallic pillars are placed between the conjugated rosettes on the top and bottom layers to make the whole structure self-supported and free-standing, with a position highlighted by the black dotted lines in Fig. 6.2(b). Figure 6.2(c) shows a photograph of the CMF, in which the useful window is 10 mm × 10 mm × 0.015 mm (L × W × H). Figures 6.2(d) and (e) show scanning electron microscope (SEM) images of the fabricated CMF. The CMF can be viewed as a composite chiral metamaterial. Conjugated rosettes are arranged to break the mirror symmetry along the direction perpendicular to the metamaterial plane. The lack of mirror symmetry is an inherent property of our design, allowing cross-coupling between the electric and magnetic fields which creates a strong chiral response around the resonance frequencies. Furthermore, we select a conjugated structure because it has a relatively large chirality and at the same time a relatively weak electric resonance [163].

Figures 6.3(a) and (b) show the simulated and measured transmission coefficients as a function of frequency. In the simulation, the transmission of the LCP wave is higher than the RCP wave around a frequency of 1.21 THz, while the transmission of the LCP wave is much lower than the RCP wave around 1.41 THz. As shown in Fig. 6.3(b), the experimentally observed resonances at 1.21 THz and 1.38 THz are in good agreement with simulations. The circular dichroism, i.e., the difference between RCP and LCP transmission, reaches about 62% at 1.38 THz in the measured results. Note that small discrepancies exist between experiment and simulation, we conjecture that they are mainly due to the tolerance in the fabrication and characterization. Using the standard definition of the polarization azimuth rotation (Eq. (6-3)) and ellipticity (Eq. (6-4)), we calculate the polarization changes in a linearly polarized wave incident on the chiral meta-foils shown in Figs. 6.3(c)-(f). At the resonant frequencies of 1.21 THz and 1.41 THz, the azimuth rotation and ellipticity reach their maximum values, ($\theta = -12^\circ$, $\eta = -24^\circ$) and ($\theta = -104^\circ$, $\eta = 20^\circ$), respectively. Meanwhile, it is clearly observed that, in the middle of the two resonant frequencies, the ellipticity $\eta = 0$, which corresponds to a pure optical activity effect. That is, for a linearly polarized incident wave, the transmitted wave is still linearly polarized with a polarization rotated by an angle θ. For the CMF, we observe a polarization rotation of 10° with $\eta = 0$. The origin of the chiral response of the conjugated structures has been discussed by a procedure of transmutation from the simple Ω-particle chiral element to the conjugated chiral metamaterials [155, 163]. Magnetic or electric moments are induced by the electric or magnetic fields, respectively, of the incident electromagnetic wave in the antiparallel or parallel direction. The conjugated arrangement breaks the mirror symmetry in the direction perpendicular to the plane of the metamaterial, and thereby induces strong chirality around the resonance frequencies.

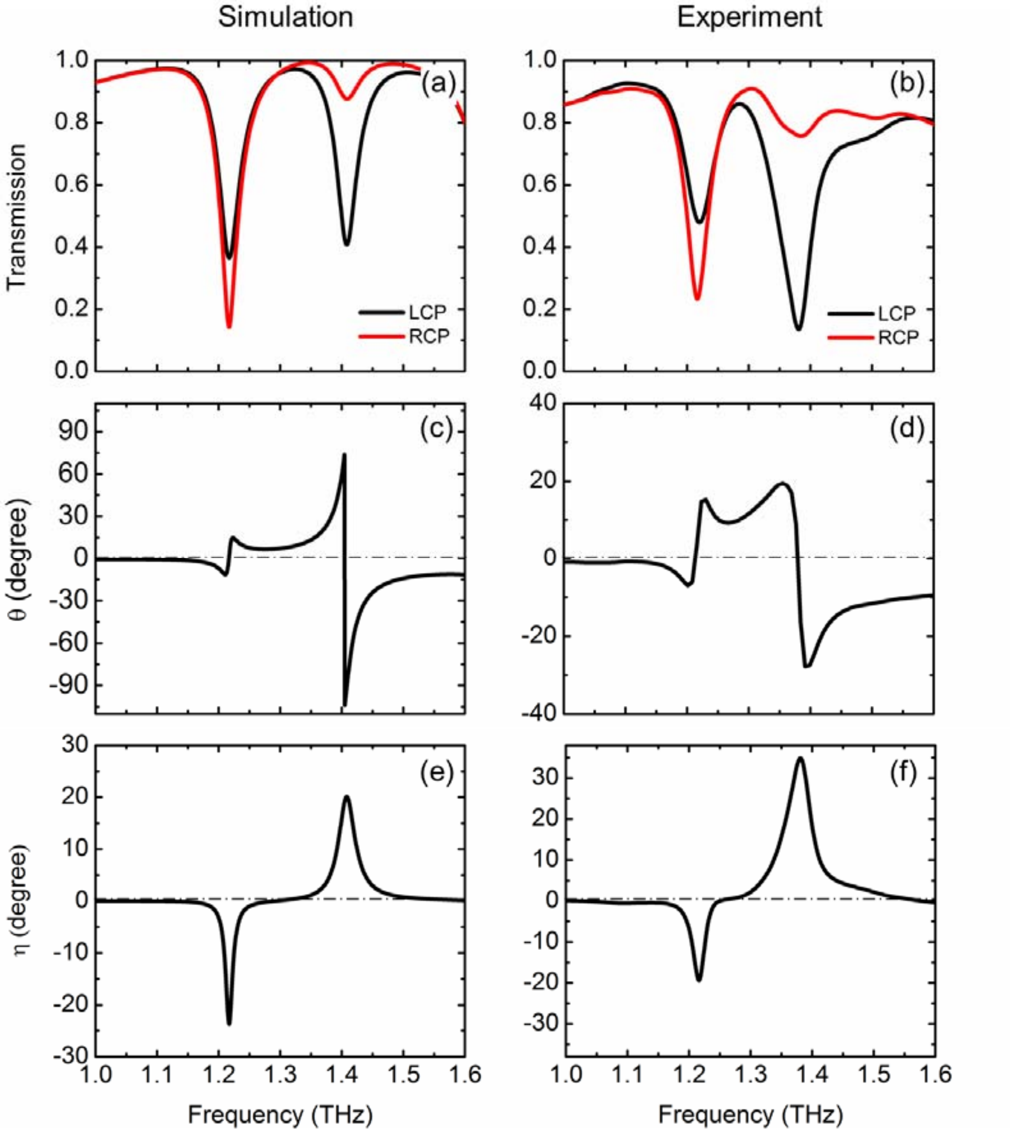

Figure 6.3 *Simulation (left) and experimental (right) results of the CMF. (a) and (b) show the transmissions of the LCP and RCP waves. (c) and (d) show the polarization azimuth rotation angle θ. (e) and (f) show the ellipticity η of the transmitted wave.*

Using the simulated transmission and reflection data, we calculate the effective constitutive parameters of the CMF [147, 149]. Parameter retrieval has been discussed in the introduction part of this Chapter. The strong chirality can easily push the refractive index of the RCP/LCP eigenwaves, $n_{\pm} = n \pm \kappa$, to be negative at the two resonances, especially at the higher resonance, seen in the shaded regions of Fig. 6.4 from 1.23 to 1.31 THz for n_{+} and from 1.42 to 1.49 THz for n_{-}. The amplitude of the chirality κ at off-resonance frequencies around 1.3 THz is about 0.3, which is enormous compared to natural materials such as sugar and quartz, where κ is around 10^{-5}. The efficiency of the negative refractive index is usually characterized by the figure of merit (FOM), which is defined as $FOM = -\mathrm{Re}(n)/\mathrm{Im}(n)$. For RCP light, the negative refractive index region around 1.21 THz has a maximum FOM = 2.8, while for LCP light, the negative refractive index region around 1.41 THz has a maximum FOM = 4.2. These values are much higher than those reported earlier [74, 75, 77, 78, 153-156]. Most chiral structures were fabricated on substrates such as flame-resistant grade 4 board or other photopolymers which have an associated large loss to decrease the FOM value. However, the CMF is an all-metal self-supported free-standing chiral metamaterial structure which properties are solely determined by the geometric structure and the metal properties. Since it is free from limitations imposed by the substrates, the CMF can be optimized to achieve a much higher FOM value to become a more suitable chiral design with a negative index.

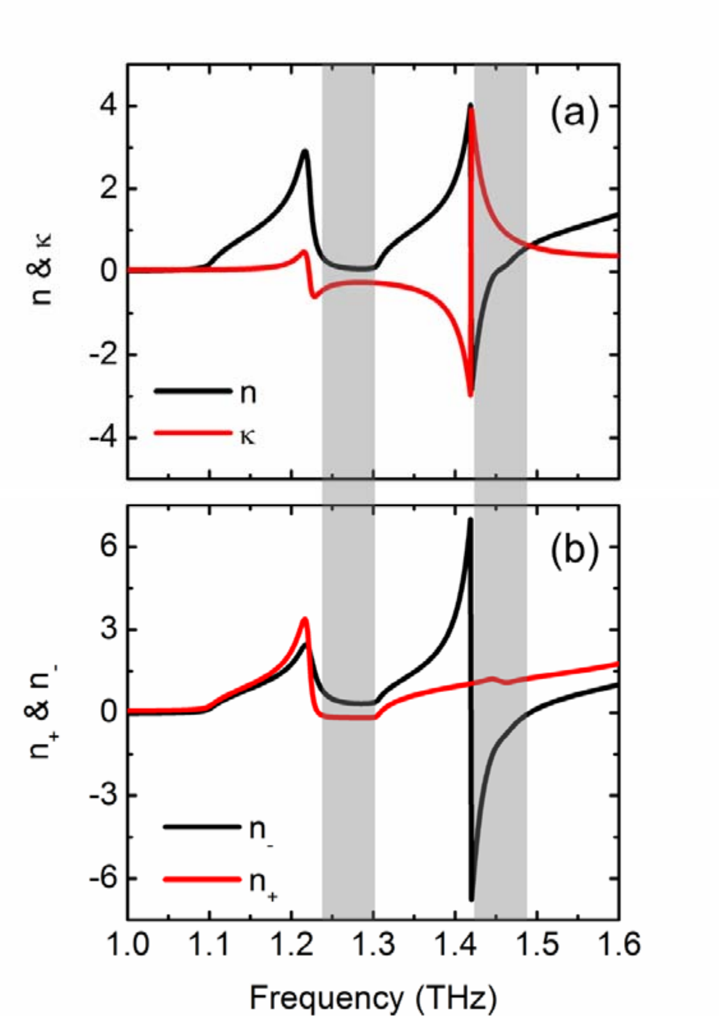

Figure 6.4 *Retrieved effective parameters of the CMF based on the simulation data. (a) Real parts of the refractive index* n *and chirality* κ *. (b) Real parts of the refractive indices for the LCP and RCP waves.*

6.4 Conclusion

In conclusion, we experimentally and numerically demonstrate a conjugated rosette, chiral meta-foil that exhibits strong optical activity, circular dichroism, and negative refractive index with a high figure-of-merit. Free-standing chiral meta-foils provide a unique approach to create a completely all-metal chiral metamaterial, which can be flexibly integrated with other terahertz functional materials and devices. Furthermore, all-metal bulk CMMs are possible to be realized by via a layer-by-layer method.

Chapter 7

THz Chiral Meta-foils as Broadband Circular Polarizers

7.1 Introduction

Circular optical dichroism, the differential absorption of right- and left-handed circularly polarized light, is a characteristic attribute of light and an important means of using light to study the structure and properties of chiral molecules [163]. While generally, 2D or 3D objects are called chiral if their mirror image at a line or a plane, respectively, cannot be transformed into the original by translations and/or rotations, many biologically relevant molecules such as naturally existing amino acids, enzymes and sugars are chiral and chiral molecules are also of great importance in chemistry, biology and pharmaceutics. However, in naturally chiral molecules the chirality is relatively low. Not surprisingly, artificial chiral 'molecules', such as helical coils, were thus studied with an aim to achieve augmented chiral effects [145, 146]. Combining chirality with metamaterials, chiral metamaterials have recently attracted considerable attention due to their exotic properties, such as giant optical activity as well as their potential to realize materials with negative refraction [72-78, 144-163]. In chiral metamaterials, strong magneto-electric coupling gives rise to an appreciably different optical response of left-handed (LCP) and right-handed circularly polarized (RCP) light. On the basis of this concept, chiral metamaterials have opened a new route to build circular polarizers with octave-wide frequency ranges of operation.

For conventional circular polarizers, two methods have commonly been used to generate circularly polarized light: (1) Bragg reflection using a cholesteric liquid crystal film [165, 166] and (2) a linear polarizer laminated with a quarter wave film [167]. However, their narrow band response at an a priori designed frequency seriously limits their integration into many devices and systems.

Recently, a gold helix photonic metamaterial [57, 168] was introduced and investigated as a compact and broadband circular polarizer. For light propagating along the helix axis, the structure was demonstrated to block circular polarization with the same handedness as the helices but to transmit the other, for a frequency range exceeding one octave. At the same time, three-dimensional bichiral plasmonic crystals [169, 170], tapered helices [171] and multi-helical structures [172, 173] have also been conceived and shown to further improve the performance of circular polarizers. However, the complex structure design and metallization make them challenging to be realized at arbitrary frequencies, for example, in the terahertz (THz) region. Although direct laser two-photon absorption writing [57, 168-173] and electro-less plating [174] can provide an effective method, there are still restrictions in meeting requirements of practical applications like the manufacturing of large areas or the need of a substrate which may limit the useful spectral range.

Twisted metamaterials [175, 176] were proposed based on stacked planar metasurfaces featuring parallel metallic rods realized with conventional lithographic techniques, suitably rotated from one layer to the next, to achieve the broadband circular polarization selectivity. They are much closer to practical applications and allow for much larger sample footprints due to an inherently simpler fabrication process. However, although very elegant in their design, such twisted stacked metasurfaces so far still cannot quite match the performance of helix-based metamaterials, as their extinction ratio is not yet high enough in four-layer structures. Although higher extinction ratios can be achieved by means of seven or more layers of twisted structures as shown in simulation, the fabrication becomes increasingly complex.

Lately, a miniature chiral beamsplitter based on gyroid photonic crystals was demonstrated to discriminate RCP and LCP light in a narrow band around 1.5 μm wavelength with a transmission of almost 50% [177].

As an alternative route to realizing high-contrast and broadband circular dichroic properties, we propose a chiral meta-foil that builds on the well-known meta-foil concept [63-66]. It combines the upright S-string architecture [68] with the distinctive feature of metallic transverse interconnects to form a self-supported, locally stiff, globally flexible space-grid. A strong left-handed magnetic resonance peak between 3 and 4.5 THz gave rise to a high transmission of electromagnetic waves. The platform of the meta-foil was further extended to the functional multi-band meta-foils that were experimentally and numerically demonstrated to achieve simultaneously negative permittivity and negative permeability responses at multiple frequencies as well as crossed meta-foils that are polarization-independent left-handed metamaterials, which are shown in Chapter 4 and Chapter 5. Conjugated rosette chiral meta-foils, the first product of meta-foils combined with chirality, exhibited strong optical activity, circular dichroism, and negative refractive index with a high figure-of-merit (FOM) at a narrow frequency range in Chapter 6.

The chiral meta-foil as introduced here is an all-metal, self-supported, free-standing chiral metamaterial assembled from simple half-loop structures that feature the same handedness. It can be derived from a conventional 1SE meta-foil by simply shifting interconnecting lines by half a unit cell length from row to row. Because of the direct coupling among these connected structures, the chiral meta-foil can effectively operate as three-dimensional structure with a broadband optical response. Its global flexibility lends it a further degree of freedom for shaping optical surfaces, most readily, with cylindrical contours of circular, elliptic, parabolic, and hyperbolic shape. This feature could be useful in relation to cylindrical source geometries as they occur, e.g., when light is scattered from a particle beam and its detection needs to be discriminated according to its circular polarization. Furthermore, it may play a role when circular polarizers need to conform to curved surfaces the design of which is dictated from other considerations.

In this Chapter, we demonstrate experimentally and numerically that high-contrast broadband circular polarization selectivity can be achieved by a chiral meta-foil in the THz region. The bandwidth of the dichroic response is about one octave at a center frequency of 2.4 THz, the ratio between LCP and RCP light is about 700% with the maximum transmittance being approximately 70%. Chiral meta-foils may be manufactured by imprinting and hot embossing in any frequency range, enabling cost-effective mass manufacture, and may so be extended to the higher infrared and optical frequencies as well, thus enabling their direct integration into current devices and systems.

7.2 Configuration of broadband chiral meta-foils

The construction principle of our chiral meta-foil is illustrated in Fig. 7.1. A simple rod, with length l = 90 µm, width w = 30 µm and thickness t = 17 µm, can produce strong, resonant anisotropy within the plane while being strictly non-chiral. The LCP and RCP transmissions are expected to be identical for normal incidence at all frequencies. Fractional-screw-like structures are made by stacking and connecting three of such planar non-chiral rods with a rotation angle of 90° between them, thus forming the basic building blocks of chiral meta-foils. Based on the direction of rotation from top to bottom, we define the right-turn structure and left-turn structure, respectively. By this specific rotation between adjacent layers, 3D chirality is achieved in these fractional-screw-like structures.

Stacking a large number of rods with sequential rotation is one way to achieve the broad operation bands and high extinction ratios [175]. In contrast, the chiral meta-foil we propose uses a different route: handed structures with the same handedness are assembled in the form of a closely coupled array to realize the desired high-contrast and broadband properties. Thereby, a right-handed chiral meta-foils' molecule is assembled by combining two right-turn structures as illustrated in Fig. 7.1(a). Many right-handed chiral meta-foils' molecules are then joined together to form the right-handed chiral meta-foil. The same construction principle applies to left-handed chiral meta-foils as shown altogether in Fig. 7.1(b) where, in chemical terminology, line (b) represents the enantiomer version of the structures of line (a) [178]. Topologically, the unit cell corresponds to two split-rings cross-coupled to a common capacitor as schematically illustrated in Fig. 7.1(c) and (d) depicting the corresponding wire frame and topological diagrams of the unit cell, respectively. In simplest terms, the structure of a chiral meta-foil results from a shift of the interconnecting lines of a conventional 1SE meta-foil by half a unit cell length from row to row.

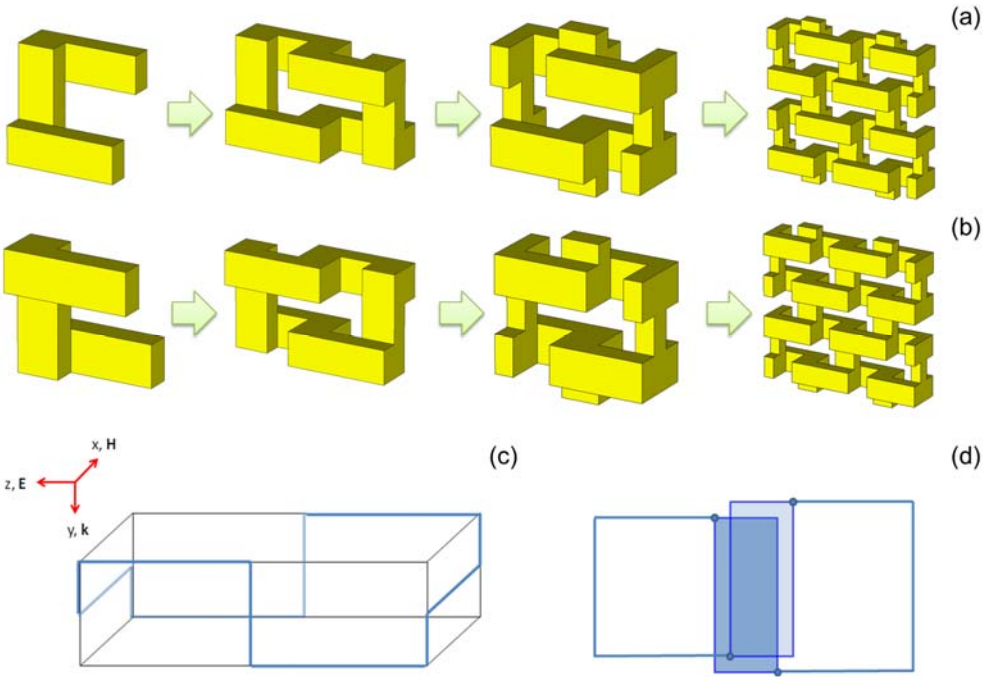

Figure 7.1 *Configuration of left-handed (a) and right-handed (b) chiral meta-foils. A wire frame schematic (c) and a topological schematic (d) of chiral meta-foils' unit cell.*

7.3 Results and discussion

Simulations of crossed meta-foils are performed by the frequency domain solver of the CST Microwave Studio. In the simulation, the unit cell boundary condition is applied and the circularly polarized eigenwaves are directly used.

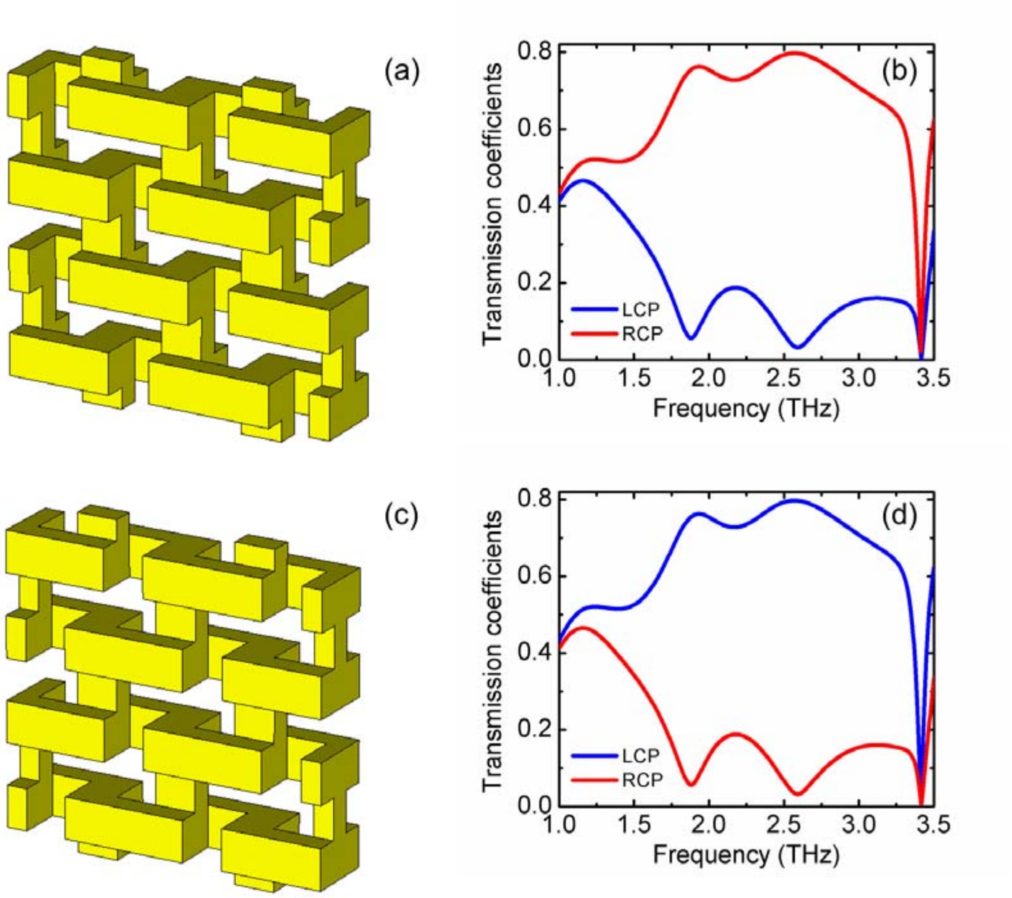

***Figure 7.2** Simulation results of broadband chiral meta-foils. 3D schematics of right-handed (a) and left-handed (c) chiral meta-foils. The simulated transmission spectra of the LCP and RCP waves for the right-handed (b) and left-handed chiral meta-foils at normal incidence.*

Figures 7.2(a) and (c) show schematic 3D diagrams of the right-handed and left-handed chiral meta-foils, and Figures 7.2(b) and (d) show the corresponding simulated transmission spectra of the LCP and RCP waves, respectively. For right-handed chiral meta-foils, the RCP waves are preferentially transmitted within the bandwidth of operation from about 1.5 THz to 3.4 THz, whereas the LCP waves are almost blocked. The associated (numerically simulated) circular dichroism, which is reflecting the difference between the transmission spectra of two circular polarizations (maximum difference divided by maximum transmission), can reach about 95 % in the chiral meta-foil. This clearly exceeds the previously reported performance of the seven layer rotated metasurfaces [175]. As expected from symmetry, the left-handed chiral meta-foils show the same transmission spectra, except that the spectra for the LCP and RCP waves are exchanged.

The terahertz chiral meta-foils are manufactured using three-level photolithography with precise alignment and three repeated gold electroplating steps with accurate thickness control. All fractional-screw-like structures are linked together and self-supported, assuring a remarkably high degree of robustness of our chiral meta-foils. After being released from the substrate, the chiral meta-foils turn into all-metal, self-supported, free-standing metamaterials (see Chapter 3). Figure 7.3(a) shows photographs of flat as well as deliberately bent chiral meta-foils. The useful window of chiral meta-foils that is available for transmission is $10 \times 10 \times 0.051$ mm^3 (L × W × H). Figures 7.3(b)-(d) show scanning electron microscope (SEM) images of these fabricated meta-foils.

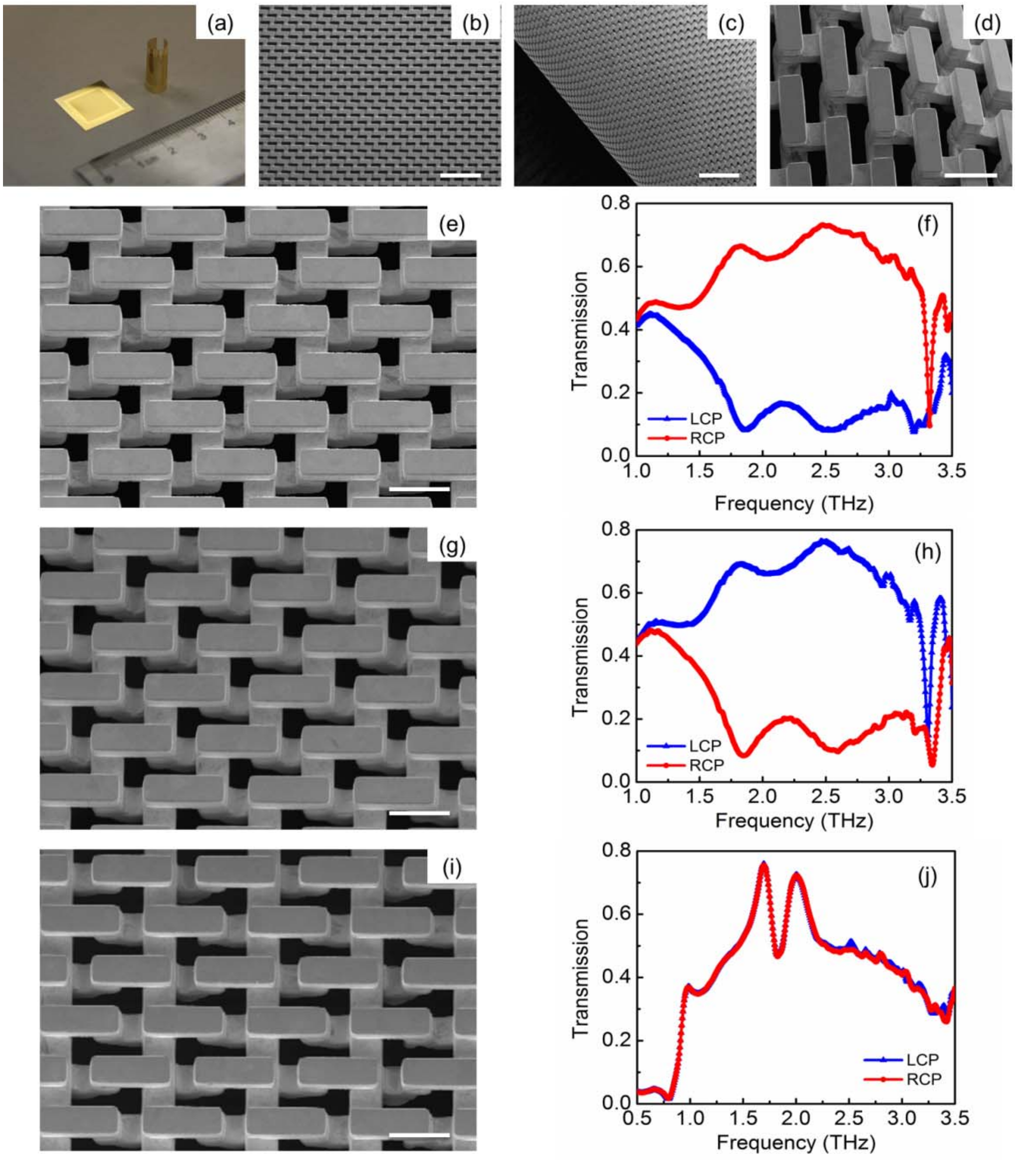

Figure 7.3 *Experimental demonstration of broadband chiral meta-foil. (a) Photographs of the flat and deliberately bent chiral meta-foils. (b-d) Scanning electron microscopy images of the fabricated chiral meta-foils. Scale bar is 300 µm in (b) and (c), 80 µm in (d), respectively. (e) Scanning electron microscopy images of the right-handed chiral meta-foil, Scale bar in (e) is 80 µm. (f) The measured transmission spectra of LCP and RCP waves for the right-handed chiral meta-foil. (g) Scanning electron microscopy images of the left-handed chiral meta-foil, Scale bar in (g) is 80 µm. This structure is an enantiomer of (e) (h) The measured transmission spectra of LCP and RCP waves for the left-handed chiral meta-foil. (i) Scanning electron microscopy images of the conventional 1SE meta-foil, Scale bar in (i) is 80 µm. (j) The measured transmission spectra of LCP and RCP waves for the 1SE meta-foil showing that the conventional 1SE meta-foil does not exhibit any dichroism at all as it is the racemic modification of structures (e) and (g).*

The high-contrast and broadband properties of chiral meta-foils are experimentally demonstrated by terahertz-time-domain spectroscopy (THz-TDS) (see Chapter 6). Figures 7.3(e)-(h) show SEM images and the measured transmission spectra for the two circularly polarized terahertz waves in the right-handed and left-handed chiral meta-foils, respectively. As predicted by simulations, our terahertz chiral meta-foils experimentally support circular polarization selectivity over a broad bandwidth from about 1.5 THz to 3.4 THz, and circular dichroism can experimentally reach about 85 %. The measured results in Figs. 7.3(f) and (h) are in very good agreement with the simulated results in Figs. 7.2(b) and (d). Some small discrepancies between experiments and simulations are mainly due to the tolerances in the fabrication and characterization.

For comparison purposes, Figures 7.3(i) and (j) show that a conventional equidistant 1SE meta-foil does not exhibit any circular dichroism at all. As, in this case, there are equal numbers of identical right-handed and left-handed unit cells, the circular polarization selectivity arising from them is completely cancelling out mutually, making the measured transmission spectra of RCP and LCP identical. In chemical terminology, this corresponds to the racemic modification [178]. In Figs. 7.4(a) and (b), we show the influence of the capacitor in the ring and the thickness of the conductors on the transmission spectra. We observe that increasing the capacitance leads to a narrower and higher broadband peak whereas an enlargement of the conductor thickness shifts the peak to higher frequencies. This clearly offers an additional degree of designing capability with respect to tuning the frequency and spectral shape.

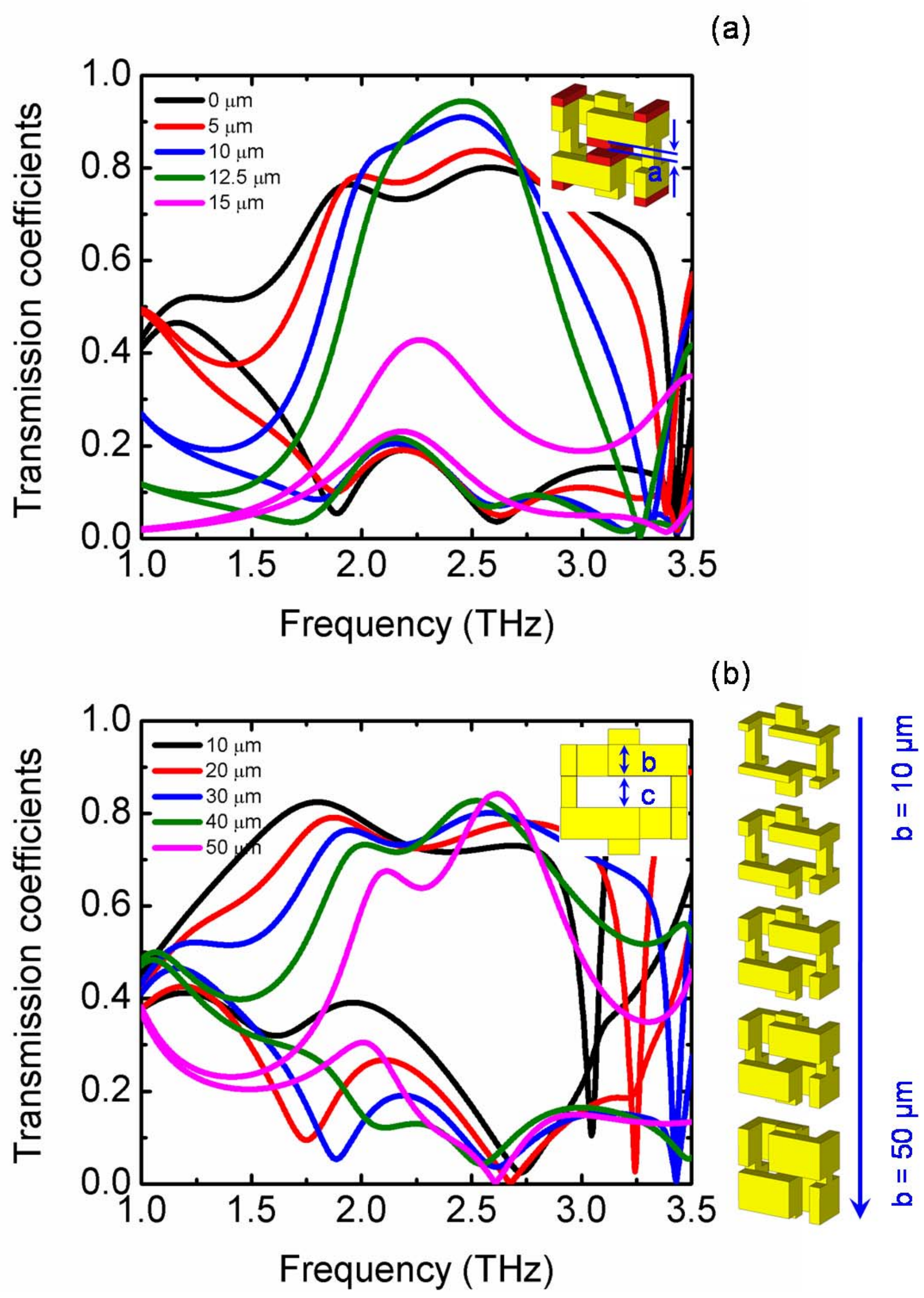

Figure 7.4 *Influence of capacitance and conductor thickness. (a) a changes from 0 to 15 μm. (b) Unit-length u = 2b+2c = 120 μm keeps constant while b changes from 10 to 50 μm.*

In a conventional meta-foil, the topology of a unit cell corresponds to two oppositely inclined split-rings cross-coupled via a common capacitor. Our chiral meta-foil is structurally very similar, but for a small, yet crucial difference: the interconnecting coupling lines are shifted by half of an S-length from row to row. This is crucial, as it creates the right- or left-handed structure. Indeed, looking at the structure depicted in Fig. 7.1(a) or (b), we can see that, starting at any point of the structure and following the path of a propagating wave going into the meta-foil the path describes a right-handed screw in Fig. 7.1(a) or a left-handed screw in Fig. 7.1(b). The shape of the spectral response of a chiral meta-foil is completely different from the conventional meta-foil. Whereas the latter exhibits a magnetic negative-μ resonance which has a relative bandwidth of about 10%, the present chiral meta-foil, in contrast, features a much broader circular-polarization-selective pass-band with a spectral width of more than one octave superposed on which magnetic resonant peaks can be observed.

To describe the basic excitation of the broadband chiral meta-foil, let us consider a plane circularly polarized wave incident on the chiral meta-foil in x-direction. Let us further assume the incident circularly polarized wave to be decomposed, as usual, into two orthogonal, linearly polarized waves. There is thus a phase shift of $\pi/2$ or $-\pi/2$ between the orthogonal components to produce right-circular or left-circular light, respectively [179, 180]. We further assume the electric field vector of the leading component to be oriented in the direction of the S strings of the meta-foil (z-direction). Then, the related H vector will point normal to the loops (y-direction) and excite them fully magnetically. This magnetic induction leads to an LC oscillation. The current influenced by the electric field thus flows in the same direction. The electric field vector of the phase shifted orthogonal component, the trailing wave, will then point in a direction normal to the loops (y-direction) and the related H field vector will be along the S strings (z-direction). In this case, the loop area projected onto a plane perpendicular to H is comparatively small, so magnetic induction plays a smaller role. To understand the dichroism, we note that, depending on the material, the electric field of the incident wave sees a right-handed or left-handed inclined split-ring. It is the interaction with this inclined split-ring that brings about the observed circular dichroism. During the first half wave of the leading component, the electric field excites a current along the top rods of the structure such that the capacitor between rods is charged. After the first quarter wave, the orthogonal trailing component helps to direct the current further along the split-ring combined with the discharge of the capacitor, provided the circular polarization corresponds to the handedness of the inclined split-ring. After the first half wave, the direction of electric excitation and the direction of the current flow are inverted, and, due to the axial symmetry of the unit cell, the second half of the ring current is performed such that, after one wave, one circular current flow is completed. If the handedness of the inclined split-rings and the circular polarization do not match, the field of the trailing wave excites a current opposite to the discharge current of the capacitor, thus partly compensating current flows and reducing transmission. While we have argued that the magnetic field of the trailing component can barely excite loops, the magnetic field of the leading component does. However, this does not distinguish between right- or left-circular excitation and, thus, plays no role in the circular polarization selectivity. In detail, during the first quarter wave of the leading component, the electric field and the induced electromagnetic field point into the same direction while they are opposite in the second quarter. Depending on the position of the spectral resonance, the magnetically induced current can be larger or smaller, thus leading to the waviness of the transmission spectra we observe.

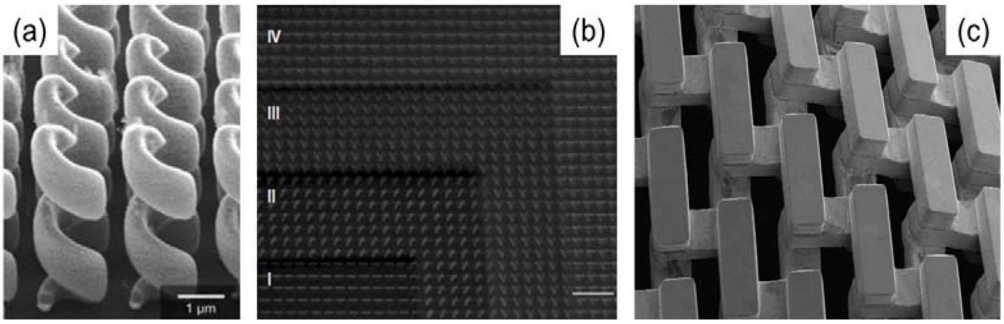

Figure 7.5 *(a) Helix photonic metamaterials [57]. (b) Twisted metamaterials [175]. (c) Broadband chiral meta-foils.*

While having some similarities to helical [57] as well as to twisted [175] metamaterials, our chiral meta-foil is, however, distinctly different from both. The chiral meta-foil features inclined split-rings that may also be called fractional screws. The crucial property is that the two fractional screws making up a unit cell are oriented such that they alternatingly accommodate the two half waves of the incident light as illustrated in Fig. 7.1, thus supporting the propagation of a like-handed wave. In contrast, in a helix, short circuiting currents are set up in the like-handed case that block the incoming wave [57]. The thickness of the layer filled with helices – or the height of a helix – is about one half wavelength. Owing to the geometric difference, the response of the chiral meta-foil is thus completely different from that of the gold helix as it transmits the wave of like handedness. Compared to twisted metamaterials, the chiral meta-foil is similarly composed of metal rods that have orientations differing by 90° from each other. However, in the chiral meta-foil these rods are galvanically coupled, not only capacitively/inductively as between insulated layers in twisted metamaterials (which are basically a stack of wire grid filters with different angular position of each layer). Considering a single layer of a twisted metamaterial, the E field vector perpendicular to the rods is transmitted. As the next layer is rotated, the transmitted E field vector also needs to rotate. The handedness of the rod rotation and the E field vector rotation then is identical. Therefore, they pass like-handed polarization. In chiral meta-foils, however, the selectivity between right- and left-handed circular polarizations is significantly larger than in twisted metamaterials. Moreover, both helical and twisted metamaterials need substrates and/or embedding matrices. This may restrict the useful spectral range. In the case of the twisted metamaterial, the optimum distance between layers is L = 120 nm for a useful spectral range of 600-1400nm, leading to a total thickness of about one wavelength. It thus does not seem immediately obvious that and how this concept may be extended to larger wavelengths into the THz range.

Compared with the gyroid photonics crystal [177], the chiral meta-foil is fundamentally different in at least two aspects, namely, the bandwidth and the thickness. Regarding the former, the chiral meta-foil features a bandwidth of about one octave whereas the gyroid photonics crystal is reported to have a relative bandwidth of about 1/60. So, the relative bandwidth of the chiral meta-foil is larger by a factor of 120. As for the thickness, the chiral meta-foil is 51 μm thick and the shortest wavelength in the bandpass is 88 μm, so, it is less than one wavelength thick in propagation direction whereas the gyroid photonics crystal prism is about 32 wavelengths thick at the point of incidence. As a corollary, we note here due to their small thickness, the chiral meta-foils should be regarded in the spirit of an effective meta-surface rather than a bulk meta-material for which one would be able to identify an effective chiral parameter κ.

While the chiral meta-foils studied were produced by means of three-level photolithography, an important aspect is that they may also be manufactured by plastic moulding show in Fig. 7.6. Two parts of either a mould insert for injection moulding or two parts of a hot embossing die yield the plastic meta-foil structure. Note that such plastic structures can be metallized by sputter deposition of the desired metal. Although here implemented at terahertz frequencies, the techniques of imprinting or hot embossing suggest that the chiral meta-foil concept can be extended to higher infrared and optical frequencies, with cost-effective mass manufacture.

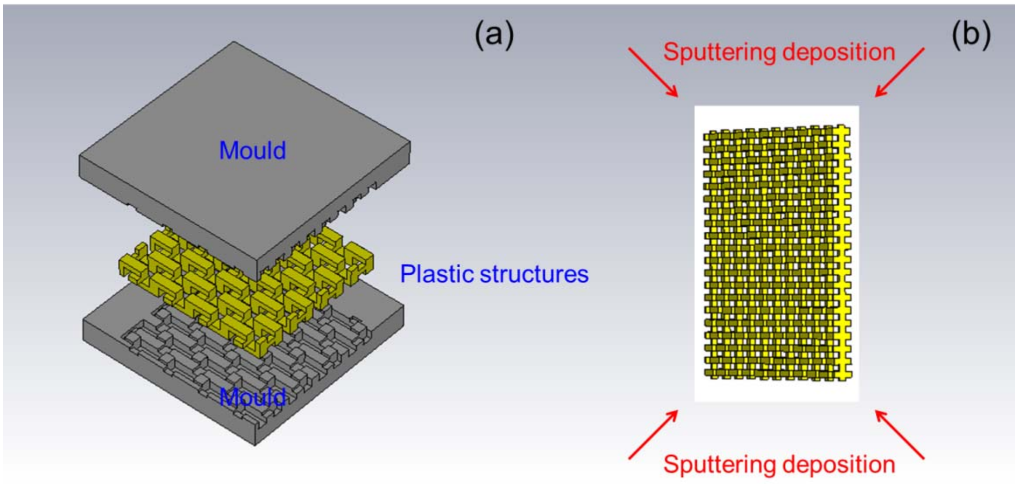

Figure 7.6 *(a) Schematic of meta-foils' manufacture by plastic moulding. (b) Schematic of plastic meta-foils' metallization by sputtering deposition of the desired metal.*

7.4 Conclusion

We have designed, manufactured and demonstrated broad-band chiral meta-foils that exhibit a high-contrast circular polarization selectivity over a bandwidth of about one octave (1.7-3.4 THz). This is achieved by a simple design variation of the well-known meta-foil, namely replacing straight interconnecting lines by alternating ones. In chemical terminology, we may regard the "molecules" in LPC and RCP chiral meta-foils as enantiomers and, consequently, the conventional meta-foil as a corresponding racemic modification. All of meta-foil structures can be fabricated by means of the well-established 3-level photolithography and gold electroplating technique. As the geometric structure of meta-foils is amenable to hot embossing or nanoimprinting, the results achieved hold promise to enable extension of the frequency range up to the visible red with gold by reducing geometric parameters suitably. Owing to the all-metal structure of meta-foils, there are no dielectrics of substrates or embedding matrices that could lead to a red-shift of the frequencies. Hence, full use can be made of the accessible spectral range that extends up to about 450 THz (667 nm) before limiting plasmonic effects are expected to set in [181]. An additional benefit of hot embossing and nanoimprint processes is a ready access to cost-effective mass manufacture. In this way, for the first time, broad-band circular polarization filters may be realized over a spectral range spanning almost three orders of magnitude from THz to the visible red. This covers, in particular, the important infrared "fingerprint" range (12-120 THz) that is routinely used for infrared molecular spectroscopy including related methods like vibrational circular dichroism.

Chapter 8

Conclusions and Future Work

8.1 Conclusions

In this thesis, the design, fabrication and characterization of meta-foils are studied to realize the various interesting functions in the terahertz (THz) region. THz meta-foils, fabricated by UV lithography and gold electroplating, are the all-metal, self-supported, locally stiff, globally flexible meshes. It is a unique approach to create an electromagnetic metamaterial that is free of dielectrics such as embedding matrices or supporting substrates. THz meta-foils' properties are thus solely determined by the geometric structure and the metal properties. At the same time, THz meta-foils are a 3D all-metal left-handed metamaterial, which provides a new structure design to effectively realize negative refractive index in the THz region. By changing the structure geometry that is still based on 'S-string' architecture, we propose the functional multi-band THz meta-foils and polarization-independent crossed THz meta-foils. By combining chirality with meta-foils, we develop the narrowband conjugated rosette chiral meta-foils and broadband chiral meta-foils. These four new meta-foils extend greatly the previous work on conventional 1SE meta-foils at different aspects.

Functional multi-band THz meta-foils are theoretically and experimentally investigated. Multi-band meta-foils are constructed by multi-cell S-string resonators in a single structure, exhibiting simultaneously negative permittivity and negative permeability responses at multiple frequencies. The phenomena are confirmed by numerical simulations and Fourier transform infrared spectroscopy measurements. Equivalent circuit analysis is applied to better understand the physical nature of the coupling between resonators and dip formation in multi-band meta-foils. Applications of spectral calibration and identification of molecules by multi-band filters are discussed. The flexible, freestanding multi-band meta-foils provide a promising candidate for the development of multi-frequency THz materials and devices.

Crossed THz meta-foils are proposed to be polarization-independent left-handed metamaterials. Upon showing that conventional parallel-string meta-foils exhibit a strong polarization dependence, we demonstrate the polarization independency of crossed meta-foils and discuss their differences. By the parameter retrieval calculations, we show the transition from 1SE over 1SP to crossed meta-foils, which gives a clear physical insight of meta-foils based on 'S-string' architecture. Polarization-independent, all-metal, self-supported, free-standing, 3D left-handed metamaterials are achieved that provide a versatile platform for developing practical applications of metamaterials.

Conjugated rosette THz chiral meta-foils, as the first product of meta-foils combined with chirality, consist of a self-supported square array of interconnected conjugated rosettes. They exhibit strong optical activity, large circular dichroism, which are demonstrated by both CST simulation and terahertz time domain spectroscopy. By retrieval calculations, negative refractive index with a figure-of merit as high as 4.2 is achieved, attributed to the free-standing nature. Conjugated rosette THz chiral meta-foils offer a new purely metal chiral design in THz metamaterial world.

Broadband THz chiral meta-foils are proposed to overcome the narrow bandwidth of conjugated rosette THz chiral meta-foils. The design, fabrication and characterization of broadband THz chiral meta-foils are studied. Broadband chiral meta-foils exhibit a strong contrast circular dichroic effect over a bandwidth of about one octave (1.7-3.3 THz), which provides a new promising route to build up the broadband circular polarizer.

Various designs allow THz meta-foils with various functions. All meta-foils proposed above can be tailor-made to virtually any shape, they can be bent, and wrapped around objects to shield them from electromagnetic radiation, thus becoming true metamaterials on curved surfaces. Furthermore, meta-foils can be manufactured by imprinting and hot embossing in any frequency range, enabling cost-effective mass manufacture. Although implemented here at THz frequencies, multiple-cell meta-foils can also be extended to higher frequency infrared and optical frequencies. Overall, all THz meta-foils proposed in this thesis provide a versatile platform for developing THz materials and devices the strong resonance properties and the tunable features, which can be directly and realistically integrated into current devices and systems.

8.2 Future Work

Without any doubt, metamaterials have become an extremely exciting research area. Within only these ten years, we have witnessed many remarkable breakthroughs, such as negative refraction, superlensing and invisibility cloaking. It is important for us to remember that the field of electromagnetic metamaterials is still rather young. Many other fascinating discoveries and applications are still waiting for us to explore. THz meta-foils, as a promising candidate in THz metamaterials, provide a versatile platform for practical applications of metamaterials in the THz region. The multi-band, polarization-independent and chiral properties in different meta-foils have been experimentally demonstrated. Other applications of meta-foils, such as sensors, perfect absorbers, cylindrical lenses and terahertz cloaks, may be realized experimentally in the future.

Any dielectrics can bring metamaterials the insertion losses and resonance shift [102]. A process was demonstrated for tuning the magnetic resonance frequency of a fixed split-ring resonator (SRR) array, by way of adding materials near the split-ring elements [182]. Applying drops of a silicon-nanospheres/ethanol solution to the surface of the sample decreases the magnetic resonance frequency of SRR array. Tao et al. designed, fabricated, and characterized SRR based planar terahertz metamaterials on ultrathin silicon nitride substrates for biosensing applications. SRRs fabricated on thin film substrates show significantly better performance than identical SRRs fabricated on bulk silicon substrates [183]. This trend hints that the meta-foil can be a better sensor. As the meta-foil is an all-metal self-supported structure, it is able to have much higher sensitivity to surrounding dielectrics. At the same time, it can work at elevated temperatures to accommodate environmental conditions. Thus, we can find some bio-particles or any other dielectrics to design experiments investigating meta-foils' biological and chemical sensing applications in the future.

Metamaterial absorbers offer benefits over conventional absorbers such as further miniaturization, wider adaptability and increased effectiveness. Perfect metamaterial absorbers proposed usually consist of metal-insulator-metal structures [99-101]. The top metal layer is structurally designed, mostly by planar metamaterial structures, while the bottom layer is purely metal layer. Here, the meta-foils with three-layer structures can replace the top metal layer to be a new perfect absorber design, which may bring some interesting and exciting results. Hence, the meta-foils-based absorber will be investigated in the coming future.

Gradient index optics has been applied to design lenses by shaping the spatial distribution of the refractive index of a material rather than the interface of lenses [96, 128-132]. The resulting lenses can be flat and avoid the typical aberrations of traditional lenses. Multi-band THz meta-foils discussed in Chapter 4 exhibit simultaneously negative permittivity and negative permeability responses at multiple frequencies, which are actually one case of index-gradient metamaterials. As the meta-foils can be bent and adapted to curved surfaces, it is possible to build a cylindrical hyperlens by a stack of bent meta-foils [64]. The meta-foils can be also wrapped around objects to shield them from electromagnetic radiation, indicating THz clocking applications. Although a lot of theoretical work has been carried out on gradient index optics, the experimental demonstrations of hyperlens and clocks are still very limited, especially at THz and optical frequencies. THz meta-foils can be a promising element in the research of index-gradient metamaterials in the future, which is difficult and challenging but possible.

In Chapter 3.3, synchrotron radiation has been experimentally demonstrated to be a better source for sample characterization in the FIR region, and its high photo flux and brilliance enable high resolution and the characterization on extremely small samples. Based on this excellent spatial resolution, we can investigate the spectroscopic probing of single cells of THz meta-foils and study the transverse propagation of the resonant excitation in the future.

In Chapter 5, S-strings with the same S-length in both y and z directions creates all left-handed resonances at the same frequency, making the meta-foils be polarization-independent left-handed metamaterials. S-strings with different S-lengths in both two perpendicular directions, called asymmetric crossed meta-foils, will lead to two different left-handed resonances. It means that the switch of two negative index bands can be realized by a simple 90° rotation. All these have been demonstrated by simulation and parameter retrieval. Following this idea, we will do more work on asymmetric crossed meta-foils in the future.

In Chapter 4 and Chapter 5, the negative refractive index of meta-foils is mainly demonstrated by the parameter retrieval calculations. Next, we will try to experimentally demonstrate it as described in [20].

Most meta-foils proposed so far are based on 'S-string' architecture, except for the conjugated rosette chiral meta-foils discussed in Chapter 6. Next, we can think out other designs to achieve other interesting results. At present, all meta-foils are investigated in the THz region. In the future, they can also be manufactured by plastic moulding. Two parts of either a mould insert for injection moulding or two parts of a hot embossing die yield the plastic meta-foil structure. Such plastic structures can be metallized by sputtering deposition of the desired metal. The techniques of imprinting or hot embossing support meta-foils being extended to higher infrared and optical frequencies, with cost-effective mass manufacture.

Meta-foils require all structures connected each other. Layer-by-layer structures without connections between adjacent unit cells are also interesting.

The fabrication procedure is similar except the final releasing step, and the whole structures are standing on substrate. Recently, Averitt et al. [60, 61] have fabricated and investigated stand-up magnetic metamaterials at THz frequencies. Thus, we can also find some new designs and new applications to do some work on stand-up metamaterials. Now, we are studying the helix-like structures to obtain the broadband chiral properties. The design of helix-like structures is similar to the twisted metamaterials [57, 175]. The difference is that between the layers are connected each other. Various helix-like structures have been fabricated, next we will characterize them and discuss their properties.

Bibliography

1. S. A. Ramakrishna, “Physics of negative refractive index materials,” *Rep. Prog. Phys.* **68**, 449-521 (2005).
2. C. M. Soukoulis, M. Kafesaki, and E. N. Economou, “Negative-index materials: new frontiers in optics,” *Adv. Mater.* **18**, 1941-1952 (2006).
3. M. Wegener, and S. Linden, “Shaping optical space with metamaterials,” *Phys. Today* **63**, 32-36 (2010).
4. N. I. Zheludev, “The road ahead for metamaterials,” *Science* **328**, 582-583 (2010).
5. Y. Liu, and X. Zhang, “Metamaterials: a new frontier of science and technology,” *Chem. Soc. Rev.* **40**, 2494-2507 (2011).
6. N. I. Zheludev, and Y. S. Kivshar, “From metamaterials to metadevices,” *Nat. Mater.* **11**, 917-924 (2012).
7. V.G. Veselago, “The electrodynamics of substances with simultaneously negative values of ε and μ,” *Sov. Phys. Usp.* **10**, 509-514 (1968).
8. J. B. Pendry, A. J. Holden, W. J. Stewart, and I. Youngs, “Extremely low frequency plasmons in metallic mesostructures,” *Phys. Rev. Lett.* **76**, 4773-4776 (1996).
9. J. B. Pendry, A. J. Holden, D. J. Robbins, and W. J. Stewart, “Magnetism from conductors and enhanced nonlinear phenomena,” *IEEE Trans. Microwave Theory Tech.* **47**, 2075-2084 (1999).
10. D. R. Smith, W. J. Padilla, D. C. Vier, S. C. Nemat-Nasser, and S. Schultz, “Composite medium with simultaneously negative permeability and permittivity,” *Phys. Rev. Lett.* **84**, 4184-4187 (2000).
11. R. A. Shelby, D. R. Smith, and S. Schultz, “Experimental verification of a negative index of refraction.” *Science* **292**, 77-79 (2001).
12. T. J. Yen, W. J. Padilla, N. Fang, D. C. Vier, D. R. Smith, J. B. Pendry, D. N. Basov, and X. Zhang, “Terahertz magnetic response from artificial materials,” *Science* **303**, 1494-1496 (2004).
13. S. Linden, C. Enkrich, M. Wegener, J. Zhou, Th. Koschny, and C. M. Soukoulis, “Magnetic response of metamaterials at 100 terahertz,” *Science* **306**, 1351-1353 (2004).
14. J. Zhou, Th. Koschny, M. Kafesaki, E. N. Economou, J. B. Pendry, and C. M. Soukoulis, “Saturation of the magnetic response of split-ring resonators at optical frequencies,” *Phys. Rev. Lett.* **95**, 224902 (2005).

15. C. M. Soukoulis, S. Linden, and M. Wegener, “Negative refractive index at optical wavelengths,” *Science* **315**, 47-49 (2007).

16. T. Tanaka, “Using metamaterials to defy our common understanding of light,” *RIKEN Research* **4**, 7:13-16 (2009).

17. S. Zhang, W. J. Fan, N. C. Panoiu, K. J. Malloy, R. M. Osgood, and S. R. J. Brueck, “Experimental demonstration of near-infrared negative-index metamaterials,” *Phys. Rev. Lett.* **95**, 137404 (2005).

18. G. Dolling, C. Enkrich, M. Wegener, C. M. Soukoulis, and S. Linden, “Simultaneous negative phase and group velocity of light in a metamaterial,” *Science* **312**, 892-894 (2006).

19. G. Dolling, M. Wegener, C. M. Soukoulis, and S. Linden, “Negative-index metamaterial at 780 nm wavelength,” *Opt. Lett.* **32**, 53-55 (2007).

20. J. Valentine, S. Zhang, T. Zentgraf, E. Ulin-Avila, D. A. Genov, G. Bartal, and X. Zhang, “Three-dimensional optical metamaterial with a negative refractive index,” *Nature* **455**, 376-379 (2008).

21. S. Xiao, U. K. Chettiar, A. V. Kildishev, V. P. Drachev, and V. M. Shalaev, “Yellow-light negative-index metamaterials,” *Opt. Lett.* **34**, 3478-3480 (2009).

22. C. Helgert, C. Menzel, C. Rockstuhl, E. Pshenay-Severin, E.-B. Kley, A. Chipouline, A. Tünnermann, F. Lederer, and T. Pertsch, “Polarization-independent negative-index metamaterial in the near infrared,” *Opt. Lett.* **34**, 704-706 (2009).

23. D. Chanda, K. Shigeta, S. Gupta, T. Cain, A. Carlson, A. Mihi, A. J. Baca, G. R. Bogart, P. Braun, and J. A. Rogers, “Large-area flexible 3D optical negative index metamaterial formed by nanotransfer printing,” *Nat. Nanotechnol.* **6**, 402-407 (2011).

24. N. Liu, H. Guo, L. Fu, S. Kaiser, H. Schweizer, and H. Giessen, “Three-dimensional photonic metamaterials at optical frequencies,” *Nature Mater.* **7**, 31-37 (2008).

25. N. Liu, L. Fu, S. Kaiser, H. Schweizer, and H. Giessen, “Plasmonic building blocks for magnetic molecules in three-dimensional optical metamaterials,” *Adv. Mater.* **20**, 3859-3865 (2008).

26. J. B. Pendry, “Negative refraction makes a perfect lens,” *Phys. Rev. Lett.* **85**, 3966-3969 (2000).

27. A. Grbic, and G. V. Eleftheriades, “Overcoming the diffraction limit with a planar left-handed transmission –line lens,” *Phys. Rev. Lett.* **92**, 117403 (2004).

28. A. N. Lagarkov, and V. N. Kissel, “Near-perfect imaging in a focusing system based on a left-handed-material plate,” *Phys. Rev. Lett.* **92**, 077401 (2004).

29. N. Fang, H. Lee, C. Sun, and X. Zhang, “Sub-diffraction-limited optical imaging with a silver superlens,” *Science* **308**, 534-537 (2005).

30. T. Taubner, D. Korobkin, Y. Urzhumov, G. Shvets, and R. Hillenbrand, “Near-field microscopy through a SiC superlens,” *Science* **313**, 1595 (2006).

31. X. Zhang, and Z. Liu, “Superlenses to overcome the diffraction limit,” *Nat. Mater.* **7**, 435-441 (2008).

32. J. B. Pendry, D. Schurig, and D. R. Smith, “Controlling electromagnetic fields,” *Science* **312**, 1780-1782 (2006).

33. D. Schurig, J. J. Mock, B. J. Justice, S. A. Cummer, J. B. Pendry, A. F. Starr, and D. R. Smith, “Metamaterial electromagnetic cloak at microwave frequencies,” *Science* **314**, 977-980 (2006).

34. U. Leonhardt, “Optical conformal mapping”, *Science* **312**, 1777-1780 (2006).

35. W. Cai, U. K. Chettiar, A. V. Kildishev, and V. M. Shalaev, “Optical cloaking with metamaterials,” *Nat. Photon.* **1**, 224-227 (2007).

36. U. Leonhardt, and T. Tyc, “Broadband invisibility by non-Euclidean cloaking,” *Science* **323**, 110-112 (2008).

37. J. Li, and J. B. Pendry, “Hiding under the Carpet: a new strategy for cloaking,” *Phys. Rev. Lett.* **101**, 203901 (2008).

38. R. Liu, C. Ji, J. J. Mock, J. Y. Chin, T. J. Cui, and D. R. Smith, “Broadband ground-plane cloak,” *Science* **323**, 366-369 (2009).

39. H. F. Ma, and T. J. Cui, “Three-dimensional broadband ground-plane cloak made of metamaterials,” *Nat. Commun.* **1**, 1-6 (2010).

40. J. Valentine, J. Li, T. Zentgraf, G. Bartal, and X. Zhang, “An optical cloak made of dielectrics,” *Nat. Mater.* **8**, 568-571 (2009).

41. L. H. Gabrielli, J. Gardenas, C. B. Poitras, and M. Lipson, “Silicon nanostructure cloak operating at optical frequencies,” *Nat. Photon.* **3**, 461-463 (2009).

42. B. Ferguson and X.-C. Zhang, “Materials for terahertz science and technology,” *Nat. Mater.* **1**, 26-33 (2002).

43. C. A. Schmuttenmaer, “Exploring Dynamics in the far-infrared with terahertz spectroscopy,” *Chem. Rev.* **104**, 1759-1779 (2004).

44. M. Tonouchi, "Cutting-edge terahertz technology," *Nat. Photon.* **1**, 97-105 (2007).

45. P. U. Jepsen, D. G. Cooke, and M. Koch, "Terahertz spectroscopy and image – Modern techniques and applications," *Laser Photon. Rev.* **5**, 124-166 (2011).

46. X. C. Zhang, "Terahertz wave imaging: horizons and hurdles," *Phys. Med. Biol.* **47**, 3667-3677 (2002).

47. J. Faist, F. Capasso, D. L. Sivco, C. Sirtori, A. L. Hutchinson, and A. Y. Cho, "Quantum cascade laser," *Science* **264**, 553-556 (1994).

48. D. H. Auston, and K. P. Cheung, "Coherent time-domain far-infrared spectroscopy," *J. Opt. Soc. Am. B* **2**, 606-612 (1985).

49. R. D. Averitt, and A. J. Taylor, "Ultrafast optical and far-infrared quasiparticle dynamics in correlated electron materials," *J. Phys. Condens. Matter.* **14**, R1357-R1390 (2002).

50. W. Withayachumnankul, and D. Abbott, "Metamaterials in the terahertz regime," *IEEE Photon. J.* **1**, 99-108 (2009).

51. H.-T. Chen, J. F. O'Hara, A. K. Azad, A. J. Taylor, "Manipulation of terahertz radiation using metamaterials," *Laser Photon. Rev.* **5**, 513-533 (2011).

52. H. O. Moser, and C. Rockstuhl, "3D THz metamaterials from micro/nanomanufacturing," *Laser Photon. Rev.* **6**, 219-244 (2012).

53. C. M. Bingham, H. Tao, X. Liu, R. D. Averitt, X. Zhang, and W. J. Padilla, "Planar wallpaper group metamaterials for novel terahertz applications," *Opt. Express* **16**, 18565-18575 (2008).

54. J. D. Baena, L. Jelinek, and R. Marqués, "Towards a systematic design of isotropic bulk magnetic metamaterials using the cubic point groups of symmetry," *Phys. Rev. B* **76**, 245115 (2007).

55. C. Rockstuhl, F. Lederer, C. Etrich, T. Pertsch, and T. Scharf, "Design of an artificial three-dimensional composite metamaterial with magnetic resonances in the visible range of the electromagnetic spectrum," *Phys. Rev. Lett.* **99**, 017401 (2007).

56. N. Liu, H. Liu, S. Zhu, and H. Giessen, "Stereometamaterials," *Nat. Photon.* **3**, 157-162 (2009).

57. J. K. Gansel, M. Thiel, M. S. Rill, M. Decker, K. Bade, V. Saile, G. V. Freymann, S. Linden, and M. Wegener, "Gold helix photonic metamaterial as broadband circular polarizer," *Science* **325**, 1513-1515 (2009).

58. D. B. Burckel, J. R. Wendt, G. A. T. Eyck, J. C. Ginn, A. R. Ellis, I. Brener, and M. B. Sinclair, "Micrometer-scale cubic unit cell 3D metamaterial layers," *Adv. Mater.* **22**, 5053-5057 (2010).

59. D. Ö. Güney, Th. Koschny, and C. M. Soukoulis, "Intra-connected three-dimensionally isotropic bulk negative index photonic metamaterial," *Opt. Express* **18**, 12348-12353 (2010).

60. K. Fan, A. C. Strikwerda, H. Tao, X. Zhang, and R. D. Averitt, "Stand-up magnetic metamaterials at terahertz frequencies," *Opt. Express* **19**, 12619-12627 (2011).

61. K. Fan, A. C. Strikwerda, X. Zhang, and R. D. Averitt, "Three-dimensional broadband tunable terahertz metamaterials," *Phys. Rev. B* **87**, 161104 (2013).

62. H. O. Moser, J. A. Kong, L. K. Jian, H. S. Chen, G. Liu, M. Bahou, S. M. P. Kalaiselvi, S. M. Maniam, X. X. Cheng, B.-I. Wu, P. D. Gu, A. Chen, S. P. Heussler, S. B. Mahmood, and L. Wen, "Free-standing THz electromagnetic metamaterials," *Opt. Express* **16**, 13773-13780 (2008).

63. H. O. Moser, L. K. Jian, H. S. Chen, M. Bahou, S. M. P. Kalaiselvi, S. Virasawmy, S. M. Maniam, X. X. Cheng, S. P. Heussler, S. B. Mahmood, and B.-I. Wu, "All-metal self-supported THz metamaterial – the meta-foil," *Opt. Express* **17**, 23914-23919 (2009).

64. H. O. Moser, L. K. Jian, H. S. Chen, M. Bahou, S. M. P. Kalaiselvi, S. Virasawmy, X. X. Cheng, A. Banas, K. Banas, S. P. Heussler, B.-I. Wu, W. B. Zhang, S. M. Maniam, and W. Hua, "THz meta-foil – a platform for practical applications of metamaterials," *J. Mod. Opt.* **57**, 1936-1943 (2010).

65. H. O. Moser, L. K. Jian, H. S. Chen, M. Bahou, S. M. P. Kalaiselvi, S. Virasawmy, S. M. Maniam, X. X. Cheng, S. P. Heussler, S. B. Mahmood, and B.-I. Wu, "Self-supported all-metal THz metamaterials," *Proc. of SPIE* **7392**, 73920E (2009).

66. H. O. Moser, L. K. Jian, H. S. Chen, S. M. P. Kalaiselvi, S. Virasawmy, S. M. Maniam, X. X. Cheng, A. Banas, K. Banas, S. P. Heussler, M. Bahou, B.-I. Wu, W. Hua, and Z. Yi, "Geometry-functional relationships in meta-foils," *Proc. of SPIE* **7711**, 771119 (2010).

67. R. Alaee, C. Menzel, A. Banas, K. Banas, S. Xu, H. Chen, H. O. Moser, F. Lederer, and C. Rockstuhl, "Propagation of electromagnetic fields in bulk terahertz metamaterials: a combined experimental and theoretical study," *Phys. Rev. B* **87**, 075110 (2013).

68. H. Chen, L. Ran, J. Huangfu, X. Zhang, and K. Chen, “Left-handed materials composed of only S-shaped resonators,” *Phys. Rev. E* **70**, 057605 (2004).

69. J. D. Jackson, “Classical Electromagnetics,” 3rd ed. (John Wiley & Sons, New York, 1999).

70. X. Chen, T. M. Grzegorczyk, B.-I. Wu, J. Pacheco, Jr., and J. A. Kong, “Robust method to retrieve the constitutive effective parameters of metamaterials,” *Phys. Rev. E* **70**, 016608 (2004).

71. J. A. Kong, “Electromagnetic wave theory,” (Cambridge, MA: EMW Publishing, 2008).

72. S. Tretyakov, I. Nefedov, A. Sihvola, S. Maslovski, and C. Simovski, “Waves and energy in chiral nihility,” *J. Electromagn. Waves Appl.* **17**, 695-706 (2003).

73. J. B. Pendry, “A chiral route to negative refraction,” *Science* **306**, 1352-1355 (2004).

74. A. V. Rogacheva, V. A. Fedotov, A. S. Schwanecke, and N. I. Zheludev, “Giant gyrotropy due to electromagnetic-field coupling in a bilayered chiral structure,” *Phys. Rev. Lett.* **97**, 177401 (2006).

75. E. Plum, J. Zhou, J. Dong, V. A. Fedotov, Th. Koschny, C. M. Soukoulis, and N. I. Zheludev, “Metamaterial with negative index due to chirality,” *Phys. Rev. B* **79**, 035407 (2009).

76. S. Zhang, Y.-S. Park, J. Li, X. Lu, W. Zhang, and X. Zhang, “Negative refractive index in chiral metamaterials,” *Phys. Rev. Lett.* **102**, 023901 (2009).

77. M. Decker, R. Ruther, C. E. Kriegler, J. Zhou, C. M. Soukoulis, S. Linden, and M. Wegener, “Strong optical activity from twisted-cross photonic metamaterials,” *Opt. Lett.* **34**, 2501-2503 (2009).

78. M. Decker, R. Zhao, C. M. Soukoulis, S. Linden, and M. Wegener, “Twisted split-ring-resonator photonic metamaterial with huge optical activity,” *Opt. Lett.* **35**, 1593-1595 (2010).

79. A. D. Boardman, V. V. Grimalsky, Y. S. Kivshar, S. V. Koshevaya, M. Lapine, N. M. Litchinitser, V. N. Malnev, M. Noginov, Y. G. Rapoport, and V. M. Shalaev, “Active and tunable metamaterials,” *Laser Photon. Rev.* **5**, 287-307 (2011).

80. A. Q. Liu, W. M. Zhu, D. P. Tsai, and N. I. Zheludev, “Micromachined tunable metamaterials: a review,” *J. Opt.* **14**, 114009 (2012).

81. H.-T. Chen, W. J. Padilla, J. M. O. Zide, A. C. Gossard, A. J. Taylor, and R. D. Averitt, "Active terahertz metamaterial devices," *Nature* **444**, 597-600 (2006).

82. A. Degiron, J. J. Mock, and D. R. Smith, "Modulating and tuning the response of metamaterials at the unit cell level," *Opt. Express* **15**, 1115-1127 (2007).

83. H.-T. Chen, J. F. O'Hara, A. K. Azad, A. J. Taylor, R. D. Averitt, D. B. Shrekenhamer, and W. J. Padilla, "Experimental demonstration of frequency-agile terahertz metamaterials," *Nat. Photon.* **2**, 295-298 (2008).

84. H.-T. Chen, W. J. Padilla, M. J. Cich, A. K. Azad, R. D. Averitt, and A. J. Taylor, "A metamaterial solid-state terahertz phase modulator," *Nat. Photon.* **3**, 148-151 (2009).

85. M. Lapine, D. Powell, M. Gorkunov, I. Shadrivov, R. Marqués, and Y. Kivshar, "Structural tenability in metamaterials," *Appl. Phys. Lett.* **95**, 084105 (2009).

86. S. Aksu, M. Huang, A. Artar, A. A. Yanik, S. Selvarasah, M. R. Dokmeci, and H. Altug, "Flexible plasmonics on unconventional and nonplanar substrates," *Adv. Mater.* **23**, 4422-4430 (2011).

87. Z. C. Chen, R. Mohsen, Y. D. Gong, C. T. Chong, and M. H. Hong, "Realization of variable three-dimensional terahertz metamaterials tubes for passive resonance tenability," *Adv. Mater.* **24**, OP143-OP147 (2012).

88. M. Lapine, I. V. Shadrivov, D. A. Powell, and Y. S. Kivshar, "Magnetoelastic metamaterials," *Nat. Mater.* **11**, 30-33 (2012).

89. J. Y. Ou, E. Plum, L. Jiang, and N. I. Zheludev, "Reconfigurable photonic metamaterials," *Nano Lett.* **11**, 2142-2144 (2011).

90. S. Xiao, V. P. Drachev, A. V. Kildishev, X. Ni, U. K. Chettiar, H.-K. Yuan, and V. M. Shalaev, "Loss-free and active optical negative-index metamaterials," *Nature* **466**, 735-738 (2010).

91. M. A. Noginov, G. Zhu, M. Mayy, B. A. Ritzo, N. Noginova, and V. A. Podolskiy, "Stimulated emission of surface Plasmon polaritons," *Phys. Rev. Lett.* **101**, 226806 (2008).

92. E. Plum, V. A. Fedotov, P. Kuo, D. P. Tsai, and N. I. Zheludev, "Towards the lasing spaser: controlling metamaterial optical response with semiconductor quantum dots," *Opt. Express* **17**, 8548-8551 (2009).

93. N. I. Zheludev, S. L. Prosvirnin, N. Papasimakis, and V. A. Fedotov, "Lasing spaser," *Nat. Photon.* **2**, 351-354 (2008).

94. S. Wuestner, A. Pusch, K. L. Tsakmakidis, J. M. Hamm, and O. Hess, “Overcoming losses with gain in a negative refractive index metamaterial,” *Phys. Rev. Lett.* **105**, 127401 (2010).

95. A. Fang, Th. Koschny, and C. M. Soukoulis, “Self-consistent calculations of loss-compensated fishnet metamaterials,” *Phys. Rev. B* **82**, 121102(R) (2010).

96. Y. Liu, and X. Zhang, “Recent advances in transformation optics,” *Nanoscale* **4**, 5277-5292 (2012).

97. Y. Lai, J. Ng, H. Y. Chen, D. Z. Han, J. J. Xiao, Z.-Q, Zhang, and C. T. Chan, “Illusion optics: the optical transformation of an object into another object,” *Phys. Rev. Lett.* **102**, 253902 (2009).

98. Y. Lai, H. Y. Chen, Z.-Q. Zhang, and C. T. Chan, “Complementary media invisibility cloak that cloaks objects at a distance outside the clocking shell,” *Phys. Rev. Lett.* **102**, 093901 (2009).

99. N. I. Landy, S. Sajuyigbe, J. J. Mock, D. R. Smith, and W. J. Padilla, “Perfect metamaterial absorber,” *Phys. Rev. Lett.* **100**, 207402 (2008).

100. Y. D. Chong, L. Ge, H. Cao, and A. D. Stone, “Coherent perfect absorbers: time-reversed lasers,” *Phys. Rev. Lett.* **105**, 053901 (2010).

101. K. Aydin, V. E. Ferry, R. M. Briggs, and H. A. Atwater, “Broadband polarization-independent resonant light absorption using ultrathin plasmonic super absorbers,” *Nat. Commun.* **2**, 517 (2011).

102. T. Chen, S. Li, and H. Sun, “Metamaterials application in sensing,” *Sensors* **12**, 2742-2765 (2012).

103. N. Papasimakis, V. A. Fedotov, N. I. Zheludev, and S. L. Prosvirnin, “Metamaterial analog of electromagnetically induced transparency,” *Phys. Rev. Lett.* **101**, 253903 (2008).

104. S.-Y. Chiam, R. Singh, C. Rockstuhl, F. Lederer, W. Zhang, and A. A. Bettiol, “Analogue of electromagnetically induced transparency in a terahertz metamaterials,” *Phys. Rev. B* **80**, 153103 (2009).

105. N. Liu, L. Langguth, T. Weiss, J. Kästel, M. Fleischhauer, T. Pfau, and H. Giessen, “Plasmonic analogue of electromagnetically induced transparency at the Drude damping limit,” *Nat. Mater.* **8**, 758-762 (2009).

106. J. Gu, R. Singh, X. Liu, X. Zhang, Y. Ma, S. Zhang, S. A. Maier, Z. Tian, A. K. Azad, H.-T. Chen, A. J. Taylor, J. Han, and W. Zhang, “Active control of electromagnetically induced transparency analogue in terahertz metamaterials,” *Nat. Commun.* **3**, 1151 (2012).

107. M. Bahou, L. Wen, X. Ding, B. D. F. Casse, S. P. Heussler, P. Gu, C. Diao, H. O. Moser, W.-S. Sim, J. Gu, Y.-L. Mathis, "Infrared spectro/microscopy at SSLS – edge effect source in a compact superconducting storage ring," *Am. Inst. Phys. Conf. Proc.* **879**, 603-606 (2007).

108. W. D. Duncan, and G. P. Williams, "Infrared synchrotron radiation from electron storage rings," *Appl. Opt.* **22**, 2914-2923 (1983).

109. M. Abo-Bakr, J. Feikes, K. Holldack, P. Kuske, W. B. Peatman, U. Schade, and G. Wüstefeld, "Brilliant, coherent far-infrared (THz) synchrotron radiation," *Phys. Rev. Lett.* **90**, 094801 (2003).

110. H. O. Moser, B. D. F. Cassse, O. Wilhelmi, and B. T. Saw, "Terahertz response of a microfabricated rod-split-ring-resonator electromagnetic metamaterial," *Phys. Rev. Lett.* **94**, 063901 (2005).

111. W. J. Padilla, M. T. Aronsson, C. Highstrete, M. Lee, A. J. Taylor, and R. D. Averitt, "Electrically resonant terahertz metamaterials: theoretical and experimental investigations," *Phys. Rev. B* **75**, 041102 (2007).

112. H.-T. Chen, J. F. O'Hara, A. J. Taylor, R. D. Averitt, C. Highstrete, M. Lee, and W. J. Padilla, "Complementary planar terahertz metamaterials," *Opt. Express* **15**, 1084-1095 (2007).

113. Z. C. Chen, M. H. Hong, C. S. Lim, N. R. Han, L. P. Shi, and T. C. Chong, "Parallel laser microfabrication of large-area asymmetric split ring resonator metamaterials and its structural tuning for terahertz resonance," *Appl. Phys. Lett.* **96**, 181101 (2010).

114. S.-Y. Chiam, R. Singh, W. Zhang, and A. A. Bettiol, "Controlling metamaterial resonances via dielectric and aspect ratio effects," *Appl. Phys. Lett.* **97**, 191906 (2010).

115. H. Tao, J. J. Amsden, A. C. Strikwerda, K. Fan, D. L. Kaplan, X. Zhang, R. D. Averitt, and F. G. Omenetto, "Metamaterial silk composites at terahertz frequencies," *Adv. Mater.* **22**, 3527-3531 (2010).

116. H. Tao, L. R. Chieffo, M. A. Brenckle, S. M. Siebert, M. Liu, A. C. Strikwerda, K. Fan, D. L. Kaplan, X. Zhang, R. D. Averitt, and F. G. Omenetto, "Metamaterials on paper as a sensing platform," *Adv. Mater.* **23**, 3197-3201 (2011).

117. Y. Yuan, C. Bingham, T. Tyler, S. Palit, T. H. Hand, W. J. Padilla, D. R. Smith, N. M. Jokerst, and S. A. Cummer, "Dual-band planar electric metamaterial in the terahertz regime," *Opt. Express* **16**, 9746-9752 (2008).

118. Y. Yuan, C. Bingham, T. Tyler, S. Palit, T. H. Hand, W. J. Padilla, N. M. Jokerst, and S. A. Cummer, "A dual-resonant terahertz metamaterial

based on single-particle electric-field-coupled resonators," *Appl. Phys. Lett.* **93**, 191110 (2008).

119. S. Hussain, J. M. Woo, and J.-H. Jang, "Dual-band terahertz metamaterials based on nested split ring resonators," *Appl. Phys. Lett.* **101**, 091103 (2012).

120. C. S. Lim, M. H. Hong, Z. C. Chen, N. R. Han, B. Luk'yanchuk, and T. C. Chong, "Hybrid metamaterial design and fabrication for terahertz resonance response enhancement," *Opt. Express* **18**, 12421-12429 (2010).

121. N. R. Han, Z. C. Chen, C. S. Lim, B. Ng, and M. H. Hong, "Broadband multi-layer terahertz metamaterials fabrication and characterization on flexible substrates," *Opt. Express* **19**, 6990-6998 (2011).

122. Q.-J. Du, J.-S. Liu, K.-J. Wang, X.-N. Yi, and H.-W. Yang, "Dual-band terahertz left-handed metamaterial with fishnet structure," *Chin. Phys. Lett.* **28**, 014201 (2011).

123. Y. Zhu, S. Vegesna, Y. Zhao, Y. Kuryatkov, M. Holtz, Z. Fan, M. Saed, and A. A. Bernussi, "Tunable dual-band terahertz metamaterial bandpass filters," *Opt. Lett.* **38**, 2382-2384 (2013).

124. D.-H. Kwon and D. H. Werner, "Near-infrared metamaterials with dual-band negative-index characteristics," *Opt. Express* **15**, 1647-1652 (2007).

125. U. K. Chettiar, A. V. Kildishev, H.-K. Yuan, W. Cai, S. Xiao, V. P. Drachev, and V. M. Shalaev, "Dual-band negative index metamaterial: double negative at 813 nm and single negative at 772 nm," *Opt. Lett.* **32**, 1671-1673 (2007).

126. Q.-Y. Wen, H.-W. Zhang, Y.-S. Xie, Q.-H. Yang, and Y.-L. Liu, "Dual band terahertz metamaterial absorber: design, fabrication, and characterization," *Appl. Phys. Lett.* **95**, 241111 (2009).

127. X. Shen, T. J. Cui, J. Zhao, H. F. Ma, W. X. Jiang, and H. Li, "Polarization-independent wide-angle triple-band metamaterial absorber," *Opt. Express* **19**, 9401-9407 (2011).

128. D. R. Smith, J. J. Mock, A. F. Starr, and D. Schurig, "Gradient index metamaterials," *Phys. Rev. E* **71**, 036609 (2005).

129. R. B. Greegor, C. G. Parazzoli, J. A. Nielsen, M. A. Thompson, M. H. Tanielian, and D. R. Smith, "Simulation and testing of a graded negative index of refractive lens," *Appl. Phys. Lett.* **87**, 091114 (2005).

130. Z. L. Mei, J. Bai, and T. J. Cui, "Gradient index metamaterials realized by drilling hole arrays," *J. Phys. D: Appl. Phys.* **43**, 055404 (2010).

131. Y.-J. Tsai, S. Larouche, T. Tyler, G. Lipworth, N. M. Jokerst, and D. R. Smith, "Design and fabrication of a metamaterial gradient index diffraction grating at infrared wavelengths," *Opt. Express* **19**, 24411-24423 (2011).

132. S. Sun, Q. He, S. Xiao, Q. Xu, X. Li, and L. Zhou, "Gradient-index meta-surfaces as a bridge linking propagating waves and surface waves," *Nat. Mater.* **11**, 426-431 (2012).

133. H. Schweizer, L. Fu, H. Gräbeldinger, H. Guo, N. Liu, S. Kaiser, and H. Giessen, "Negative permeability around 630 nm in nanofabricated vertical meander metamaterials," *Phys. Status Solidi A* **204**, 3886-3900 (2007).

134. H. Chen, L. Ran, J. Huangfu, X. Zhang, K. Chen, T. M. Grzegorczyk, and J. A. Kong, "Metamaterial exhibiting left-handed properties over multiple frequency bands," *J. Appl. Phys.* **96**, 5338 (2004).

135. A. J. Gatesman, R. H. Giles, and J. Waldman, "High-precision reflectometer for submillimeter wavelengths," *J. Opt. Soc. Am. B* **12**, 212-219 (1995).

136. C. R. Simovski, "Material parameters of metamaterials (a review)," *Opt. Spectrosc.* **107**, 726-753 (2009).

137. O. Luukkonen, S. I. Maslovski, and S. A. Tretyakov, "A stepwise Nicolson-Ross-Weir-Based material parameter extraction method," *IEEE Antennas Wireless Propag. Lett.* **10**, 1295-1298 (2011).

138. X. X. Liu, D. A. Powell, and A. Alù, "Correcting the Fabry-Perot artifacts in metamaterial retrieval procedures," *Phys. Rev. B* **84**, 235106 (2011).

139. J. Huangfu, L. Ran, H. Chen, X.-M. Zhang, and K. Chen, T. M. Grzegorczyk, and J. A. Kong, "Experimental confirmation of negative refractive index of a metamaterial composed of **Ω**-like metallic patterns," *Appl. Phys. Lett.* **84**, 1537 (2004).

140. L. Peng, L. Ran, H. Chen, H. Zhang, J. A. Kong, and T. M. Grzegorczyk, "Experimental observation of left-handed behavior in an array of standard dielectric resonators," *Phys. Rev. Lett.* **98**, 157403 (2007).

141. M. R. Leahy-Hoppa, M. J. Fitch, X. Zheng, L. M. Hayden, and R. Osiander, "Wideband terahertz spectroscopy of explosives," *Chem. Phys. Lett.* **434**, 227-230 (2007).

142. I. A. I. Al-Naib, C. Jansen, N. Born, and M. Koch, "Polarization and angle independent terahertz metamaterials with high Q-factors," *Appl. Phys. Lett.* **98**, 091107 (2011).

143. W. M. Zhu, A. Q. Liu, W. Zhang, J. F. Tao, T. Bourouina, J. H. Teng, X. H. Zhang, Q. Y. Wu, H. Tanoto, H. C. Guo, G. Q. Lo, and D. L. Kwong, “Polarization dependent state to polarization-independent state change in THz metamaterials,” *Appl. Phys. Lett.* **99**, 221102 (2011).

144. L. Kelvi, “Baltimore lectures on Molecular Dynamic and the Wave Theory of Light,” page 619 (London, Cambridge University Press Warehouse, 1994).

145. I. V. Lindell, A. H. Sihvola, S. Tretyakov, and A. J. Viitanen, “Electromagnetic waves in chiral and bi-isotropic media,” (Boston, MA: Artech House Publishers, 1994).

146. S. Tretyakov, A. Serdyukov, I. Semchenko, and A. Sihvola, “Electromagnetics of bi-anisotropic materials: theory and applications,” (London: Gordon and Breach Science, 2001).

147. B. Wang, J. Zhou, Th. Koschny, M. Kafesaki, and C. M. Soukoulis, “Chiral metamaterials: simulations and experiments,” *J. Opt. A: Pure Appl. Opt.* **11**, 114003 (2009).

148. Z. Li, M. Mutlu, E. Ozbay, “Chiral metamaterials: from optical activity and negative refractive index to asymmetric transmission,” *J. Opt.* **15**, 023001 (2013).

149. R. Zhao, Th. Koschny, and C. M. Soukoulis, “Chiral metamaterials: retrieval of the effective parameters with and without substrate,” *Opt. Express* **18**, 14553-14567 (2010).

150. E. Plum, V. A. Fedotov, A. S. Schwanecke, N. I. Zheludev, and Y. Chen, “Giant optical gyrotropy due to electromagnetic coupling,” *Appl. Phys. Lett.* **90**, 223113 (2007).

151. Z. Li, R. Zhao, Th. Koschny, M. Kafesaki, K. B. Alici, E. Colak, H. Caglayan, E. Ozbay, and C. M. Soukoulis, “Chiral metamaterials with negative refractive index based on four “U” split ring resonators,” *Appl. Phys. Lett.* **97**, 081901 (2010).

152. X. Xiong, W.-H. Sun, Y.-J. Bao, M. Wang, R.-W. Peng, C. Sun, X. Lu, J. Shao, Z.-F. Li, and N.-B. Ming, “Construction of a chiral metamaterial with a U-shaped resonator assembly,” *Phys. Rev. B* **81**, 075119 (2010).

153. J. Zhou, J. Dong, B. Wang, Th. Koschny, M. Kafesaki, and C. M. Soukoulis, “Negative refractive index due to chirality,” *Phys. Rev. B* **79**, 121104 (2009).

154. Z. Li, H. Caglayan, E. Colak, J. Zhou, C. M. Soukoulis, and E. Ozbay, “Coupling effect between two adjacent chiral structure layers,” *Opt. Express* **18**, 5375-5383 (2010).

155. R. Zhao, L. Zhang, J. Zhou, Th. Koschny, and C. M. Soukoulis, "Conjugated gammadion chiral metamaterial with uniaxial optical activity and negative refractive index," *Phys. Rev. B* **83**, 035105 (2011).

156. J. Zhou, D. R. Chowdhury, R. Zhao, A. K. Azad, H.-T. Chen, C. M. Soukoulis, A. J. Taylor, and J. F. O'Hara, "Terahertz chiral metamaterials with giant and dynamically tunable optical activity," *Phys. Rev. B* **86**, 035448 (2012).

157. Z. Li, K. B. Alici, H. Caglayan, M. Kafesaki, C. M. Soukoulis, and E. Ozbay, "Composite chiral metamaterials with negative refractive index and high values of the figure of merit," *Opt. Express* **20**, 6146-6156 (2012).

158. Z. Li, K. B. Alici, E. Colak, and E. Ozbay, "Complementary chiral metamaterials with giant optical activity and negative refractive index," *Appl. Phys. Lett.* **98**, 161907 (2011).

159. K. Hannam, D. A. Powell, I. V. Shadrivov, and Y. S. Kivshar, "Dispersionless optical activity in metamaterials," *Appl. Phys. Lett.* **102**, 201121 (2013).

160. R. Singh, E. Plum, C. Menzel, C. Rockstuhl, A. K. Azad, R. A. Cheville, F. Lederer, W. Zhang, and N. I. Zheludev, "Terahertz metamaterial with asymmetric transmission," *Phys. Rev. B* **80**, 153104 (2009).

161. S. Zhang, J. Zhou, Y.-S. Park, J. Rho, R. Singh, S. Nam, A. K. Azad, H.-T. Chen, X. Yin, A. J. Taylor, and X. Zhang, "Photoinduced handedness switching in terahertz chiral metamolecules," *Nat. Commun.* **3**, 942 (2012).

162. G. Kenanakis, R. Zhao, A. Stavrinidis, G. Konstantinidis, N. Katsarakis, M. Kafesaki, C. M. Soukoulis, and E. N. Economou, "Flexible chiral metamaterials in the terahertz regime: a comparative study of various designs," *Opt. Mater. Express* **2**, 1702-1712 (2012).

163. R. Zhao, Th. Koschny, E. N. Economou, and C. M. Soukoulis, "Comparison of chiral metamaterial designs for repulsive Casimir force," *Phys. Rev. B* **81**, 235126 (2010).

164. K. Nakanishi, N. Berova, and R. W. Woody, "Circular dichroism: principles and applications," (Weinheim, Germany:VCH, 1994).

165. S. T. Wu, and D. K. Yang, "Reflective liquid crystal displays," (Wiley, New York, 2001).

166. Q. Hong, T. X. Wu, and S. T. Wu, "Optical wave propagation in a cholesteric liquid crystal using the finite element method," *Liq. Cryst.* **30**, 367-375 (2003).

167. S. Huard, “Polarization of light,” (Wiley, New York, 1997).

168. J. K. Gansel, M. Wegener, S. Burger, and S. Linden, “Gold helix photonic metamaterials: a numerical parameter study,” *Opt. Express* **18**, 1059-1069 (2010).

169. M. Thiel. M. S. Rill, G. V. Freymann, and M. Wegener, “Three-dimensional bi-chiral photonic crystals,” *Adv. Mater.* **21**, 4680-4682 (2009).

170. A. Radke, T. Gissibl, T. Klotzbücher, P. V. Braun, H. Giessen, “Three-dimensional bichiral plasmonic crystals fabricated by direct laser writing and electroless silver plating,” *Adv. Mater.* **23**, 3018-3021 (2011).

171. J. K. Gansel, M. Latzel, A. Frölich, J. Kaschke, M. Thiel, and M. Wegener, “Tapered gold-helix metamaterials as improved circular polarizers,” *Appl. Phys. Lett.* **100**, 101109 (2012).

172. Z. Yang, M. Zhao, and P. Lu, “How to improve the signal-to-noise ratio for circular polarizers consisting of helical metamaterials?” *Opt. Express* **19**, 4255-4260 (2011).

173. J. Kaschke, J. K. Gansel, and M. Wegener, “On metamaterial circular polarizers based on metal N-helices,” *Opt. Express* **20**, 26012-26020 (2012).

174. Y. Yan, M. L. Rashad, E. J. Teo, H. Tanoto, J. H. Teng, and A. A. Bettiol, “Selective electroless silver plating of three dimensional SU-8 microstructures on silicon for metamaterials applications,” *Opt. Mater. Express* **1**, 1548-1554 (2011).

175. Y. Zhao, M. A. Belkin, and A. Alù, “Twisted optical metamaterials for planarized ultrathin broadband circular polarizers,” *Nat. Commun.* **3**, 870 (2012).

176. Y. Zhao, J. Shi, L. Sun, X. Li, and A. Alù, “Alignment-free three-dimensional optical metamaterials,” *Adv. Mater.* **26**, 1439 (2014).

177. M. D. Turner, M. Saba, Q. Zhang, B. P. Cumming, G. E. Schröder-Turk, and M. Gu, “Miniature chiral beamsplitter based on gyroid photonic crystals,” *Nat. Photon.* **7**, 801 (2013).

178. H. Beyer and W. Walter, “Lehrhuch der organischen Chemie,” (S. Hirzel Verlag, Stuttgart, 1991).

179. M. Born and E. Wolf, “Principle of optics,” 7th ed., (Cambridge University Press, 2005).

180. P. W. Pohl, “Optik und Atomphysik,” (Springer, 1963).

181. S. Tretyakov, “On geometrical scaling of split-ring and double-bar resonators at optical frequencies,” Metamaterials **1**, 40 (2007).

182. T. Driscoll, G. O. Andreev, D. N. Basov, S. Palit, S. Y. Cho, N. M. Jokerst, and D. R. Smith, “Tuned permeability in terahertz split-ring resonators for devices and sensors,” *Appl. Phys. Lett.* **91**, 062511 (2007).

183. H. Tao, A. C. Strikwerda, M. Liu, J. P. Mondia, E. Ekmekci, K. Fan, D. L. Kaplan, W. J. Padilla, X. Zhang, R. D. Averitt, and F. G. Omenetto, “Performance enhancement of terahertz metamaterials on ultrathin substrate for sensing applications,” *Appl. Phys. Lett.* **97**, 261909 (2010).